



POLITECNICO
MILANO 1863

SCUOLA DI INGEGNERIA INDUSTRIALE
E DELL'INFORMAZIONE

Divertor heat flux and scrape-off layer turbulence studies in negative and positive triangularity plasmas in the TCV tokamak

TESI DI LAUREA MAGISTRALE IN
NUCLEAR ENGINEERING - INGEGNERIA NUCLEARE

Author: **Riccardo Ian Morgan**

Student ID: 992519

Advisor: Prof. Matteo Passoni

Co-advisors: Prof. Christian G. Theiler, Dr. Theodore Golfopoulos

Academic Year: 2023-24

Abstract

Nuclear fusion is the energy source of all active stars in the universe: when two hydrogen nuclei get close enough, they can fuse together into helium, liberating a vast amount of energy in the process. Being able to harness this power would provide a clean, safe and potentially unlimited source of energy. To date, the best candidate to achieve this goal is a machine called Tokamak: a toroidal chamber in which an extremely hot plasma is kept confined by strong magnetic fields. Among the various challenges that are yet to be solved, one that poses particular concern is the intense plasma heat flux expected on a region of the first wall called *divertor*.

The outer part of the plasma, a region known as *Scrape-Off Layer* (SOL), is characterized by high-amplitude turbulent phenomena, during which very elongated filaments of hot and dense plasma (known as *blobs*) are expelled outwards with velocities of the order of 1km/s, thus influencing the level of plasma-wall interaction.

Over the past 30 years, in the Tokamak à Configuration Variable (TCV, located in the EPFL university in Lausanne, Switzerland), there has been intense research on the optimization of the plasma shape. One particular shaping parameter, known as *triangularity*, was observed to deeply affect the plasma behaviour. In particular, as triangularity is reduced from positive to negative values, the plasma confinement level was seen to increase, while turbulence levels and the divertor's heat flux fall-off length λ_q got lower.

This thesis carries out an analysis of data obtained from TCV L-mode plasmas to further investigate the role of triangularity on the divertor heat flux profile and on the SOL turbulence, and to possibly find connections between these two phenomena.

The divertor heat flux profile is determined by Langmuir Probe measurements and is analyzed across a large data-set using the so-called Eich-fitting, revealing a clear negative correlation of the profile fall-off length λ_q with the upper triangularity δ_u . A variety of published scaling laws, compared to experimental results, show how triangularity plays an important role as a regression parameter. Some trends in the q_0 Eich parameter (which contributes to quantify the total power reaching the divertor) are found to be consistent with the acknowledged triangularity dependence and with an unexplained difference in radiated power occurring when the direction of the tokamak magnetic field is inverted.

A second peak sometimes visible in the heat flux profile is also studied, finding a dependence of its position on the outer gap (the distance between the plasma and the outer wall), which is hypothesised to be connected to the deceleration of blobs in the SOL, as some experimental data suggests.

The SOL turbulence, in the form of elongated blobs, is studied with two Gas Puff Imaging (GPI) systems located in different regions of the plasma. Results found significant differences in blob phenomenology with changing triangularity, especially in terms of radial velocity. A mechanism by which this difference could explain the reported λ_q variations is proposed. To investigate this idea and to connect the heat flux profile with the blob features, a heuristic blob model is developed and its predictions were found to be consistent with experimental observations.

Keywords: Plasma physics, triangularity, divertor, heat flux, Eich-fitting, turbulence, blobs, gas-puff imaging

Abstract in lingua italiana

La fusione nucleare è la fonte di energia di tutte le stelle attive nell'universo: quando due nuclei di idrogeno si fanno abbastanza vicini, possono fondersi insieme in elio, liberando una grande quantità di energia nel processo. Riuscire a sfruttare questa reazione fornirebbe una fonte di energia pulita, sicura e potenzialmente illimitata. Ad oggi, il miglior candidato per raggiungere questo obiettivo è una macchina chiamata Tokamak: una camera toroidale in cui un plasma estremamente caldo viene confinato da forti campi magnetici. Tra le varie sfide che devono ancora essere risolte, una che desta particolare preoccupazione è l'intenso flusso di calore previsto dal plasma su una regione della prima parete chiamata *divertore*.

La parte esterna del plasma, una regione nota come *Scrape-Off Layer* (SOL), è caratterizzata da ampie turbolenze, in cui filamenti molto allungati di plasma caldo e denso (noti come *blob*) vengono espulsi verso l'esterno con velocità dell'ordine di 1km/s, influenzando così il livello di interazione plasma-parete.

Negli ultimi 30 anni, nel Tokamak a Configuration Variable (TCV, situato all'università EPFL di Losanna, Svizzera), si è svolta un'intensa ricerca sull'ottimizzazione della forma del plasma. Si è osservato che un particolare parametro geometrico, noto come *triangolarità*, può influenzare profondamente il comportamento del plasma. In particolare, riducendo la triangolarità da valori positivi a negativi, si è visto aumentare il livello di confinamento del plasma e al tempo stesso diminuire i livelli di turbolenza e la lunghezza di decadimento λ_q del flusso di calore sul divertore.

Questa tesi si concentra sull'analisi di dati ottenuti in TCV su plasmi in modo-L per approfondire il ruolo della triangolarità sul profilo del flusso di calore sul divertore e sulla turbolenza nel SOL, e per trovare possibili collegamenti tra questi due fenomeni.

Il profilo del flusso di calore sul divertore è stato determinato tramite misure con sonde di Langmuir ed è stato analizzato su un ampio set di parametri utilizzando il cosiddetto Eich-fitting, rivelando una chiara correlazione negativa tra la lunghezza di decadimento del profilo λ_q e la triangolarità superiore δ_u . Una serie di correlazioni pubblicate in letteratura, confrontate con i risultati sperimentali qui ottenuti, mostrano come la triangolarità giochi un ruolo importante come parametro di regressione. Alcune tendenze del parametro

di Eich q_0 (che contribuisce a quantificare il calore totale che raggiunge il divertore) si dimostrano coerenti con il già citato ruolo della triangolarità e con una differenza non chiarita nella potenza irradiata dal plasma che si verifica quando la direzione del campo magnetico del tokamak viene invertita.

Un secondo picco talvolta visibile nel profilo del flusso di calore è a sua volta oggetto di studio: si osserva una dipendenza della sua posizione dal gap esterno (la distanza tra il plasma e la parete esterna), che si ipotizza collegato alla decelerazione dei blob nel SOL, come suggeriscono alcuni dati sperimentali.

La turbolenza del SOL, sotto forma di blob allungati, viene studiata con due sistemi di GPI (Gas Puff Imaging) situati in regioni diverse del plasma. I risultati rilevano differenze significative nella fenomenologia dei blob al variare della triangolarità, soprattutto per quanto riguarda la loro velocità radiale. Viene proposto un meccanismo in base al quale questa differenza potrebbe spiegare le variazioni di λ_q riportate. Per indagare questa idea e collegare il profilo del flusso di calore con le caratteristiche dei blob, viene sviluppato un modello euristico per i blob, le cui previsioni risultano coerenti con le osservazioni sperimentali.

Parole chiave: Fisica dei plasmi, triangolarità, divertore, flusso di calore, Eich-fitting, turbolenza, blob, gas-puff imaging

Contents

Abstract	i
Abstract in lingua italiana	iii
Contents	v
1 Introduction to nuclear fusion	1
1.1 Thermonuclear fusion reaction	1
1.2 Magnetically confined fusion	5
1.2.1 Physical principles	6
1.2.2 Open questions	8
1.2.3 Near and far future	9
1.3 Thesis outline	11
2 Overview of the plasma edge	13
2.1 Plasma geometry	13
2.1.1 Limited and diverted geometry	14
2.1.2 Coordinate system	15
2.1.3 Plasma shaping and triangularity	18
2.1.4 Scrape-Off Layer geometry	19
2.2 Plasma confinement modes	21
2.3 Divertor heat exhaust	22
2.4 Scrape-Off Layer turbulence	27
2.5 Divertor detachment	30
2.6 Thesis motivation, objectives and methods	33
3 The Tokamak à Configuration Variable	35
3.1 TCV and its role in this thesis	35
3.2 Gas Puff Imaging	36

3.3	Langmuir Probes	40
3.4	Far-InfraRed Interferometer: FIR	42
3.5	Baratron pressure gauges	42
3.6	Multi-spectral imaging: MANTIS	43
4	Data analysis and results	45
4.1	Shots database and preliminary analysis	45
4.2	Heat exhaust on divertor target	48
4.2.1	Eich fitting: fall-off length and spreading factor	51
4.2.2	Eich fitting: main peak and total heat flux	54
4.2.3	Tail and second peak	57
4.3	Filamentary turbulence in the SOL	60
4.3.1	Outer Midplane GPI	60
4.3.2	X-point GPI	63
4.3.3	Blobs evolution from midplane to X-point	65
4.4	Summary and discussion	67
5	Heuristic Blob Model	71
5.1	Model hypotheses and derivation	71
5.2	Predictions and discussion	76
5.3	Limitations and possible improvements	81
6	Conclusions	83
	Bibliography	87
A	Appendix A	95
A.1	List of exploited TCV shots	95
	List of Figures	97
	List of Tables	99
	List of Symbols	101
	Acknowledgements	105

1 | Introduction to nuclear fusion

1.1. Thermonuclear fusion reaction

Over millennia, since the discovery of fire, mankind has gained control over an increasing number of energy sources, exploiting them to heat up homes, to build cities, to understand the world around us and, ultimately, to evolve civilization.

In this regard, it is quite amusing to notice that thermonuclear fusion - a virtually unlimited, cleaner and safer energy source - has always been hiding in plain sight. To see it at work, one just needs to look up towards the Sun.

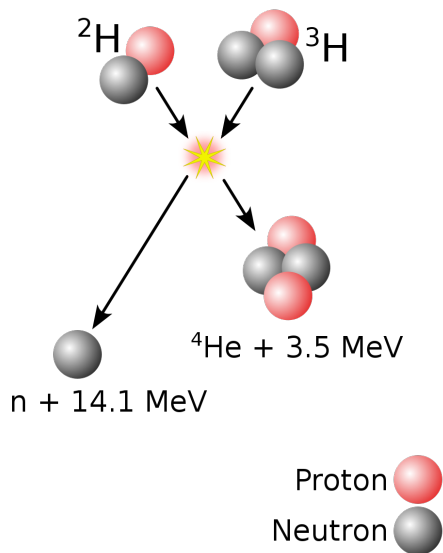


Figure 1.1: Deuterium-tritium fusion scheme.

Only a hundred years ago we understood that nuclear fusion is the reason behind the incredible amount of energy production happening in the stars. Shortly after, physicists and engineers started to investigate viable ways to harvest this energy.

Today we are still struggling in the unprecedented effort of building our own artificial star on earth; and while a lot of research is still needed, incredible milestones have been achieved so far (including a net production of energy in 2022) and much more are expected in the years to come.

But what exactly is nuclear fusion? As the name suggests, it is a process in which the nuclei of 2 light elements merge together, producing one (or more) heavier elements while releasing a vast amount of energy and possibly neutrons.

In Fig.1.1 is depicted the mechanism of deuterium-tritium fusion: two isotopes of hydrogen (Deuterium, having 1 proton and 1 neutron; Tritium, having 1 proton and 2 neutrons) merge together creating a helium-4 nucleus (having 2 protons and 2 neutrons), a free neutron and 17.6 MeV in the form of products' kinetic energy [1].

The great outburst of energy is a consequence of the fact that the fusion of light elements creates products having total rest mass lower than the one of the original nuclei. This mass defect is turned into energy according to the famous equation $E = mc^2$.

From an energy point of view, the products of the fusion reaction have higher binding energy with respect to the starting nuclei. As long as this is true, the fusion reaction remains exothermic. As shown in Fig. 1.2, this happens for elements lighter than Fe-56. For heavier nuclei, fusion becomes an endothermic reaction. On the contrary, splitting the nucleus (a process known as nuclear fission) would now release energy, which explains why fission power plants make use of very heavy elements, such as Uranium [1].

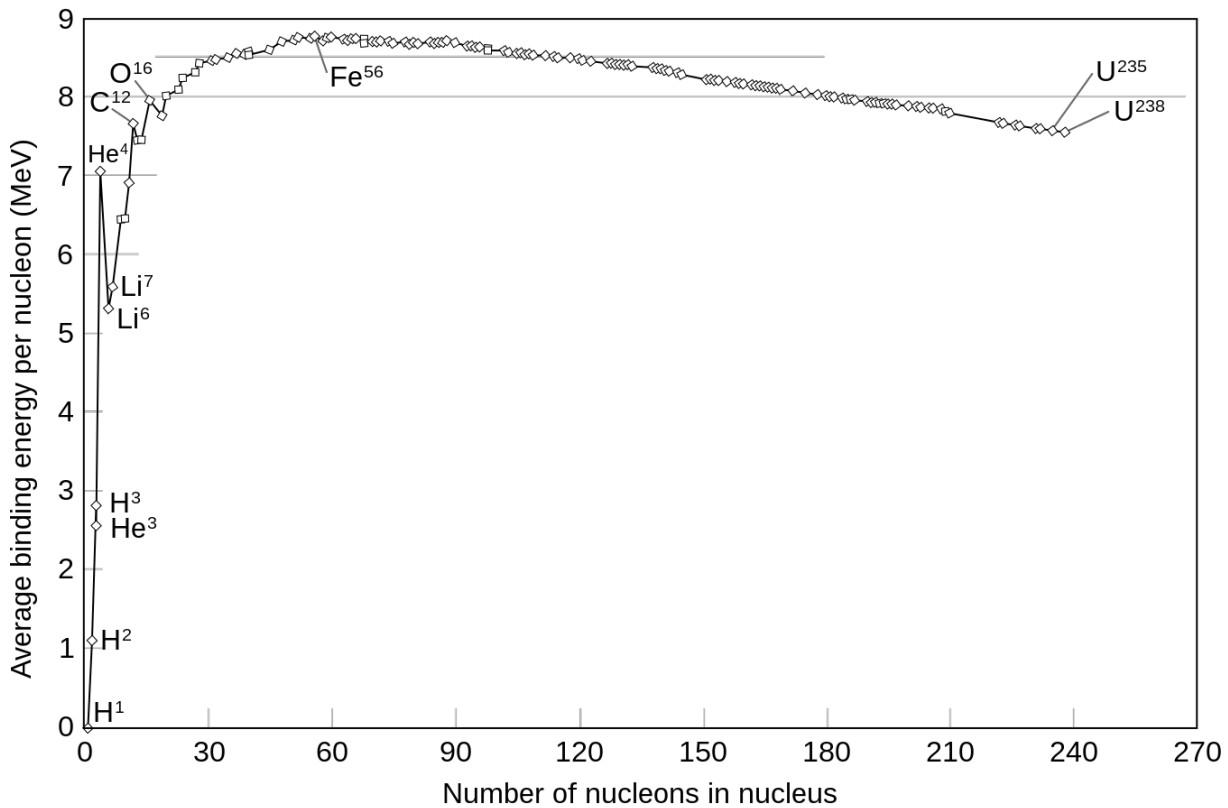


Figure 1.2: Nuclei binding energy per nucleon

The fact that fusion reactions release so much energy does not mean they are easy to obtain. On the contrary, fusion is actually a very difficult reaction to induce. To achieve it, we need to push two positively charged nuclei to subatomic distance, until they are so close that the strong nuclear force ties them together. Before this happens though, we have to overcome Coulomb's electrostatic repulsion, that tries to push the nuclei away from each other. The interplay of the long range Coulomb's repulsion and the nuclear strong force creates a potential barrier that the nuclei must overcome in order to fuse. Luckily, quantum mechanics comes to help [2]: thanks to quantum tunneling, nuclei have a certain probability of "passing through" the potential barrier, so that fusion can also

happen at lower energies.

Regardless, the probability of two nuclei fusing together remains low. To exactly measure how small it is, we can exploit the concept of cross section, defined as follows.

Taken any reaction between particles of types a and b , we can imagine a beam of particles a , with density n_a impinging on a target of particles b with density n_b . If the relative velocity between beam and target is v , we can express the rate of reactions, R , as:

$$R = n_a v \sigma_{a,b} n_b \quad (1.1)$$

Here, σ is the *microscopic cross section*: it is a measure of how likely the reaction is to happen. It is measured in cm^2 , so we could say it measures the "geometric extension" of the particles. In simple terms this would mean: particles with high σ are bigger, so they are more likely to collide and the reaction rate will be higher.

While this interpretation works fine on classical macroscopic systems (e.g. collisions between billiard balls), it must be rejected when describing interaction among nuclei. In fact these are intrinsically quantum objects and not only it is impossible to assign them a specific geometric extension (due to Heisenberg's *indeterminacy principle*), but we also find that any reaction cross section greatly changes with the particle's energy. Despite its strange nature, once the quantum cross section has been properly measured, it is a very reliable tool to compute reaction rates.

Achieving a macroscopic production of energy through fusion is not a simple task. While accelerating a beam of ions on an appropriate target would produce some fusion reactions, since the fusion cross section is so small, the vast majority of the beam's energy would be lost through other effects (such as bremsstrahlung emission, sputtering, excitation of atoms,...) that are much more likely to happen.

The idea is then to create a physical system in which the fusion's fuel is confined in a limited volume and kept under those conditions that make fusion possible [2]. Such conditions will be explained in the following, but intuitively, the most important one is that the temperature of this system must be very high. So high, in fact, that the bonds keeping nuclei and electrons tied together as in ordinary matter will break, and the system will turn into a complex sea of charged particles moving in all directions, in which every particle affects all the others via long range electromagnetic interactions.

This kind of system shows such a different behaviour with respect to solids, liquids and gases that it is identified as the fourth state of matter, and it is called a *plasma*: namely, *any state of matter that contains enough free charged particles for its dynamics to be dominated by electromagnetic forces* [3].

Looking at Eq.1.1, both v and σ depend on energy and since the energy stored in the plasma is directly related with the temperature, the average product $\langle\sigma v\rangle$, called *reaction rate*, will also depend on T [1, 2]. The angular brackets represent an average over all the particles and is needed since they do not travel with the same velocities, but with a velocity distribution that is usually well described by a Maxwellian function.

To understand which reactions are most interesting from the engineering point of view, Fig.1.3 shows the reaction rate as a function of temperature.

It is clear that the Deuterium-Tritium (D-T) reaction offers the highest rate at the lowest temperature, thus becoming the ideal candidate for artificial fusion reactors.

If we want to build a functioning power plant, we must make sure to satisfy a basic *power balance* requirement [1–3]: the plasma must be capable of self-sustaining, that is a condition in which, as long as we inject fuel, it will produce enough energy through fusion to replace the energy losses (with the word *losses* we mean any kind of energy form leaving the plasma, regardless of whether it is turned into electric power, or it is eventually lost as heat). When this happens, the plasma has reached *ignition* and will continue to exist without an external source of energy, otherwise it will quickly cool down and the fusion reaction will stop. We should note that in this simple discussion we are neglecting any injection of external power (that can still be in place during and after ignition) and the power that the plasma loses to heat up the constantly injected fresh fuel.

A plasma reaches ignition condition (and is known as *burning plasma*) if:

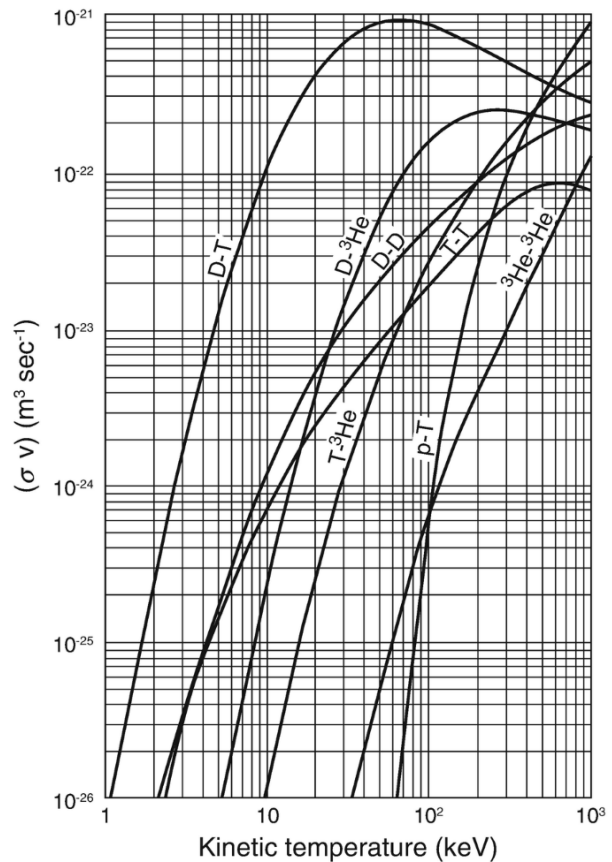


Figure 1.3: Reaction rates for various fusion reactions.

$$P_f > P_b + P_q \quad (1.2)$$

Where P_f is the fusion power, P_b the bremsstrahlung (radiative) losses and P_q the power lost by the plasma due to non-perfect confinement.

In an ideal plasma, where ions and electrons have the same, uniform temperature and density T and $n/2$, we can write:

$$P_f = k_f n^2 \langle \sigma v \rangle \quad (1.3)$$

$$P_b = k_b n^2 T^{1/2} \quad (1.4)$$

$$P_q = \frac{3/2nT}{\tau_e} \quad (1.5)$$

Where k_f and k_b are constants and τ_e is the *energy confinement time*.

In Eq.1.5 the Boltzmann constant is already considered in the temperature T , that must be expressed in eV. Substituting and rearranging, we obtain:

$$nT\tau_e > \frac{3/2T^2}{k_f \langle \sigma v \rangle - k_b T^{1/2}} \quad (1.6)$$

Eq.1.6 is a very important result, known as *Lawson criterion* [4]. It states that, in order to achieve ignition, the *triple product* $nT\tau_e$ must be higher than a minimum value. This minimum value is still dependent on temperature and, for the DT reaction, it has a minimum around 15 keV, that is 150 million °C, 10 times hotter than the Sun's core!

If we consider that the superconducting coils needed to create the magnetic field (and positioned at a distance of about 1m from the plasma core) have to be cooled down to almost 0K, we can start to understand why building a fusion reactor is probably the most challenging engineering effort mankind has ever attempted.

1.2. Magnetically confined fusion

There are two different strategies when it comes to satisfy Lawson's criterion. As we saw in the previous section, the temperature is quite fixed at ≈ 10 keV. The other parameters are more flexible and we can both have a plasma with very high density and very low confinement time, as well as the opposite.

The first approach is exploited by the *inertial confinement* (ICF) schemes: a small pellet of fuel is compressed under the force of very powerful lasers. These beams can ablate the surface of the pellet, which expands outwards very fast. As a reaction, the inner part of the pellet will be compressed inwards, reaching an incredibly high density ($\approx 10^{25}$ cm⁻³) for a very short amount of time ($\tau_e \approx 10^{-9}$ s).

On the contrary, the *magnetic confinement* (MCF) schemes exploit very powerful magnetic fields to keep much bigger, less dense ($\approx 10^{19} \text{ cm}^{-3}$) plasmas confined for much longer times ($\tau_e \approx 1 \text{ s}$ and more).

This thesis will focus on the magnetic confinement approach, that is explained to some extent in the following.

1.2.1. Physical principles

The idea to magnetically confine a plasma arises when noticing that in a very simple linear and uniform magnetic field, such as the one produced by a solenoid, every charged particle is free to move in the direction parallel to the field lines, but is forced to follow a circular motion in the plane perpendicular to the field. If now we close the solenoid on itself, forming a torus with closed magnetic lines, the particles would be trapped inside the torus, at least as a first approximation.

The curvature and non-homogeneity of the magnetic field, in fact, would then introduce charge-dependent drifts in the particle trajectories. The resulting charge separation creates a strong electric field in the plasma, that, coupling with the magnetic field, introduces the $\mathbf{E} \times \mathbf{B}$ drift. This powerful drift would force the entire plasma to expand radially outwards, until it would crash into the chamber walls.

This scenario can be prevented by adding a new component to the magnetic field. Up to now we considered a purely *toroidal* magnetic field, that is the \mathbf{B} field lies in the direction along the torus. To prevent charge separation, it is enough to add a *poloidal* component to the magnetic field, that is a component lying in the vertical cross section of the torus. The resulting field lines move both toroidally and poloidally and wrap around the torus, as shown in Fig.1.4, left. If the ratio of poloidal over toroidal revolutions is an irrational number, the field line will continue to wrap around the torus, but will never close on itself: it will instead ergodically cover a whole surface, known as *magnetic surface* or, for reasons explained in Sec.2.1.2, *flux surface* (alternatively, a flux surface is a surface on which the magnetic field line lies). The resulting magnetic field is made up of nested and non-intertwining flux surfaces.

To produce the toroidal field, it is sufficient to surround the torus with electric coils capable of sustaining very high currents. Such currents, flowing in the poloidal direction, will create a magnetic field along the toroidal one, in accordance to Ampere's law. In order to successfully confine a reactor grade plasma, the toroidal field must be very intense, usually above $1T$. Creating such a strong field is not immediate, since the resulting electromagnetic forces will induce strong stresses in the reactor's components.

The way in which the poloidal field is produced further distinguishes the two main can-

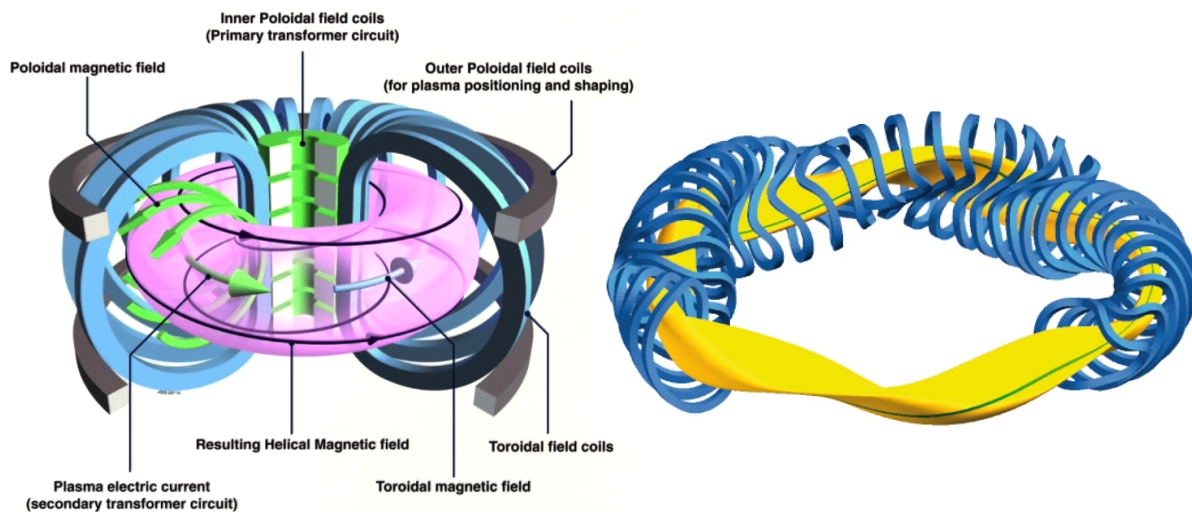


Figure 1.4: Left: scheme of a tokamak with coils and magnetic fields; taken from [5]. Right: scheme of a Stellarator (created by Max-Planck Institut für Plasmaphysik).

didates in MCF:

- The *Stellarator* (Fig.1.4, right) exploits coils with very complex geometry that will also create a poloidal field. This feature leads to the need of modelling the full 3D structure when studying the machine.
- In a simplified fashion, the *tokamak* (Fig.1.4, left) exploits a central solenoid placed in the middle of the torus as a *current drive*. This solenoid acts exactly as the primary winding of a transformer: an increasingly strong electric current flows through it, generating a time-varying magnetic field. Due to Faraday's law, an electric current is thus induced into the plasma, acting here as the secondary winding of the transformer. Finally, this current generates the poloidal field we need, which usually has much lower intensity than the toroidal one. Then, the poloidal field can be corrected with *external poloidal field coils*, useful to adjust the plasma's shape and position.

Since the current in the central solenoid cannot increase indefinitely, the machine cannot run continuously, but must operate in a pulsed manner. This limitation could be mitigated by exploiting additional and different current drive methods.

The tokamak configuration is, with good approximation, toroidally symmetric. As a consequence, it is often not necessary to study its whole 3D structure, but it is possible to limit the analysis to any 2D poloidal cross section, whose properties should be the same of any other toroidal location.

1.2.2. Open questions

Now that the fundamental requirements for a fusion reactor have been outlined, we can focus on those issues that still require a final solution. Given the extremely complicated nature of the problem, these questions are not related only to plasma physics, but also to other branches of science, engineering and economics. Here is given a small summary of the main issues [1]:

- Plasma control and behaviour

The heart of a reactor is of course the burning plasma, surely one of the most complex systems in nature. Plasma physics research is ongoing from a lot of different angles, in the effort to gain better control over it and to identify the best possible configurations in order to satisfy the very strict engineering constraints a reactor requires. Among the goals of this research we can find strategies for plasma heating and confinement, optimization of the plasma-wall interaction, mitigation of violent plasma turbulence and many others.

- Plasma-Wall Interaction

The heat flux on the nose of the space shuttle reentering atmosphere from space is about 5 MW/m^2 , lasting only some minutes. Some portions of a fusion reactor's walls will have to withstand fluxes of about 10 MW/m^2 [6] for years of operation. This already impressive heat flux could even increase in the event of major turbulent behaviour or even a *disruption*, i.e. a total loss of plasma, with all the stored energy impacting on the walls. This event would be deleterious for the wall conditions and must be avoided. Also, the harsh conditions at the plasma-wall interface can lead to excessive wall erosion and damaging, with consequent plasma pollution and loss of performance. For addressing these issues, there is ongoing research in both plasma physics and material sciences.

- Materials endurance and structure integrity

As we saw, MCF requires incredibly high magnetic fields and temperatures. This necessity translates to very high mechanical loads and thermal stresses on the materials of the vessel. Furthermore, fusion itself produces vast amounts of very energetic neutrons with the ability to deeply penetrate most materials (including steel) and thus reducing their mechanical and thermal performances over time, while also activating them (i.e. making them radioactive). This poses serious questions on the life expectancy of the vessel and of a number of more delicate parts, such as the superconductive coils.

- Fuel availability

In all realistic fusion power plants designs, the exploited reaction is between deuterium and tritium, both of which are hydrogen isotopes. Deuterium is stable and is present in nature with an isotopic abundance of 0.015%. It doesn't look like much, but it can be extracted with ease from water in virtually unlimited quantities. Tritium on the other hand is radioactive and, having a half life of about 12 years, is present in nature only in traces and its amount is not enough for it to be collected or exploited. The total amount of tritium actually stocked in the entire world is around 20 kg and its production relies on a particular type of fission reactor, mainly used in Canada [7]. The best solution is to produce the tritium at much higher rates, exploiting a nuclear reaction involving Lithium-3 and a neutron, in a process known as *tritium breeding*. Luckily enough, a fusion reactor exploiting the DT reaction is a massive generator of neutrons. If we could find an effective way to surround the plasma with a lithium *breeding blanket*, extract the tritium and use it as fuel, the problem would be solved. This kind of solution is still under study and, while promising, more research and testing have to be conducted.

- Electrical power production

Achieving a fusion plasma is a thing, getting electrical power out of it is another. While this goal can be obtained with well known thermodynamic cycles, already exploited in countless other fields, the details of an integration of the already existing technology in a tokamak have not been addressed yet.

Furthermore, a tokamak is an inherently pulsed machine, a feature that clearly introduces issues in the continuous generation on power we would like to achieve.

- Economical and political considerations

Even when we are in possess of all the scientific and technical knowledge to build a working reactor, its success from a commercial point of view will depend on its ability to produce power at a competitive price, the availability of investors, the political background, the general public's opinion and more.

1.2.3. Near and far future

Over the last 70 years, fusion research has made tremendous strides, laying a strong foundation for tomorrow's fusion reactors. Nevertheless, a lot of issues still require a deeper insight before we can see the first power plant up and running.

The next few years are going to be quite exciting for fusion research. The eyes of the scientific community are focused on ITER (Fig. 1.5), the world's largest tokamak currently under construction in Cadarache, France.

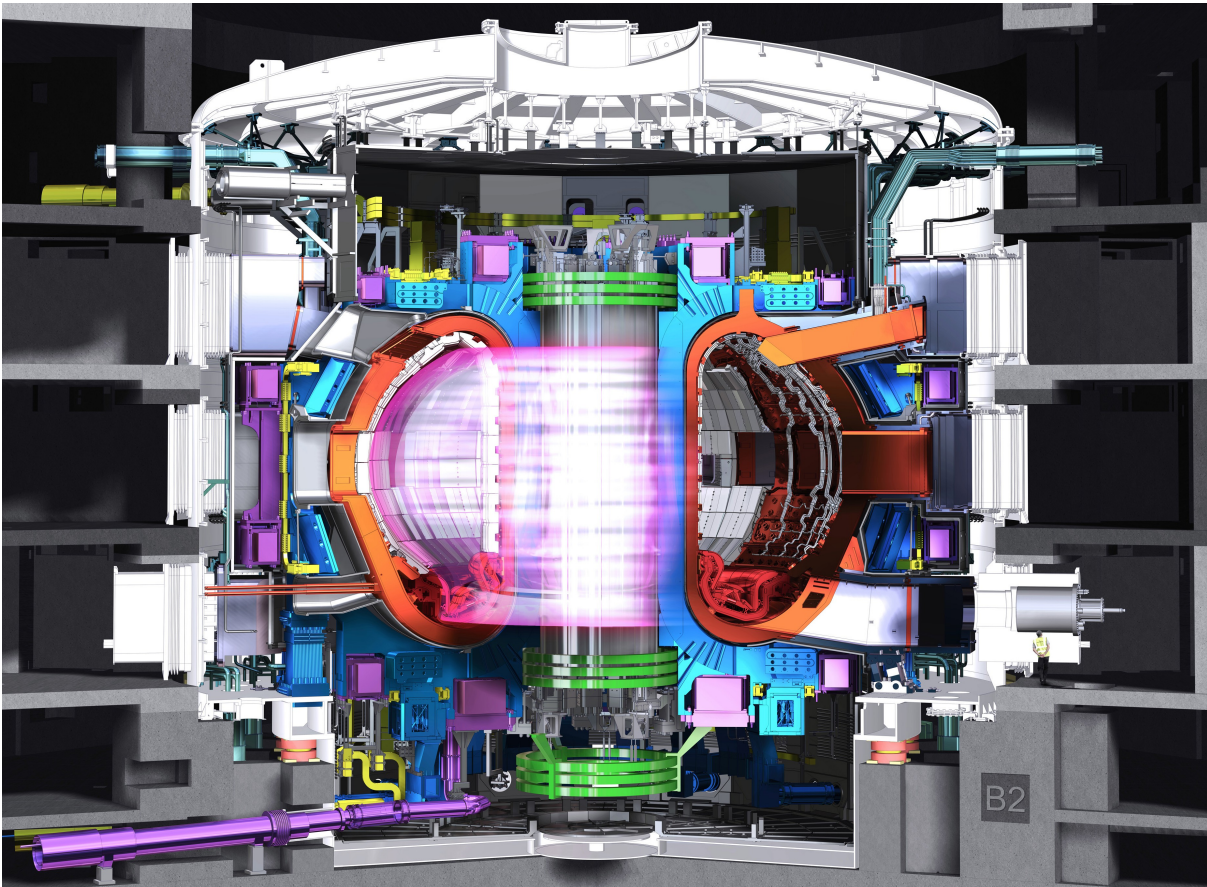


Figure 1.5: Scheme of the ITER tokamak. For scale, a man is represented in the bottom right corner.

ITER (International Thermonuclear Experimental Reactor) is going to be the result of a world-wide effort, directly supported by China, the European Union, India, Japan, Russia, South Korea and the United States to demonstrate the net production of energy in a magnetically confined fusion plasma. This tokamak aims in fact to achieve $Q > 10$ [8] (where Q is the ratio of the power produced by the plasma to the externally injected power) , paving the way for future commercial reactors.

Nevertheless, ITER is not going to produce electric power; its purpose is still inside the boundaries of research. Other goals of ITER include testing breeding blanket solutions, studying control of very large plasmas and scaling all current technology towards a reactor-grade dimension. Furthermore, it will demonstrate the safety of a fusion power plant and conduct extensive campaigns with DT plasmas, which are quite rare due to issues with tritium availability and radioactive activation of vessel components.

ITER was expected to achieve first plasma in 2025, but delays due to the Covid-19 pandemic and the discovery of manufacturing defects in some components will almost certainly move this milestone in the future. While unfortunate, delays are surely expected

when building a first-of-a-kind reactor, especially one as complex as ITER.

The knowledge acquired during ITER operation will contribute to the next-generation fusion machine, called DEMO. At this stage, it is not yet clear if DEMO will be a single international machine, or rather a collection of national projects. What is clear is its goal: DEMO will be the first prototype of a fusion power plant and it should achieve an higher energy output ($Q > 30$) [9], a nearly steady-state operation, a sufficient tritium breeding and an efficient way to collect energy and turn it into electric power [10]. In general, it will be a simpler machine with respect to ITER, less devoted to research and more focused on practical issues.

The final step will be the construction of commercial power plants. It is quite difficult to have a precise timeline, having to consider not only technical development, but also geopolitical factors; anyway, it is unlikely this will happen before the half of the century.

1.3. Thesis outline

The outline of this work is as follows: in Chapter 2 a deeper and necessary introduction to the concepts of plasma geometry, divertor, Scrape-Off Layer (SOL), filamentary turbulence, heat exhaust mechanism and detachment is given. Chapter 3 offers an overview of the Tokamak à Configuration Variable (TCV) and the main diagnostics used in this thesis. Chapter 4 shows the details of the experimental data analysis and the obtained results. Chapter 5 introduces a heuristic model as a possible bridge between the obtained results. Finally, Chapter 6 summarizes and concludes the work, suggesting possible future research.

2 | Overview of the plasma edge

Now that the basic working principles of a tokamak have been outlined, we have to describe in more detail a number of features that are either going to be further investigated or necessary to understand the following work. After an introduction to the tokamak geometry, the attention will be focused on the outer region of the plasma: the edge.

Far from being a simple boundary, the plasma edge is a crucial region connecting the hot and dense plasma core to the vessel walls. Several complex phenomena happen in this region and all of them must be well understood and controlled in order to maintain a high performance plasma and to preserve the first wall.

2.1. Plasma geometry

At a first glance, the behaviour of a plasma inside a tokamak appears to be obscure and not understandable with ease. This is somewhat true, and it is helpful to set up a proper geometric description of the machine, starting by considering the motion of single charged particles.

As a first approximation, each plasma particle moves following the magnetic field lines. Since $B_{tor} \gg B_{pol}$, particles complete a certain number of toroidal revolutions before they complete a full poloidal one. This number is called *safety factor* and is computed as:

$$q = \frac{1}{2\pi} \oint \frac{B_{tor}}{RB_{pol}} dl_{pol} \quad (2.1)$$

Since the magnetic lines are closed on themselves, particles should then be confined for an unlimited amount of time. Of course, this cannot be true: the confinement provided by magnetic fields is not perfect. A plasma is a complex system made up by countless particles constantly interacting with one another and giving rise to collisions, drifts, diffusion processes and fast turbulence phenomena, so it shouldn't come as a surprise that particles are able to gradually move outwards, escape confinement and hit the walls. It is not a matter of *if* or *when*, but of *where* and *how much*.

2.1.1. Limited and diverted geometry

As we saw, plasma particles move much more in the direction along the field lines than they do in the transverse direction. This means that if the wall features a protrusion, it will effectively limit the whole plasma, because all escaping particles, moving fast along the field lines, will intercept the protrusion before being able to move a lot outwards.

A plasma in this arrangement is called *limited*, while the solid object is known as *limiter* and can be both a poloidal or toroidal protrusion. This approach is depicted in Fig.2.1a.

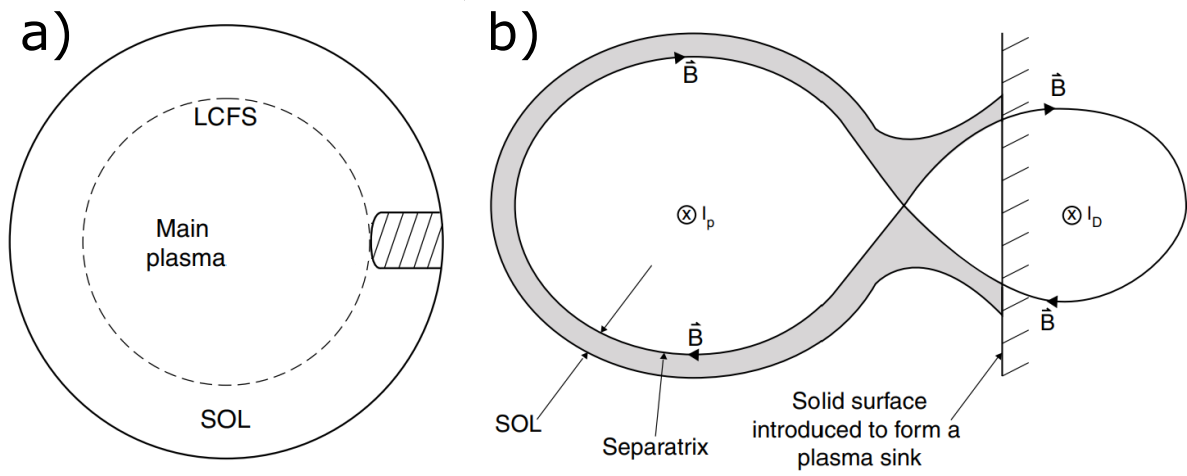


Figure 2.1: a) Poloidal cross section of a limited plasma: a toroidal limiter (shaded area) protrudes from the wall and creates a LCFS. b) Poloidal cross section of a diverted plasma: an external current creates an X-point and relative separatrix. Highlighted in grey is the Scrape-Off Layer. Both figures have been adapted from [11].

The protrusion of the limiter into the plasma identifies an important surface, called *Last Closed Flux Surface* (LCFS). The magnetic field lines inside the LCFS are totally confined in this region, known as *main plasma*. When particles cross the LCFS they start moving along field lines with a dead end into the wall. For this reason the plasma density and temperature exponentially decreases as we get far from the LCFS and this region is called *Scrape-Off Layer* (SOL).

A limited plasma has the possibility of spreading the plasma-wall interaction on a very large surface, just by shaping the plasma to match the walls contour, thus reducing the heat fluxes to the vessel. The main drawback of this strategy is a high contamination of the plasma, due to the sputtering of the wall's particles caused by the highly energetic plasma particles hitting the vessel.

Plasma contamination can easily reduce fusion performances because considerable amount of energy would be lost via bremsstrahlung. The amount of energy radiated in this way is

proportional to the second power of the impurity atomic number: this explains why even a small amount of heavy impurities from the wall can deeply affect the power balance. For this reason it is preferred to move the plasma-wall interaction region away from the main plasma, in a configuration known as *diverted* (Fig.2.1b).

To obtain a diverted geometry it is sufficient to exploit a second poloidal current, flowing in the same direction as the main one, but located outside the walls. This will again create a main plasma and a SOL but the line between the two is not called *separatrix*. This separatrix always meets itself in the so-called *X-point*, i.e. the point in which the poloidal field is zero. Between the X-point and the wall, the SOL extends into two *legs*, while the region in between these legs is called *private plasma*.

The price to pay for such an arrangement is that the small portion of walls now interacting with the plasma (i.e. the *divertor*) is subject to very high heat and particle fluxes that must be carefully managed to minimize deterioration of the divertor itself. Another drawback is the less efficient exploitation of the available volume, leading to increased costs.

In most cases, including this thesis, the terms *LCFS* and *separatrix* are interchangeable and will be used regardless of the actual plasma configuration.

2.1.2. Coordinate system

While using a cylindrical coordinate system (defined by the right-handed orthonormal triplet (R, Φ, Z)) to analyze the poloidal cross section is possible and often useful, when it comes to describe plasma properties that are changing from the core of the main plasma to the SOL, this is no longer effective and a different kind of coordinate, one that is independent from the particular plasma shape, is preferred.

To define such a coordinate we start from the Maxwell equation $\nabla \cdot \mathbf{B} = 0$, which enables us to write the magnetic field as the curl of a vector potential: $\mathbf{B} = \nabla \times \mathbf{A}$. Exploiting the tokamak axisymmetry this relation becomes:

$$\mathbf{B} = -\frac{\partial A_\Phi}{\partial Z} \hat{\mathbf{R}} + \frac{1}{R} \frac{\partial(RA_\Phi)}{\partial R} \hat{\mathbf{Z}} + \left(\frac{\partial A_R}{\partial Z} - \frac{\partial A_Z}{\partial R} \right) \hat{\Phi} \quad (2.2)$$

The right hand side of Eq.2.2 has three terms: the last one is the toroidal magnetic field, while the first two sum up to give the poloidal field. Since these both depend on A_Φ it is convenient to introduce a function $\Psi(R, Z) = 2\pi RA_\Phi(R, Z)$, so that the components of the poloidal field become:

$$B_R = -\frac{1}{2\pi R} \frac{\partial \Psi}{\partial Z} \quad (2.3a)$$

$$B_Z = \frac{1}{2\pi R} \frac{\partial \Psi}{\partial R} \quad (2.3b)$$

The theory of *MagnetoHydroDynamics* (MHD) is a very powerful tool for the study of quasi-stationary plasmas. Without giving a full explanation of this theory (for further details see [1, 3]), we can focus on one of the ideal MHD equilibrium equations, which states that in a magnetically confined plasma the magnetic forces must counterbalance the pressure forces:

$$\mathbf{J} \times \mathbf{B} = \nabla p \quad (2.4)$$

If we take the dot product of Eq.2.4 with \mathbf{B} and then \mathbf{J} we find $\mathbf{B} \cdot \nabla p = 0$ and $\mathbf{J} \cdot \nabla p = 0$, meaning that the magnetic field lines and the current must both lie on surfaces of constant pressure. Since we know from Sec.1.2.1 that a single field line always lies on the same flux surface, we just proved that every flux surface is a surface of constant pressure and cannot be crossed by currents. Exploiting Eqs.2.3 we can easily prove that $\mathbf{B} \cdot \nabla \Psi = 0$, which means that also Ψ is constant on a whole flux surface.

All these observations make Ψ the perfect candidate for building a coordinate describing variations in the plasma as we move from the core to the edge.

To give physical meaning to Ψ we can refer to Fig.2.2, where two arbitrary flux surfaces (labeled as Ψ_1 and Ψ_2) are shown. On the poloidal plane we can connect

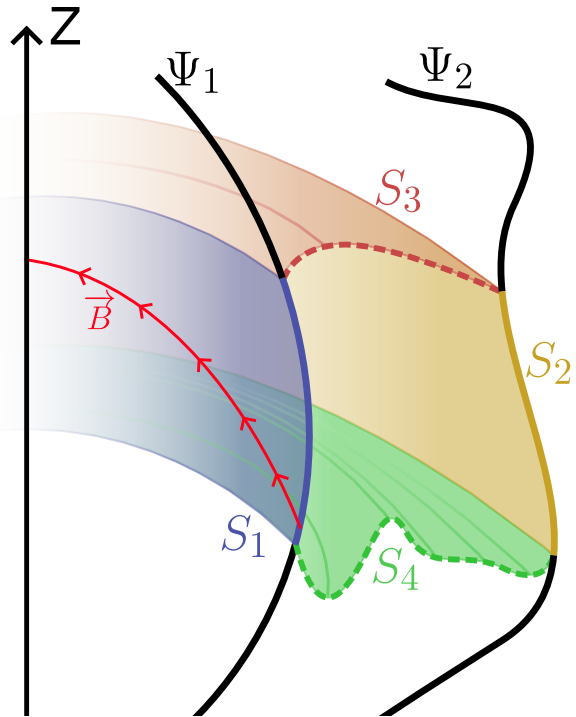


Figure 2.2: Scheme of two flux surfaces with two arbitrary toroidal ribbons connecting them.

these surfaces with two random paths, that are then projected toroidally around the Z axis. As a result we get 4 surfaces: S_1 and S_2 are portions of the original flux surfaces, while S_3 and S_4 are toroidal "ribbons" connecting the two surfaces.

We wish to compute the flux of the magnetic field across the total surface S ; exploiting the divergence theorem and Gauss theorem we find: $\iint_S \mathbf{B} \cdot \hat{n} dS = \iiint_V \nabla \cdot \mathbf{B} dV = 0$. The flux on S_1 and S_2 must be 0, since we know the magnetic field lies on flux surfaces without crossing them; also, considering how S_3 and S_4 have been built, it is clear that the flux of the toroidal field will be zero on them. These considerations lead to an important result: $\iint_{S_3} \mathbf{B}_{pol} \cdot \hat{n} dS_3 = \iint_{S_4} \mathbf{B}_{pol} \cdot \hat{n} dS_4$, where we reversed the sign of one of the versors \hat{n} so that they both point in the same direction. This result means that it does not matter how we choose the original profile, the flux of the poloidal field across a ribbon will always be the same.

We can now compute this flux by choosing a convenient ribbon, defined by two points having same Z, but different R: one located on Ψ_1 , the other on Ψ_2 . Then we connect these points with a straight line and project it toroidally: the resulting ribbon is a flat surface with a normal versor \hat{n} always pointing along Z. As a result only the Z component of the field will contribute to the flux. Thus we find, exploiting Eq.2.3b:

$$\iint_S \mathbf{B}_{pol} \cdot \hat{n} dS = \int_{R_1}^{R_2} B_Z(R, Z) 2\pi R dR = \int_{R_1}^{R_2} \frac{1}{2\pi R} \frac{\partial \Psi}{\partial R} 2\pi R dR = \Psi_2 - \Psi_1 \quad (2.5)$$

Eq.2.5 is the reason why Ψ is actually called *poloidal flux function* and the magnetic surfaces are also called flux surfaces.

It can be shown that Ψ is arbitrary to an additive constant, and the choice is made so that $\Psi_{LCFS} = 0$. We can now identify the whole poloidal magnetic field as a set of nested surfaces of constant Ψ . The innermost surface, i.e. a single line circumnavigating the tokamak, is known as *magnetic axis*.

Finally, the new coordinate we were looking for is then defined as:

$$\rho_\Psi = \sqrt{\frac{\Psi - \Psi_0}{\Psi_{LCFS} - \Psi_0}} = \sqrt{1 - \frac{\Psi}{\Psi_0}} \quad (2.6)$$

Where Ψ_0 is the value of the poloidal flux function on the magnetic axis, so that ρ_Ψ is 0 on it and 1 on the LCFS. The final result is depicted in Fig.2.3. We can clearly see that the red surface separates the main plasma, for which all flux surfaces are closed, from the SOL, where flux surfaces are open and intercept the walls.

2.1.3. Plasma shaping and triangularity

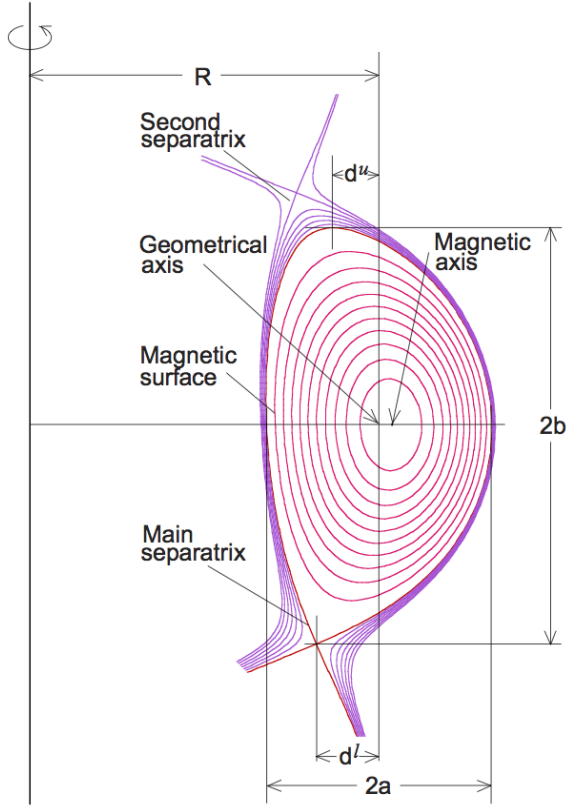


Figure 2.3: Plasma geometry. The red line is the LCFS (or separatrix). Closed flux surfaces are shown in pink, open ones are purple. Taken From [12].

triangularity describes a deformation into a "D" shape (or "reverse-D", for negative values) and, as pointed out by Eqs. 2.7b-d can be defined separately for the upper and lower portions of the plasma.

To give an example of the triangularity effect, Fig.2.4 shows a comparison of three different cases.

When non-circular shapes were being studied in the late 1960s, the scientific community found out that positive triangularity (PT) plasmas yielded better performances when compared to circular plasmas, while negative triangularity (NT) plasmas were quickly discarded on the basis of poor stability [13].

During the last 30 years, investigation of NT plasmas has found renovated interest: in the rest of this Chapter, the documented role of δ in each presented phenomenon will be

Over the years, researchers found that the plasma shape has strong influence on confinement level, so that a simple circular cross-section has been deformed into a more complex geometry. To quantify the introduced distortion, the most important parameters are called *elongation* (κ) and *triangularity* (δ) and, with reference to Fig.2.3 are defined as:

$$\kappa = \frac{b}{a} \quad (2.7a)$$

$$\delta_u = \frac{d_u}{a} \quad (2.7b)$$

$$\delta_l = \frac{d_l}{a} \quad (2.7c)$$

$$\delta = \frac{d_u + d_l}{2} \quad (2.7d)$$

Elongation describes the distortion of a circular cross section into an ellipse, while

triangularity describes a deformation into a "D" shape (or "reverse-D", for negative values) and, as pointed out by Eqs. 2.7b-d can be defined separately for the upper and lower portions of the plasma.

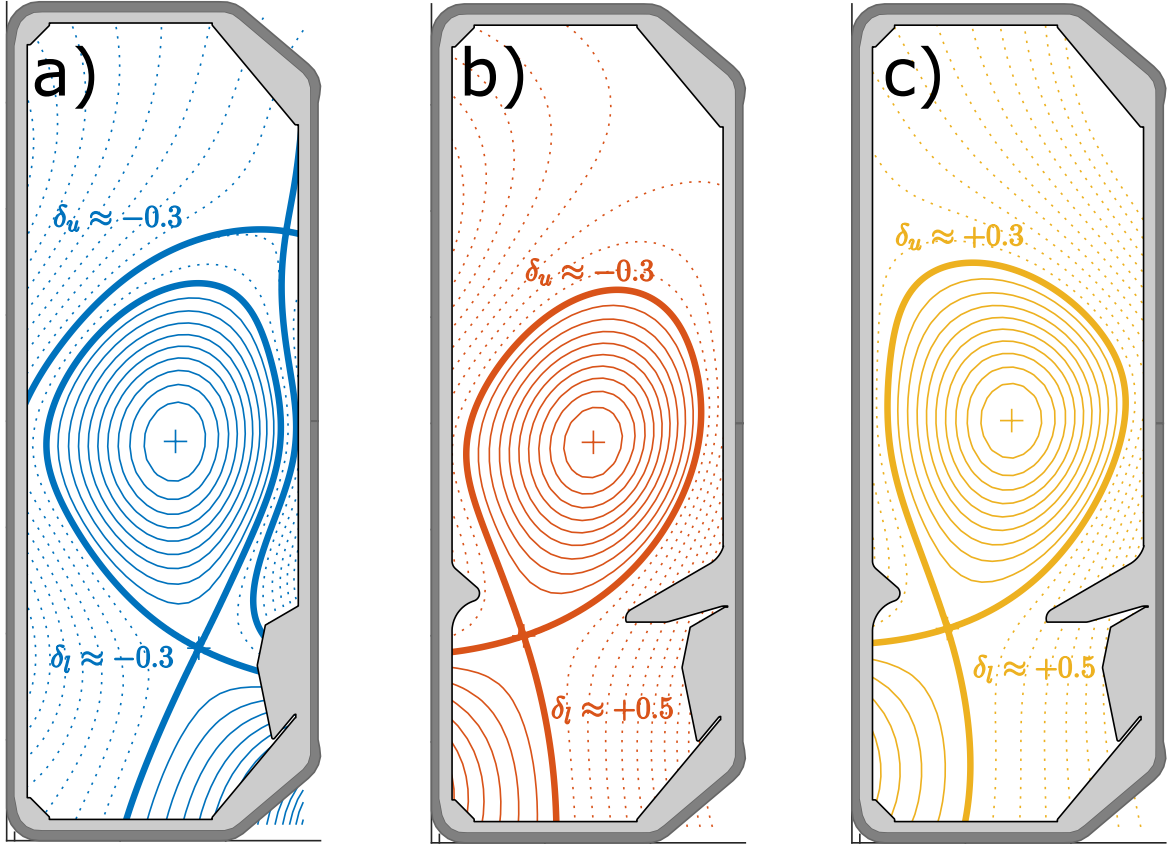


Figure 2.4: Comparison of different triangularity plasmas. a) $\delta_u < 0$ and $\delta_l < 0$. b) $\delta_u < 0$ and $\delta_l > 0$. c) $\delta_u > 0$ and $\delta_l > 0$. Note the different legs positions for changing lower triangularity.

underlined. A quick summary is also given in Sec.2.6.

2.1.4. Scrape-Off Layer geometry

Introduced in Sec.2.1.1, the SOL has a fundamental role in a fusion reactor. Both in limited and diverted configurations, it connects the main plasma to the vessel walls. This section summarizes its most basic geometric properties in the diverted case.

When a charged particles crosses the LCFS, it will find itself moving along a particular field line in the SOL. Before hitting the wall, since the $B_{tor} \gg B_{pol}$, it will circle around the torus for a number of times, travelling a quite long distance that takes the name of *connection length* ($L_{||}$) and its value is in the order of the tens of meters. Of course the exact value of $L_{||}$ depends on the particular location in which the particle entered the SOL.

For convention, we always measure the connection length from a location called *midplane*,

defined as the point on the LCFS having a vertical tangent line in the poloidal cross-section. Also other relevant quantities such as plasma density and temperature are usually taken at the midplane. Since the flow of particles is directed from the main plasma to the walls, we usually refer to the midplane as the *upstream* region and to the wall as the *target* region.

When the particles reach the target, they hit it at an angle γ resulting from the relative orientation of the magnetic field and the wall, as shown in Fig.2.5b.

For reasons that will be clarified in Section 2.3, it is important to also introduce the angle β_{pol} between the poloidal field and the wall (Fig.2.5a).

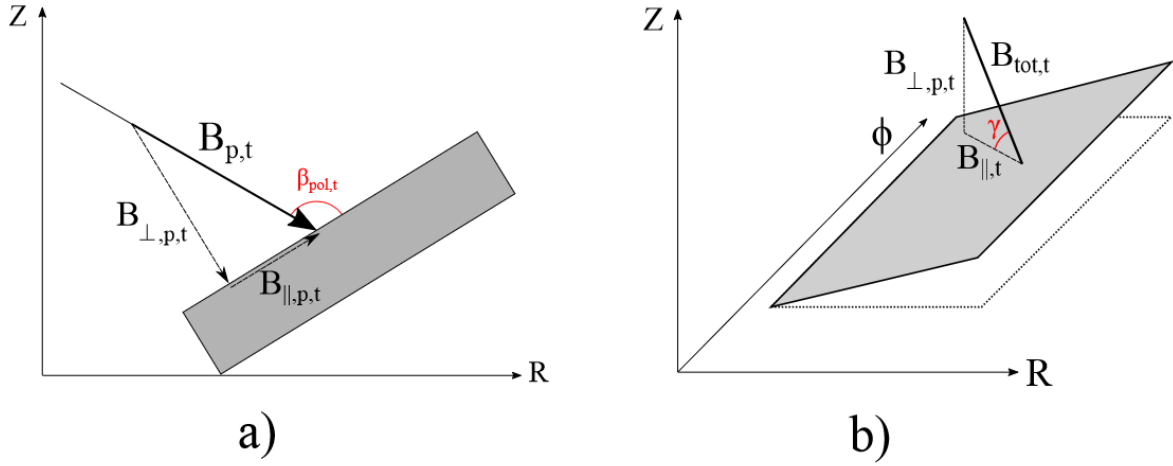


Figure 2.5: Orientation of magnetic field at the target. Picture taken from [14].

Along the SOL the relative distance among flux surfaces can vary quite a lot as we move from the midplane to the target, passing through the X-point. The reason is that the poloidal field itself is subject to great variations (this is clear if we consider that at the X-point we have $B_{pol} = 0$).

This effect is easily described by the *poloidal flux expansion* $f_{x,pol}$, defined as the ratio of the distances of two flux surfaces, measured at the location of interest and upstream.

From Eqs.2.3 we can easily find $|\nabla\Psi| = 2\pi RB_{pol}$. If dr is the distance between the two surfaces, $d\Psi = |\nabla\Psi|dr = 2\pi RB_{pol}dr$ and we obtain (on the target):

$$f_{x,pol} \equiv \frac{dr_t}{dr_u} = \frac{R_u B_u^{pol}}{R_t B_t^{pol}} \quad (2.8)$$

2.2. Plasma confinement modes

Achieving a burning plasma requires the ability to reach a good grade of confinement. The most relevant parameter in this respect is the energy confinement time, defined as the ratio of the total energy content of the plasma over the energy flow leaving the plasma. If this is high enough, the plasma is able to efficiently confine its own energy and to possibly reach reactor conditions. The entire history of fusion research has been led by the goal of increasing the confinement level of our machines, by understanding and mitigating those mechanisms that could lead to excessive energy dissipation, such as accumulation of impurities in the main plasma or strong turbulent phenomena.

Sometimes important breakthroughs are achieved when you are not looking for them. This is what happened in 1982 in Germany, during an ordinary plasma experiment performed in the ASDEX tokamak. Halfway through the shot, plasma parameters suddenly and drastically changed, with the energy confinement time doubling in value and the plasma edge turbulence disappearing. This fortuitous event led to the discovery of the so called *H-mode*, while the old, ordinary, mode was renamed *L-mode* [15]. These names were chosen to reflect the level of confinement displayed by the two modes: respectively high and low.

The discovery ignited vast enthusiasm in the fusion community and H-mode quickly became the leading option for a working reactor. Despite the increased confinement, an H-mode plasma is interested by non-negligible issues that are absent in similar L-mode plasmas [16]. The increased confinement observed in H-mode is a consequence of the formation of a *transport barrier* close to the separatrix. This thin layer is characterized by very low transport coefficients, thus reducing particle and energy fluxes to the SOL. The result is an achievement of a denser and hotter core, featuring higher confinement times; but at a price. H-mode can exist only if the power entering the plasma is higher than the *L-H power threshold*; the increased confinement also favors impurity retention in the core and, most importantly, much steeper density and temperature gradients develop across the transport barrier. Said gradients are so high that they quickly become unstable, resulting in a new type on plasma instability: the *Edge Localized Modes* (ELMs). An ELM consist of a violent loss of particles and energy from the core, with possible damages for the vessel walls. The most powerful ELMs, happening in a device of the size of ITER, would have deleterious consequences for both the divertor targets and plasma contamination [17, 18]. ELM mitigation is in fact an open field of research.

There are various indications at the occurrence of an L-H transition. Usually a drop in the D_α radiation, combined with an increase of the core density is sufficient proof the

transition has happened.

As a consequence of these complex H-mode implications and in the light of new findings regarding negative triangularity plasmas, in recent years L-mode research has found renewed interest. In particular, there is compelling evidence that NT L-mode plasmas can achieve confinement levels comparable or even superior to equivalent positive triangularity H-mode plasmas, as shown in [19] for $\delta = \pm 0.4$. In particular, it is reported both an increase in τ_e and a reduction in core turbulence. As a result the level of additional heating required to achieve the same conditions of a PT plasma is greatly reduced [20, 21]. Furthermore, studies report a suppression of edge turbulence for NT plasmas [22, 23]. A concern about L-mode operation is that the high power required for ignition would cause the plasma to transition into H-mode; however, studies on DIII-D and TCV showed that the L-H power threshold is much higher in negative triangularity than in equivalent positive triangularity plasmas [21, 24].

Overall, these findings provide a basis to question the choice of a PT H-mode reactor and underline the need of further studies in NT L-mode plasmas.

2.3. Divertor heat exhaust

As mentioned before, one of the main concerns for a future reactor is how the huge heat fluxes to the divertor will be managed. If the power will turn out to be concentrated on a thinner region than anticipated, it will pose a serious concern for the divertor life expectancy.

It is therefore essential to achieve the best possible understanding of the heat exhaust physics: this section will present the fundamental aspects.

When plasma particles cross the LCFS, they start travelling along open field lines moving rapidly towards the target. The parallel motion is much more pronounced than the cross field one, that, however, is at play. The result is a very high parallel heat flow, confined in a very narrow layer (a few cm) close to the LCFS.

While travelling towards the target, plasma particles pass through very different regions: at first they are moving along the denser plasma core that continues to inject particles into the SOL, but after passing the X-point they move along the private plasma region, which features a very low density: the resulting density gradient causes the particles to diffuse back through the LCFS into the private region itself.

We are interested in the parallel heat flux profile across the SOL, evaluated as a function of the distance from the separatrix. In a small thought experiment we can imagine to "follow" this profile as it travels along the field lines from midplane towards the divertor

target:

- We can assume that in the upstream region (i.e. the outer midplane) the heat flux has an ideal exponential profile with fall-off length λ_q [25]:

$$q_{||,u}(dr_u) = q_{0,u} \cdot e^{-\frac{dr_u}{\lambda_{q,u}}} \quad (2.9)$$

Where $dr = r - r_{sep}$ is the radial distance from the separatrix, while the subscript u stands for *upstream* (Fig.2.6 top).

- After passing the X-point, the plasma will diffuse in the private region. This effect has been modeled by Eich [26], convoluting the exponential profile with a Gaussian function having width S . This parameter, also called *power spreading factor* describes the intensity of the particles diffusion and is directly related to the connection length between the X-point and the target and the competition between parallel and perpendicular heat diffusion: $S = l_x \sqrt{\frac{\chi_{\perp}}{\chi_{||}}}$ [27, 28]. This yields, on the target:

$$q_{||,t}(\bar{s}) = \frac{q_{0,t}}{2} \exp \left[\left(\frac{S_t}{2\lambda_{q,t}} \right)^2 - \frac{\bar{s}}{\lambda_{q,t}} \right] \operatorname{erfc} \left(\frac{S_t}{2\lambda_{q,t}} - \frac{\bar{s}}{S_t} \right) + q_{bg} \quad (2.10)$$

Where the subscript t stands for *target*, erfc is the *complementary error function*, q_{bg} accounts for background and $\bar{s} = s - s_0$ with s being a curvilinear coordinate on the target and s_0 the LCFS position.

- As a first approximation particles move following the field lines; so, the geometry of the magnetic field is deeply related to the heat flux profile and this dependency takes essentially two forms:

1. If the divertor is placed further outwards with respect to the midplane, the strength of the total magnetic field will be lower and the power will be diluted in a higher volume. To quantify this effect we can rely on a simple MHD property: in any flux tube the magnetic field flux is conserved. Considering that $B_{tor} \gg B_{pol}$, we can write: $A_u \cdot B_u^{tor} = A_t \cdot B_t^{tor}$.

Assuming no heat sources or sinks in the SOL (not valid in detached divertor conditions), also the total heat flow is conserved: $q_{||,u} \cdot A_u = q_{||,t} \cdot A_t$.

Combining these results and considering that $B_{tor} \propto 1/R$ we obtain:

$$\frac{q_{||,u}}{q_{||,t}} = \frac{A_t}{A_u} = \frac{B_u^{tor}}{B_t^{tor}} = \frac{R_t}{R_u} = f_x \quad (2.11)$$

Where f_x is the *total flux expansion*.

2. In a poloidal cross section, if the flux surfaces grow further apart from each other, also the heat flux profile will spread following them, so the parameters λ_q and S will be directly affected. As shown in Section. 2.1.4, this effect is described by the poloidal flux expansion $f_{x,pol}$ (Eq.2.8).
- An intelligent way to spread the heat flux to the target on a larger area, is to tilt the divertor so that the angle of incidence becomes quite low. With reference to Fig.2.5a, we see that the heat flux is now spread over a length $d\bar{s} = dr_t / \sin \beta_{pol,t} = dr_u \cdot f_{x,pol} / \sin \beta_{pol,t}$. To account for this we can define an *effective poloidal flux expansion*:

$$f_{x,pol}^* = \frac{f_{x,pol}}{\sin \beta_{pol,t}} \quad (2.12)$$

It must be kept in mind that this strategy, while effective, is limited by engineering constraints related to the fact that the target is not a single piece of material, but is usually made up of a lot of carefully aligned tiles. To accommodate thermal expansion and to make their installation easier, the tiles are separated by a small gap. If the grazing angle becomes too small, the exposed edges of the tiles would actually be subject to higher heat fluxes and deteriorate quickly.

A summary of these mechanisms is represented in Fig.2.6.

The convention when dealing with heat exhaust, is to measure the heat flux to the target and then rescale it at the midplane. This allows to get rid of flux expansion effects, even if it introduces some non-intuitive concepts, such as a power spreading factor defined upstream S_u , when this parameter is actually introduced to describe a behaviour happening between the X-point and the target.

Exploiting Eqs. 2.10, 2.11, 2.12 and the relation $\bar{s} = dr_u \cdot f_{x,pol}^*$, we finally obtain:

$$q_{||,t}(dr_u) = \frac{q_{0,u}}{2f_x} \exp \left[\left(\frac{S_u}{2\lambda_{q,u}} \right)^2 - \frac{dr_u}{\lambda_{q,u}} \right] \operatorname{erfc} \left(\frac{S_u}{2\lambda_{q,u}} - \frac{dr_u}{S_u} \right) + q_{bg} \quad (2.13)$$

We note that in Eq.2.13 there is not an explicit appearance of $f_{x,pol}^*$. The reason is that we are expressing $q_{||,t}$ directly as a function of dr_u , if we wanted to use \bar{s} we would recover

it.

In the following I will always consider $\lambda_{q,u}$ and S_u , calling them simply λ_q and S , unless otherwise specified. These are the most significant parameters in the Eich function, describing the extension of the heat deposition area. To get a unified estimate of such extension, we can compute the *integral decay length* [29]:

$$\lambda_{int} = \frac{\int (q_{||}(x) - q_{bg}) dx}{q_{||,max}} \quad (2.14)$$

As shown in [30], Eq. 2.14 can be approximated as:

$$\lambda_{int} = \lambda_q + 1.64 \cdot S \quad (2.15)$$

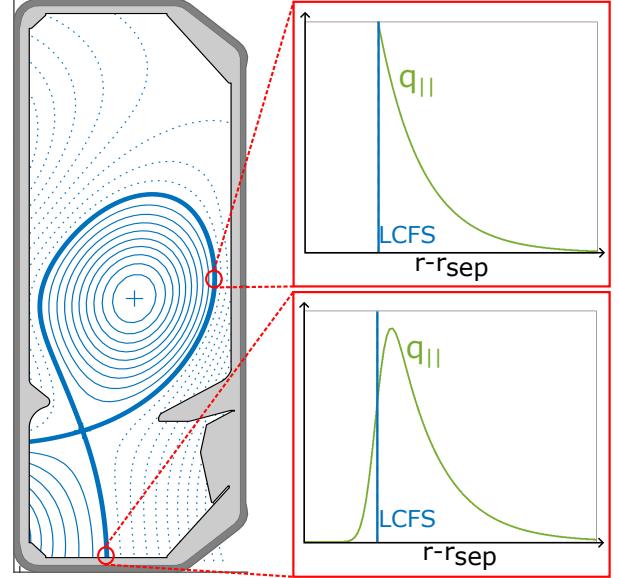


Figure 2.6: Evolution of the heat flux profile from upstream to the divertor target

Given the practical importance of correctly estimating λ_q , a number of models and scaling laws have been proposed over the years. An overview of some of these, valid for L-mode plasmas, is presented in Table 2.1. Eich and Scarabosio laws are quite similar and their most relevant parameter is the poloidal magnetic field or, equivalently, the plasma current (even though this dependence is quite hidden inside the safety factor). Brunner and Silvagni laws are very simple, describing λ_q only through the pressure. Counter intuitively, it looks that the average plasma pressure correlates to λ_q better than the localized edge electron pressure [31]. Horacek-E3 and Lim law also take triangularity into account, both predicting an increase of the fall-off length with δ . This result is consistent with the experimental observation [32] and constitutes one of the worst drawbacks of NT plasmas, even though this configuration would move the heat deposition area to larger radii, making it larger.

Author	Correlation	Notes
Eich [33]	$1.37 \cdot B_{tor}^{-0.55} q_{cyl}^{1.17} P_{SOL}^{0.2} R^{0.1}$ $q_{cyl} = \frac{2\pi a^2 B_{tor}}{R\mu_0 I_p} \frac{1+\kappa^2}{2}$	L-mode JET,AUG
Scarabosio [34]	$1.44 \cdot B_{tor}^{-0.8} q_{95}^{1.14} P_{SOL}^{0.22} R^{-0.03}$	L-mode JET,AUG
Brunner [35]	$0.91 \cdot \bar{p}^{-0.48}$	L,H,I-mode C-Mod
Silvagni [36]	$2.45 \cdot p_{e,95}^{-0.34}$	L,H,I-mode AUG
Horacek D1 [37]	$2800 \cdot \epsilon^{-1.03} f_{gw}^{0.48} J^{-0.35}$	L-mode JET,EAST,MAST, C-Mod,COMPASS only outer target
Horacek E3 [37]	$44000 \cdot \delta_u^{0.45} f_{gw}^{0.34} J^{-0.6}$	L-mode JET,EAST, C-Mod,COMPASS both targets
Lim [38]	$0.27 \cdot 1.95 \cdot C^{9/17} A^{1/17} q^{12/17} \cdot R^{7/17} P_{SOL}^{-4/17} n_e^{10/17} B_{tor}^{-12/17} L_X^{12/17}$	L-mode JET,MAST,C-Mod, AUG,COMPASS,TCV analytical theory-based

Table 2.1: Some scaling laws for λ_q (all results are expressed in mm). Other work, only based on H-mode plasmas, is here omitted. All quantities are evaluated in SI units, with the following exceptions: P_{SOL} [MW], \bar{p} [atm], $p_{e,95}$ [kPa], n_e [$10^{19} m^{-3}$]. In Lim's scaling law, C and L_X are geometrical parameters, depending also on triangularity [38]. The "Notes" column contains indications on the confinement mode under investigation, the tokamaks where data came from and eventual other details.

It must be noted that, while the Eich function does a satisfying job in fitting the heat flux profile, its description is not perfect, especially in the areas far from the separatrix. For example, it has been pointed out that a "multi- λ fit" can better describe the profile [35]. This comes at the price of introducing more fitting parameters and it is not based on a clear physical explanation as the Eich function is, but it underlines an important fact: the tails of the heat-flux profile tend to fall off at a lower pace with respect to the centre of the peak and this hints at the investigation of a different physical mechanism. This thesis

tries to explain (at least partly) this behaviour with the presence of filamentary turbulence in the edge of the plasma. a heuristic model, based on experimental observations, is presented in Chapter 5 for this purpose. While the connection of the far-SOL profiles with edge turbulence is being explored [39, 40], a final conclusion has yet to be obtained; the mechanisms studied in this work could give useful insights towards a better understanding of these phenomena.

2.4. Scrape-Off Layer turbulence

The SOL, far from being a stable steady-state system, is usually interested by different kind of turbulent phenomena. Among these, there is a frequent formation and expulsion of *filaments* [41–43]. These are coherent plasma structures, characterized by higher density and temperature than the surrounding plasma, that form close to the LCFS and are expelled outwards through the SOL with radial velocities $v_r \approx 1$ km/s. The filaments are much more extended in the toroidal direction (~ 1 m) than they are in a poloidal cross-section (~ 1 cm), in which they usually appear elliptical. For this reason they are also known as *blobs*.

Blobs are generated close to the separatrix thanks to instabilities driven by gradients in pressure and magnetic fields. Also, the presence of charge dependent drifts leads to charge separation in the plasma. As a consequence, a density ripple can form, featuring opposite charge accumulation on its boundaries, which in turn results in a poloidal electric field. The latter couples with the toroidal magnetic field, generating an $\mathbf{E} \times \mathbf{B}$ drift that pulls the emerging blob outwards. As long as the charge separation in the blob persists, the whole structure is dragged outwards by the $\mathbf{E} \times \mathbf{B}$ drift, hence the very high radial velocity $\mathbf{v}_r = \frac{\mathbf{E} \times \mathbf{B}}{B^2}$. This blob formation mechanism can be visualized in Fig.2.7.

It has to be noted that the direction of the radial velocity is always pointing outwards: an inversion of the magnetic field would in fact invert the charge-dependent drifts and the polarization inside the blob would be opposite, resulting in an identical radial velocity.

Charge separation turns out to be crucial for understanding the blobs dynamics. The radial velocity of a blob, depends in fact on the availability of current closure paths, that regulate the recombination of the charge and so the reduction of the $\mathbf{E} \times \mathbf{B}$ drift. Said paths can take different forms according mainly to the blob size and the plasma collisionality. For example if a blob is connected all the way to a wall, the solid surface offers a chance for current closure; or if the blob is disconnected in the vicinity of the X-point due to excessive magnetic shear, the current-closure path will be different. Overall, 4 different regimes can be identified, according to the *Two-Region Model* [42, 44].

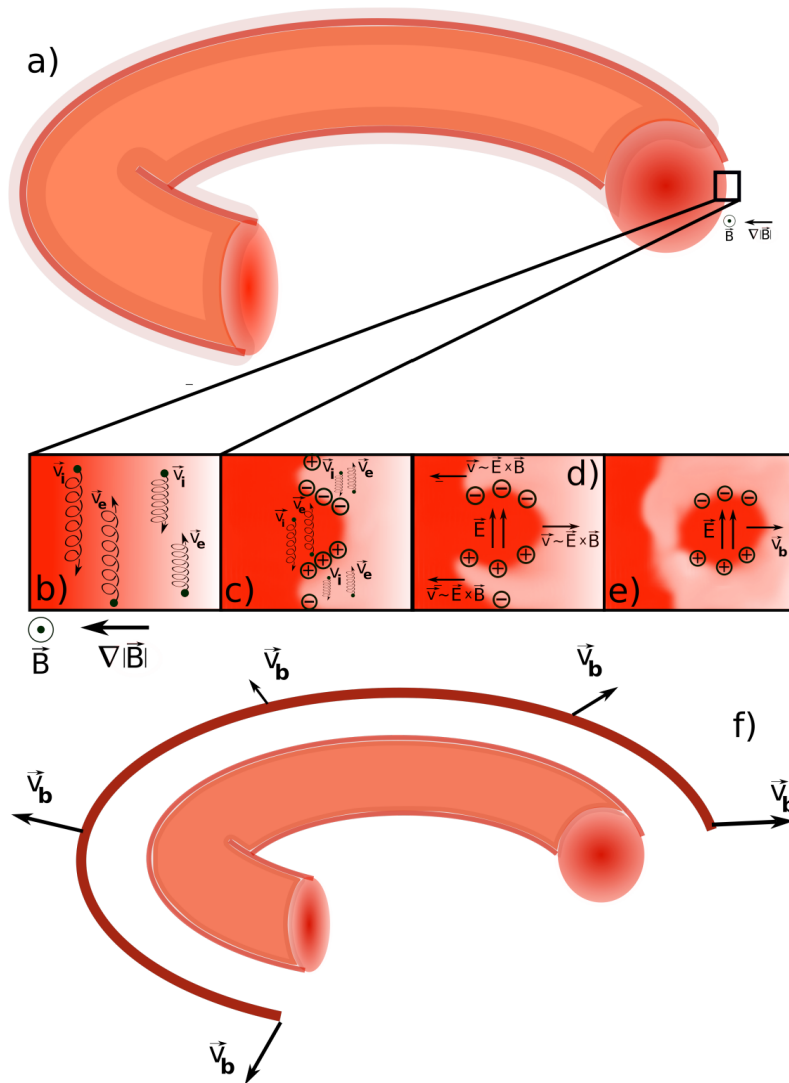


Figure 2.7: Formation mechanism of the filaments. a) Sketch of the plasma and direction of the magnetic field and its gradient. b) Charge dependent drifts (grad-B drift and curvature drift) leading to charge separation. c) Formation on a density ripple, featuring charge separation. d) Coupling of the poloidal electric field with the toroidal magnetic field, leading to an $\mathbf{E} \times \mathbf{B}$ drift. e) $\mathbf{E} \times \mathbf{B}$ drift dragging the blob outwards. f) Full sketch of a filament. Picture taken from [14].

A relevant question when it comes to blobs is whether or not they are connected all the way from midplane to the divertor. Answering is not straightforward for a variety of reasons. First of all, measuring the along-field extension of a filament is not an easy task: at best we can find evidence that a blob is connected between the locations of 2 different diagnostics, the signals of which are subject to a cross-correlation analysis. Such a technique is exploited in [45], in which is found that filaments in the far SOL

($\rho_\Psi > 1.05$) seem to always be connected to the divertor region, while closer to the separatrix it depends on the particular blob regime. The intense flux expansion [46] can in fact stretch a blob so much that its smaller dimension becomes comparable to the gyro-radius, offering a path for current closure (due to increased collisionality) and effectively disconnecting the blob. Another possible disconnection cause has been identified in the poloidal shearing of the $\mathbf{E} \times \mathbf{B}$ velocity [47].

Another technique, exploited in [48], is to compare the fields of view of two Gas-Puff Imaging diagnostics (see Sec.3.2) located at midplane and close to the X-point to see if locations connected by field-line tracing would provide comparable signals when a blob is detected. Findings in [48] show that in the vicinity of the X-point, two kinds of blobs can be immediately distinguished on the basis of their aspect ratio (i.e. the ratio of the maximum extension of the blob to its extension in the direction perpendicular to the first one, once the half-maximum contour has been identified). Filaments with high aspect ratio (ranging from 3 to 8) resulted to be connected upstream to the midplane and their highly elongated shape could be explained by means of the strong flux expansion present close to the X-point. Blobs with lower aspect ratio were not found to be connected and are hence called *divertor localized*. As we move from the X-point to the divertor target, divertor localized blobs become the dominant type of turbulence.

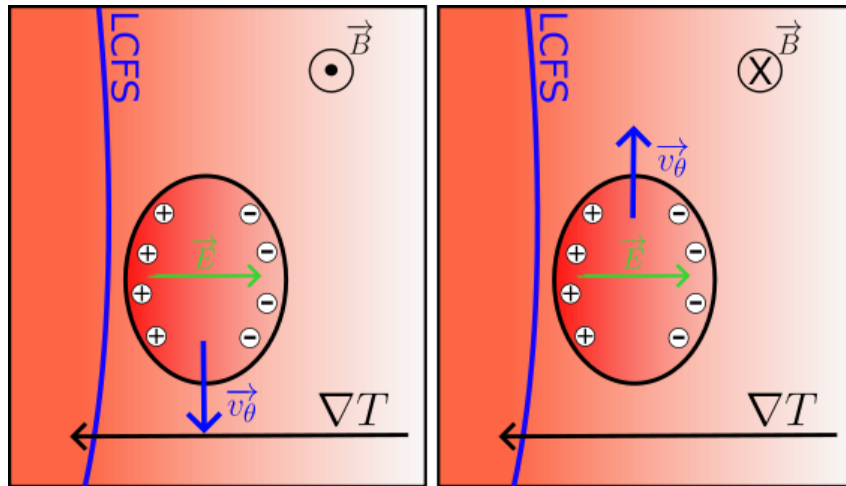


Figure 2.8: Possible mechanism explaining a blob poloidal velocity. On the left, the toroidal field is directed out-of-page, resulting in a downwards \mathbf{v}_θ . On the right, the opposite situation is depicted.

Another relevant difference among these types of blob is found in their poloidal velocity. Divertor localized blobs were seen to move poloidally upwards, in accordance with another $\mathbf{E} \times \mathbf{B}$ drift, driven in this case by a temperature gradient across the blob itself [45]. As shown in Fig.2.8 the region of the blob closer to the plasma core tends to be hotter than

the one further away. As a result, a net flow of electrons (that being much lighter than ions are more affected) to the peripheral region of the blob induces a charge separation and creates an electric field pointing outwards. This field couples once again with the toroidal magnetic field to give a poloidal velocity (whose direction depends on the orientation of the magnetic field).

On the other hand, connected blobs were found to move poloidally downwards, in the opposite direction than the one suggested by the aforementioned drift. This behaviour was still found in accordance with the same blob's movement on the midplane, but projected to the X-point by means of field-line tracing; an indication that midplane conditions somehow "set the pace" for the whole connected blob.

A better understanding of blobs behaviour is of practical importance, since there is great experimental evidence (supported by simulations) that filaments have an important influence on the overall SOL profiles and on the heat and particle cross-field transport [39–41, 49, 50]. In general, the higher density and temperature of blobs, coupled with their strong radial velocity, provides in fact an efficient cross-field convective transport, which becomes the dominant transport mechanism in the far-SOL. On this basis, in Chapter 5 is presented a heuristic model that tries to correlate the blobs phenomenology with the heat deposition on the divertor target.

Of particular interest is the change in blobs behaviour with triangularity. As δ decreases, blobs were found to appear less frequently, with a higher dimension but a lower radial velocity, lowering their contribution to particle transport [40]; for even stronger NT ($\delta \lesssim -0.25$) a complete turbulence suppression has been observed [23], the reason for which appears to be related to the greatly decreased connection length in plasmas with strong negative triangularity.

These results - consistent with the improved confinement and the lower λ_q observed in NT plasmas and simulations [38, 51] - will be further investigated in Chapter.4.

2.5. Divertor detachment

In order to preserve the integrity of the divertor, one would like to reduce as much as possible the strong fluxes it is subject to. This section summarizes (without proof) some important results in SOL modeling and how they can lead to milder *divertor regimes*. For a more detailed description, see [11].

A solid surface is an effective sink for the plasma's charged particles [11]. These tend to stick to it and when the surface charge density is high enough they start to recombine.

The resulting neutrals are not tightly bound to the wall and are soon re-emitted into the plasma due to thermal agitation. Once a steady state is reached, for what concerns particle balance the plasma is self-sustained.

In this way, the wall has a dual role. On the SOL side it acts as a pump, creating a gradient in particles density and thus ensuring a continuous flow from upstream to the target; from the balance point of view, it feeds to the plasma new neutrals that will be ionized again.

This process is known as *recycling* and can go on indefinitely, as long as we provide energy for the particles ionization.

Heat transfer through the SOL, from upstream to the target, is always a combination of convection and conduction. According to which one is predominant, two different situations arise:

- Sheath limited regime

The majority of heat is carried by convection and the SOL is almost isothermal.

- Conduction limited regime

Most of the heat flux is due to conduction and there is a strong temperature drop across the SOL.

The discriminant between the two regimes is the SOL collisionality, defined as the average number of times a particle will have a collision while travelling through the SOL:

$$\nu_{SOL} \approx 10^{-16} \frac{n_u [\text{m}^{-3}] \cdot L_{||} [\text{m}]}{T_u^2 [\text{eV}]} \quad (2.16)$$

A conduction limited regime is achieved if $\nu_{SOL} \gtrsim 15$ [11]. Eq. 2.16 shows that this happens if the upstream density is high, while the upstream temperature is low enough. A particular advantage of the conduction limited SOL over the sheath limited one is the much higher recycling it ensures [11]: the flow of recycled neutrals is in fact $\propto n_u^2$, rather than only $\propto n_u$. For this reason the conduction limited regime is also called *high recycling regime*. Its advantage is the high temperature drop along the SOL, and thus a lower target temperature T_t with the consequent reduction of the sputtering yields. Recycling also leads to some reduction in the heat flux reaching the target. The reason is that when a neutral is expelled from the wall into the plasma, before it is ionized it can go through several processes of excitation and de-excitation, during which some energy will be radiated away and thus spread on a much larger surface. As T_t gets lower, the number of excitations before ionization increases and more energy will be radiated away. This situation is known as the *strongly radiative regime*, even if there is not a sharp separation

with the high recycling one.

As T_t gets even lower, the flow of recycled neutrals starts to exercise a frictional drag (due to charge-exchange reactions) on the incoming plasma flow, thus reducing the outflow itself. The consequence is a reduced ion flux on the divertor and a loss of plasma pressure along the magnetic field [52]. Moreover, if $T_t \lesssim 1\text{eV}$, volume recombination will take place (i.e. the plasma particles do not need to reach the wall, but will recombine while still in the SOL). These effects can lead to very strong volumetric losses of energy, greatly decreasing particle and heat fluxes the divertor, as well as lowering T_t . When this happens, the divertor is said to be in a *detached regime*.

The scientific consensus today is that a power producing reactor will necessarily operate at least with a partially detached divertor, i.e. the reduction of heat flux and pressure is achieved for the first few (≈ 2) power fall-off lengths [52, 53]. At least this is the regime ITER will operate in and further study [6].

There are different ways to access a detached regime. The first and most straightforward one just consists in increasing the main plasma density: it can be shown that this has the dual effect of reducing the plasma target temperature [52] while increasing the recycling rate. Other strategies rely on increasing the fraction of the radiated power, usually by *seeding* (i.e. injecting) impurities in the divertor region. Geometrically, it should be beneficial to increase the connection length and the target major radius, even if experiments on TCV did not confirm these parameters to yield significant changes in detachment threshold [52].

Acknowledging a detached regime is not difficult, since there are at least four clear indications. Observing the particle flux to the target, in the first place it increases as the plasma density gets higher; but at the detachment onset we can observe a clear roll-over and the flux starts decreasing. In attached conditions and a high recycling regime, the Two Point Model predicts the target particle flux to grow as $\propto n_u^2$; we can thus define a *Degree of Detachment* (DoD) [54] as the ratio of the measured particle flux and the expected particle flux. Other signs of detachment include a drop in target temperature and its direct consequence: the front of emitted light due to impurities, specifically Carbon-III on the TCV tokamak (see Sec.3.6), drastically moves from the target to the vicinity of the X-point. Finally, the neutrals pressure in the divertor region increases.

A recent study performed on TCV shows the important effect that triangularity has on the access to a detached regime [55]. It was shown that detachment is more elusive for NT plasmas with respect to PT ones. The reasons for this seem to be related, at least in part, to the lower connection length; nevertheless there is evidence for other mechanisms not yet clarified.

2.6. Thesis motivation, objectives and methods

The management of the strong heat fluxes generated by a fusion plasma is a necessary step towards commercial power plants. An underestimation of these would lead to excessive erosion and damage of the first wall, and the plasma itself would suffer from the consequent high level of contamination.

The previous sections showed, among other results, the importance of triangularity on a number of very different phenomena. To briefly summarize the results, we saw how negative triangularity can increase the plasma confinement level, so that L-mode scenarios reach similar performances to H-mode counterparts (Sec.2.2). Coherently, the divertor heat flux fall-off length λ_q gets smaller as triangularity decreases (Sec.2.3) and at the same time the SOL filamentary turbulence gets suppressed (Sec.2.4). Finally, a more difficult access to divertor detachment is observed for NT plasmas (Sec.2.5).

These results have reopened the very practical question whether future tokamaks should operate in PT or NT configuration. To give a satisfactory answer, more research is needed to confirm the observed trends, to generalize them for larger parameter ranges, to understand the physical mechanisms that regulate the effects of triangularity.

To this regard, this thesis is devoted to further investigate the plasma edge in both PT and NT configurations focusing on two phenomena: divertor heat flux and SOL filamentary turbulence (Chapter 4). A possible connection between these phenomena is also proposed in the form of a heuristic blob model (Chapter 5). In the end, Chapter 6 summarizes the obtained results and concludes the work.

The work is experimental in its nature: all data that is going to be shown have been obtained from the Tokamak à Configuration Variable (TCV), located in the Swiss Plasma Center (SPC) of the École polytechnique fédérale de Lausanne (EPFL) university in Lausanne, Switzerland. A more detailed description of this facility is given in Chapter 3. Data collected by the tokamak diagnostics were then processed by MATLAB routines (some of which were specifically written for this thesis) to extract the physical quantities presented here and to investigate possible correlations among them.

In order to get acquainted with the subject, to access TCV data and to work full-time on this thesis, I spent 5 months (October 2023 to February 2024) in SPC, followed by one month in the Plasma Science and Fusion Center (PSFC) of the Massachusetts Institute of Technology (MIT) university in Boston, USA.

3 | The Tokamak à Configuration Variable

Variable

3.1. TCV and its role in this thesis

The Tokamak à Configuration Variable (TCV) [56] is a medium size tokamak located at the Swiss Plasma Center of the EPFL university in Lausanne, Switzerland.

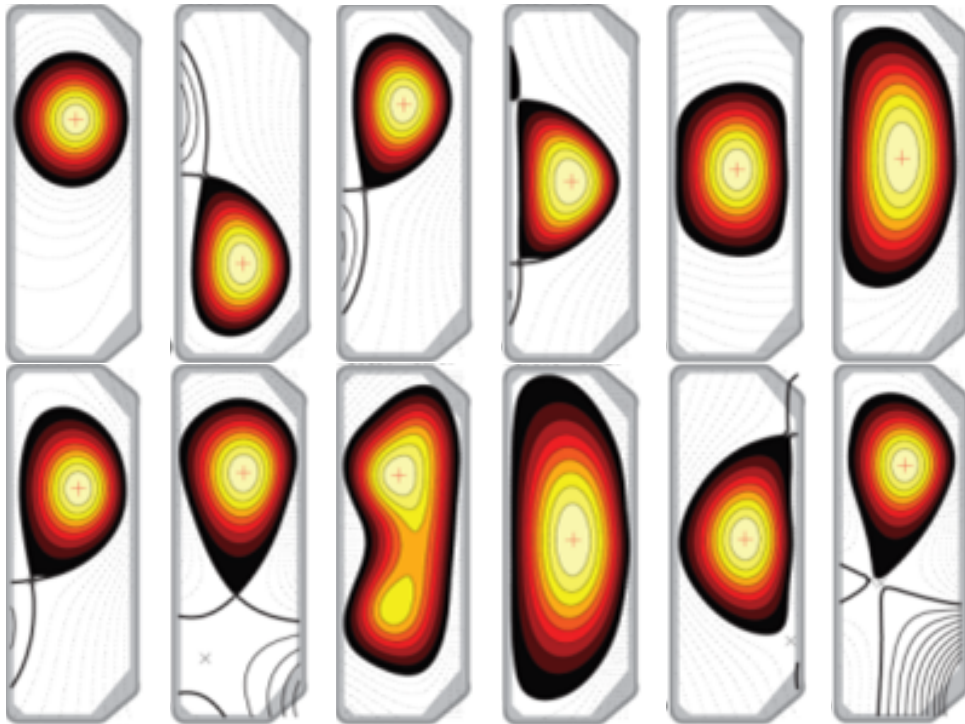


Figure 3.1: Different plasma shapes achieved in TCV. Adapted from [57].

It has a major radius of 0.88 m, and can generate a magnetic field up to 1.54 T and a plasma current up to 1 MA. The internal walls are made of graphite and there is no need for an active heat removal system, since the energy stored in each plasma shot (of the duration of about two seconds) is not enough to create damages to the vessel walls.

TCV was built in the 90s with the goal of exploring plasma performance in very different

geometries. For this reason it is equipped with 16 independently controlled plasma shaping coils, that allow to shape the plasma in a very versatile manner, as shown in Fig.3.1. While other tokamaks were built to mostly study positive triangularity plasmas and cannot rely on strong shaping capabilities, TCV's versatility has been widely exploited to push the boundary of negative triangularity studies. This reason makes it the ideal tokamak for conducting a work such as the present one.

Extracting useful data from a plasma experiment in a tokamak is not always a straightforward task: according to the particular physical quantity we want to study, a specialized diagnostic must be in place. The following sections are devoted to the description of the main TCV diagnostics used in this thesis. For each, I will briefly describe the technical instrumentation, the physical principles and the most important features.

3.2. Gas Puff Imaging

Gas Puff Imaging (GPI) [58] is a diagnostic commissioned for the detailed study of turbulent phenomena in the plasma edge. Its complexity and the considerable amount of necessary data storage make GPI a non-standard diagnostic, whose utilization must be requested and followed by a dedicated diagnostician.

Working principles

GPI relies on the light emission happening when a neutral gas (deuterium or helium) is puffed into the vacuum vessel and comes in contact with the plasma. When this happens, the neutral's electrons can get excited to higher energy levels by the plasma electrons. After a short characteristic time, neutrals decay back into the ground state while the energy difference of the two levels is converted into a photon in the visible spectrum. The exploited characteristic lines are usually $\lambda = 656\text{nm}$ for D2 and $\lambda = 587.6\text{nm}$ for He.

As shown in Fig.3.2, the GPI diagnostic on TCV is actually made up of two separate systems [59]:

- midplane GPI

The light emitted in a small field of view ($5 \times 4 \text{ cm}^2$) is reflected by two mirrors on a set of 10×12 optical fibers that transmit it to as many Avalanche Photo-diodes (APDs) that will convert the light's intensity into an amplified electrical signal. This process is necessary since the light emitted at the midplane has a quite low intensity. A great feature of this system is the very high acquisition frequency (2 MHz), high enough to track individual blobs as they move with velocities $\lesssim 5\text{km/s}$; drawbacks are the relatively poor spatial resolution and the small field of view

(Fig.3.2). In order to detect the desired wavelength, a custom made interference filter is placed between the optic fibers and the APDs.

- X-point GPI

The higher amount of light emitted in the X-point region allows the use of a commercial fast acquisition camera (Phantom v2012 FAST), having a much larger field of view ($18.2 \times 24.3 \text{ cm}^2$) and spatial resolution, but a smaller acquisition frequency (440 kHz). Also in this case an optical system of mirrors and lenses is in place to carry the light from the SOL to the camera, which must be kept quite far from the tokamak to avoid that the intense magnetic fields impacts its performances. Again, a filter is used to select the appropriate wavelength.

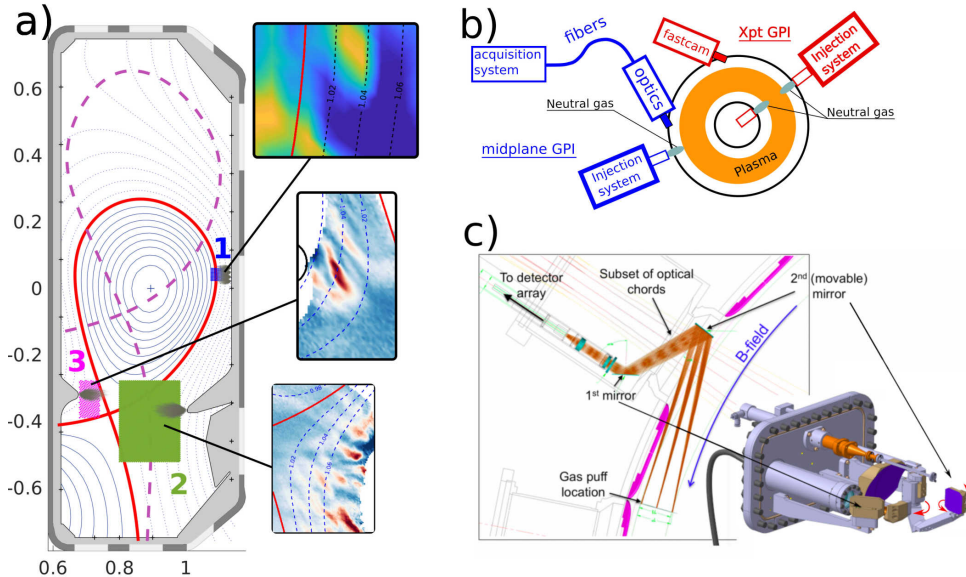


Figure 3.2: Scheme of the GPI system on TCV. a) TCV poloidal cross section showing the area covered by the GPI cameras (1:Midplane. 2:X-point Low Field Side. 3:X-point High Field Side). Two plasma geometries (red and magenta) are represented to show that different regions of the plasma can be investigated without any need of moving the diagnostic. b) Schematic view of GPI from the top, showing the position of the gas nozzles and the tangential point of view of the cameras. c) CAD model of the midplane GPI and its lines of sight, in which two mirrors are used to carry the light from the plasma into the GPI camera. Adapted from [59].

For both systems, particular care is put into the alignment of the GPI line of sight (LOS) with the magnetic field at the gas-puff location. If the alignment is bad, the resulting shapes of the blobs would be distorted from their true value. This is exactly what happens when comparing GPI results for identical plasmas with opposite helicity. In simple terms, helicity describes the twist of the magnetic field: an inversion in either the toroidal or

poloidal field would also invert the helicity and cause field lines to twist "in the opposite way". The GPI camera is placed so that its LOS is aligned with the magnetic field: if helicity is inverted the poloidal extension of the blobs can be overestimated by up to 50% and the consequent spreading of the light causes a brightness reduction up to 25% [59].

The local light emissivity ϵ of the gas cloud is related to the local plasma electrons density n_e and temperature T_e [59]:

$$\epsilon(\mathbf{r}, t) = n_0(\mathbf{r}, t) \cdot f(n_e(\mathbf{r}, t), T_e(\mathbf{r}, t)) \quad (3.1)$$

where \mathbf{r} and t are space and time coordinates, n_0 is the neutral gas density and the function f is proportional to the lifetime of the excited state and to the ratio of neutrals in the excited state to the ones in the ground state.

The brightness of light reaching the GPI optical system depends on the gas emission along the whole line of sight (Eq. 3.2a). If the LOS is perfectly tangential to the magnetic field and the gas cloud is thin enough, the integral along the LOS can be approximated as shown in Eq. 3.2b, where S_{eff} is the FWHM of the gas cloud thickness and $\epsilon|_{nozzle}$ is the value of ϵ at the toroidal coordinate of the gas injection nozzle.

$$I = \int_{LOS} \epsilon \cdot dl \quad (3.2a)$$

$$I = S_{eff} \cdot \epsilon|_{nozzle} \quad (3.2b)$$

In principle it is possible to measure more than one characteristic line simultaneously in order to estimate electron density and temperature separately; however, the brightness of some of the required lines is very low, and up to now such a possibility is not in place for the TCV GPI system.

Data analysis

Once GPI data has been collected, it must be turned into useful information. The adopted procedure is as follows.

Since the interest is usually in the fluctuations rather than in the absolute brightness, the brightness signal is normalized according to Eq.3.3, where $\bar{I}(\mathbf{r}, t)$ is the moving average over a 1ms window. This value was chosen because it is shorter than the timescale of gas density variation and much longer than the one of the fast filaments fluctuations we are interested in.

$$S(\mathbf{r}, t) = \frac{I(\mathbf{r}, t) - \bar{I}(\mathbf{r}, t)}{\bar{I}(\mathbf{r}, t)} \quad (3.3)$$

Such normalization [60] offers multiple advantages, such as making the signal S independent of the gas cloud density and revealing plasma turbulence in the outer SOL, where the absolute brightness is much lower and would otherwise be hidden.

At this point, data is processed by MATLAB algorithms with the purpose of identifying moving blobs and measuring their properties such as size, velocity, shape and appearance frequency. A blob is detected when the signal S overcomes a certain threshold, usually set around twice the average standard deviation.

The particular algorithm used in this thesis is called Conditional Average Sampling (CAS) [60] and works in the following manner. A collection of trigger points is chosen across the GPI field of view and, for each of them, every time the signal overcomes the threshold the program looks for the maximum signal in a time window of typically 60 μs and that time is recorded as a triggering event. Every trigger point will register a certain number N of triggering events and all of these are averaged according to Eq. 3.4

$$\bar{S}(\mathbf{r}, \tau) = \frac{1}{N} \sum_{j=1}^N S(\mathbf{r}, t_j + \tau) \quad (3.4)$$

Rather than analyzing every single blob, CAS retrieves the average properties of blobs passing in the location of the trigger point over a quite long time window ($\approx 10\text{-}50$ ms). To get good statistical significance, data from a trigger point can be discarded if the number of triggering events is too low.

In order to characterize the size and velocity of these average blobs, first a boundary is identified as the contour on which the signal overcomes the blob identification threshold. Then the centre of mass of the blob is found and following its evolution it is possible to identify the radial and poloidal velocities of the blob. However, other options exist: the identified blob boundary can be fitted with an ellipse and the velocities of the blob taken from the centre of the ellipse. Finally, the blob can also be identified as the region inside the half-maximum contour. The movement of the centre of this region can give another estimate of the blob velocity. The half-maximum contour is also used to estimate the blob size: for the poloidal size we "scan" the blob with a line parallel to the poloidal field in the blob centre of mass and we record the segment of the line contained within the half-maximum contour; the longest segment is then taken as the blob poloidal size. For the radial dimension the procedure is the same, but with the line being perpendicular to the poloidal field.

The main advantage of the CAS is the possibility of parallel computing, leading to reduced running times. A drawback is that the average filament is computed without any chance of discarding data from false positive blobs (such as the ones having a too short existence). Also, the averaging procedure smooths out the features of individual blobs.

3.3. Langmuir Probes

Langmuir Probes (LPs) constitute a simple, robust and inexpensive diagnostic, that have been widely used in tokamaks to obtain fundamental plasma conditions. They can be embedded in the vessel walls, or mounted on reciprocating probes to investigate inner plasma regions.

Their main drawback is the notorious difficulty in data interpretation [61].

This Section introduces the basic physical principles behind LPs operation and how data is manipulated to obtain useful information on local plasma conditions.

Working principles

When a plasma is first created, the higher mobility of electrons (with respect to ions) leads them to reach the first wall, which results negatively charge. As a consequence, a narrow layer between plasma and wall is formed, known as *sheath*. The sheath is a very particular region: quasi-neutrality is lost, a potential difference between plasma and wall (the *floating potential*, V_{fl}) arises to repel electrons and accelerate ions. Once an equilibrium is reached, and without external voltage applied, the floating potential ensures that the electron and ion fluxes to the wall have the same magnitude, so that no net current is drawn; such condition is known as *ambipolar flow* [11].

However, when an external voltage is applied to the wall, a net current can flow and a careful analysis of such current allows to retrieve information about the local plasma characteristics, including the electron density and temperature n_e and T_e .

In practice, TCV LPs are graphite cylinders with a 4mm diameter, embedded into the vessel wall and offering an almost complete poloidal coverage, as shown in Fig.3.3.

Usually, they are operated in a swept-bias mode in which an applied potential V_{pr} oscillates between about -80 to 100 V as a triangular signal of typical frequency $\approx 330\text{Hz}$ [61]. This operation allows to capture the current-potential (I-V) characteristic, and to later fit it with an appropriate physical model.

Data Analysis

Measuring the I-V characteristic is not difficult; however, linking it to physical parameters requires a complicated relation, known as *Four Parameters Model* [61]:

$$I_{pr} = I_{sat} \left(1 + \alpha(V_{pr} - V_{fl}) - e^{\frac{V_{pr} - V_{fl}}{T_e}} \right) \quad (3.5)$$

where I_{sat} is the maximum possible current (obtained when $V_{pr} = -\infty$), T_e the local electron temperature and α a coefficient account for the sheath expansion caused by the applied voltage.

Then, Eq.3.5 can be fitted on LPs acquisitions to retrieve I_{sat} , α , V_{fl} and T_e . Good results are however quite complex to obtain and a first reason is that Eq.3.5 is valid only for V_{pr} lower than the plasma potential. A delicate analysis is thus needed to identify the best cut-off voltage for the fit. a more sophisticated approach would also take into account the impact of the LPs circuit resistances. For further detail on these aspects, see [61].

Once I_{sat} is known, it can be linked to the local plasma density with the relation:

$$I_{sat} = n_{e,se} e c S \quad (3.6)$$

where $n_{e,se}$ is the electron density at the sheath entrance, c is the ions sound speed and S the effective probe collection area (depending on the actual probe surface and on the magnetic field topology, it is quite difficult to precisely evaluate).

While the LPs sampling rate is very high (200kHz), the swept-bias mode requires a lot of data points to construct and fit the I-V characteristic, so that the plasma characteristics are sampled at a much lower frequency ($\approx 10^2$ Hz).

For the purposes of this thesis, a careful reconstruction of the heat fluxes reaching the divertor is needed. The approach used here [11, 62] accounts in particular for non-ambipolar fluxes that arise when LPs are biased to any voltage different from V_{fl} . The total heat flux is then given by the sum of three contributions (electrons, ions and charge recombination on the target):

$$q_e = 2T_e(J_{sat} + J_{net}) \quad (3.7a)$$

$$q_i = (2.5T_i + V_{sh})(1 - R_E)J_{sat} \quad (3.7b)$$

$$q_{rec} = E_{rec} J_{sat} \quad (3.7c)$$

where J_{sat} and J_{net} are the saturation and net current densities, T_i the ion temperature, $R_E = 0.1$ the ion energy reflection coefficient, $E_{rec} = 13.6\text{eV} + 2.2\text{eV}$ the recombination energy per ion plus half the molecular binding energy, V_{sh} is the potential drop taking place in the sheath, computed as:

$$V_{sh} = V_{fl} - 0.5 \ln \left[2\pi \frac{m_e}{m_i} \left(1 + \frac{T_i}{T_e} \right) \right] T_e + V_{pre-sh} \quad (3.8)$$

where $V_{fl} \approx 0$, and $V_{pre-sh} \approx 0.7T_e$ is the pre-sheath voltage drop (note that all temperatures are expressed in eV).

3.4. Far-InfraRed Interferometer: FIR

Knowing the plasma density is, without doubts, a fundamental starting point for any kind of analysis. Using an interferometer is a robust and validated way for obtaining reliable measures.

The TCV Far-Infrared Interferometer [63] consists of an infrared laser ($\lambda = 184.3\mu\text{m}$) that is split in a reference beam and other 14 beams vertically crossing the whole TCV vessel, passing through the plasma (see Fig.3.3). These beams will accumulate a phase delay with respect to the reference beam, due to the different refraction index caused by the plasma presence.

The reference beam is shifted in frequency with the help of a rotating grating. A detector, sampling at 20kHz, compares the reference beam with the ones that have passed through the plasma and, from the difference (beat) frequency, can reconstruct the phase delay and so the refractive index. Since the latter is directly related to the plasma electron density, the FIR diagnostic can compute the *line averaged density* $\langle n_e \rangle$.

3.5. Baratron pressure gauges

Measuring the neutrals pressure in a tokamak can be crucial for achieving a more complete knowledge of plasma physics, in particular about the influence of neutral atoms in the

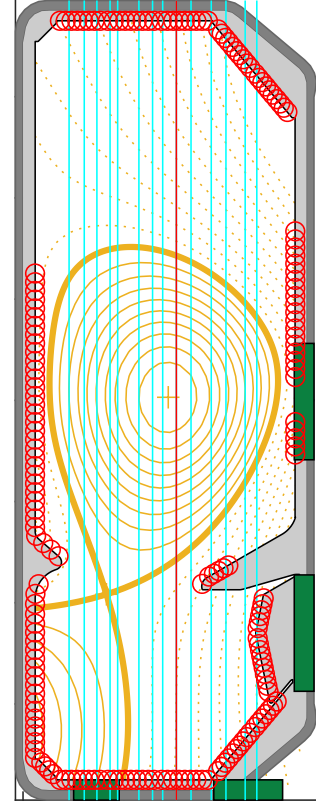


Figure 3.3: Locations in TCV of some diagnostics used in this thesis. Red circles: LPs. Green rectangles: baratron gauges ports. Vertical lines: FIR lines-of-sight (in red the reference one).

boundary. In this work, it is briefly used as an indication of approaching a detached divertor regime.

On TCV, the neutrals pressure is measured by baratron pressure gauges [63], very similar to the one already installed on JET [64]. Such gauges exploit a metal diaphragm that separates the vessel region from the baratron's backside, in which a fixed electrode is kept in very high vacuum conditions by a chemical getter pump.

A change in neutrals pressure will cause the metal diaphragm to slightly move, thus changing the capacitance between the electrode and the diaphragm itself. An electronic circuit then converts this change into pressure measurements.

The baratrons are shielded against magnetic fields and are vibrationally isolated; also, they are installed outside the toroidal field coils and are connected to the vessel via extension tubes, through ports located as shown in Fig.3.3. Since the temperature at the metal diaphragm is generally much lower than the one in the vessel, the baratron's output pressure is not the true neutrals pressure, but just reflects it. To relate the two, one can rely on the formula proposed in [65, p.144].

3.6. Multi-spectral imaging: MANTIS

MANTIS (Multi-spectral Advanced Narrow-band Tokamak Imaging System) [63, 66] is a 10-channel multi-spectral imaging system commissioned on TCV in 2018 with the dual role of passive data acquisition and sensor for real-time control.

MANTIS relies on a sophisticated optical system: light emitted from the lower portion of the plasma is collected through a port located in the vessel and impacts on the first of 10 interference filters, each of which is designed to transmit a particular wavelength with a band-pass of $\approx 1\text{nm}$. Transmitted light is captured by a camera with typical acquisition frequency of $\approx 200 - 800\text{Hz}$; reflected light reaches a concave mirror that focuses it on the next filter and so on for all 10 spectral lines (one of the channels is also exploited by the Xpt-GPI system).

Light reaches the MANTIS optical system in a tangential line-of-sight with respect to the vessel. So, naturally, the light source is spread across a certain toroidal interval. Nevertheless, we can exploit an operation known as *tomographic inversion* to compute the emission levels on a single poloidal cross-section, though this requires complex computation and cannot be run in real time.

This technique is used in this work for the Carbon-III line as an indication of a detached regime, as explained in Sec.4.1.

4 | Data analysis and results

This chapter contains a full presentation of the data that has been collected and analyzed for this thesis. A description of the choices made for the extrapolation, management and visualization of data is also given, so that any analysis can be easily reproduced. Throughout the chapter, a discussion regarding data interpretation is provided.

After Sec.4.1 will have given details on the collected data, two different phenomena will be examined here: Sec.4.2 will focus on the plasma-wall interaction in the divertor region, while Sec.4.3 will focus on a qualitative and quantitative description of the blob behaviour in the SOL. As an important reminder, the reader should keep in mind that all the shots analysed in this work were in L-mode, attached operation and all data was acquired from the low-field side SOL and divertor target.

4.1. Shots database and preliminary analysis

Parameter	Range	Notes
$ B_{tor} $ [T]	[1.4; 1.47]	Forward/Reverse
$ I_p $ [kA]	[180; 240]	+/-
$\langle n_e \rangle$ [10^{19}m^{-3}]	[2.5; 4.5]	-
R [cm]	[86; 90]	-
a [cm]	[21; 24]	-
δ [-]	[-0.3; 0.5]	-
κ [-]	[1.4; 1.75]	-
P_{tot} [kW]	[180; 380]	Ohmic(*)

Table 4.1: Parameter ranges for the TCV shots used in this thesis. (*) Input power is $\approx 90\%$ ohmic for most shots. The remaining $\approx 10\%$ comes from DNBI (Diagnostic Neutral Beam Injection), which is part of the TCV charge exchange recombination spectroscopy diagnostic.

Plasma is a very complex state of matter when it comes to its investigation and measurements are always affected by some level of error and inaccuracy. As a consequence, to reach a reasonable conclusion, one cannot rely on data from just one experiment, but, if possible, it is better to create and analyze a database collecting the highest possible number of plasma shots.

This is not a simple task, since a plasma has dozens of parameters that can vary (not always independently): if we wanted to study the effect of a single quantity (such as

triangularity), we should ensure that all the other quantities do not change too much. Following this idea, I put together a database of ≈ 100 TCV diverted shots (see App.A) sharing similar properties, some of them are summarized in Table 4.1.

As a preliminary work, the shots were analyzed to ensure that they were within the boundaries of L-mode, attached operation. This analysis was performed on 3 representative shots and, since all the collected shots share similar characteristics, the results are reasonably valid for the whole database.

The three shots chosen for this analysis are shown in Fig.4.1. Each of them is in a different geometry, as can be seen in the equilibrium reconstruction and in the triangularity table. Furthermore, they all feature an increase in plasma density around $t \approx 1$ s. Since a higher density will increase the recycling rate and can thus lead to a detached regime, these shots are very useful for our preliminary analysis.

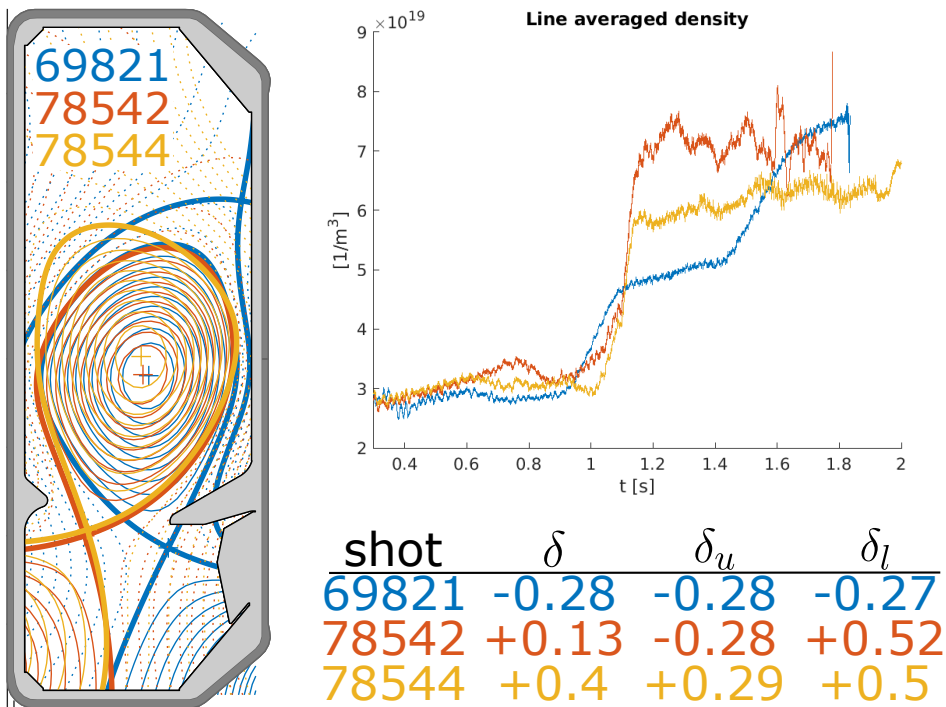


Figure 4.1: Left: equilibrium reconstruction of 3 characteristic shots (note: when shot 69821 was performed, the baffles were not installed in the machine). Right top: line averaged density during the shots. Right bottom: triangularity.

First, to ensure that the plasma shots were operating in an L-mode regime, Fig.4.2 shows D_α radiation intensity and the line averaged density (measured by the FIR interferometer, Sec.3.4) for our 3 representative shots, and one other shot (in green) that accesses an ELM-free H-mode. For the H-mode shot, we can clearly see a drop in the D_α intensity for $t \approx 1.2$ s, closely followed by an increase in line averaged density. Such a combination

identifies the L-H transition. On the other hand, the other shots can feature an increase of the D_α intensity only as a consequence of a density increase (obtained by fuel injection).

To check the attached or detached state of the divertor, we can check different quantities: the net flux of particles to the divertor target provided by the Langmuir Probes (Sec.3.3), the position of the C-III emission front provided by MANTIS (Sec.3.6) and the neutrals pressure provided by the baratron gauges, floor port (Sec.3.5).

Fig.4.3a shows the poloidal distance below the X-point of the C-III emission front (data from shot 69821 is absent since the target was not in the MANTIS field of view). We can see a clear movement of the emission front towards the X-point for $1.1 < t < 1.13$ s (explainable with the temperature dropping closer to the divertor); during the same interval the plasma density increases from $\approx 4 \cdot 10^{19}$ to $\approx 5.5 \cdot 10^{19} \text{1/m}^3$ (Fig.4.1). After this quick movement, the emission front remains quite fixed, even if the density still increases slightly further.

Checking the neutrals pressure in the divertor region (Fig.4.3b) we find, as expected, an increase for $t \gtrsim 1.2$ s: explainable with the injection of new fuel rather than a detached regime.

It is interesting to confirm the results reported in [55] regarding a more difficult access to detachment for shots with lower triangularity: the C-III front for shot 78542 ($\delta_u < 0$) clearly moves less than the front for shot 78544 ($\delta_u > 0$), even if the plasma density it achieves is higher. The same effect is reflected also for the neutrals pressure, in which the much lower pressure achieved by shot 69821 ($\delta < 0$) is evident.

These results indicate that, as the plasma density is increased, there is a shift towards a detached regime, but are still not conclusive. The clearest detachment indication is in fact the integrated particle flux to the divertor target ($2\pi \int_{target} R\Gamma dR$) and the relative

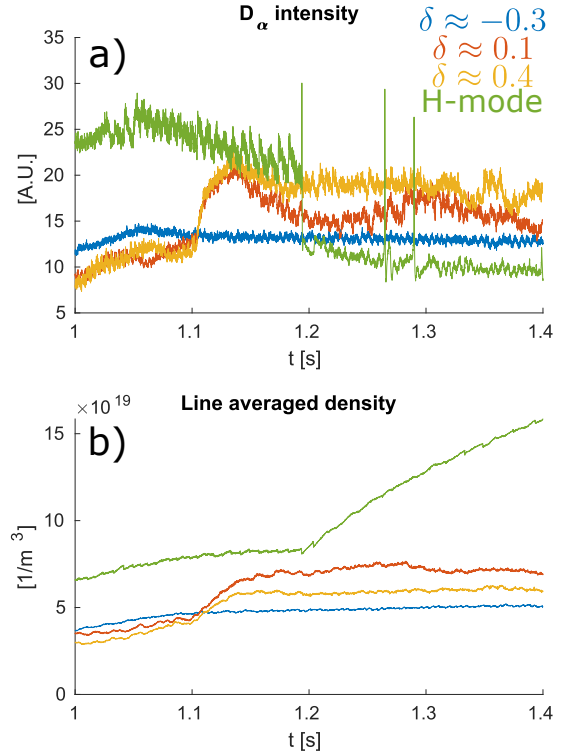


Figure 4.2: D_α radiation (a) and line averaged density (b) for checking the confinement regime.

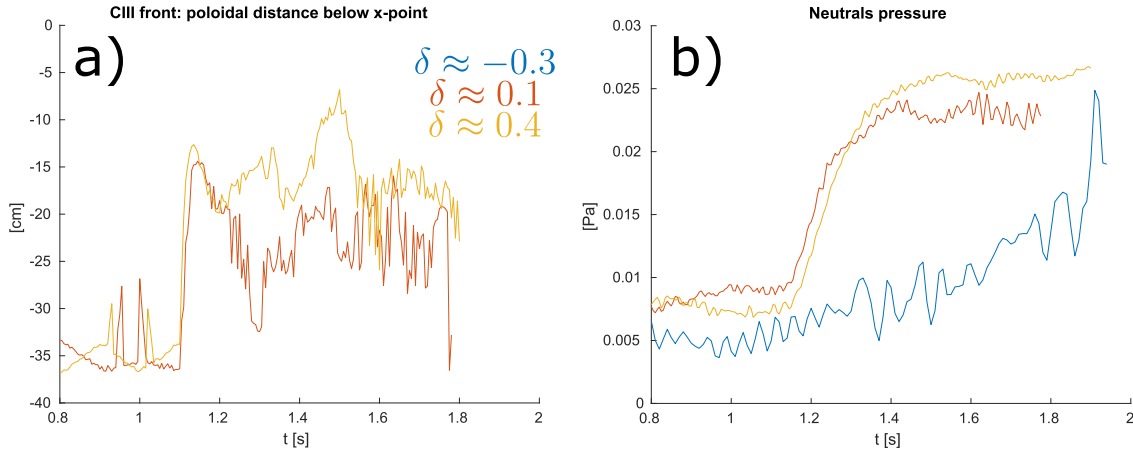


Figure 4.3: Comparison of the C-III front position (a) and the neutrals pressure (b) for shots with different triangularity. The low, symmetric peaks visible in (b) for $t \approx 1$ s can be explained by the plunges into the plasma of the RDPA diagnostic.

degree of detachment (DoD, Sec.2.5), as shown in Fig.4.4.

It is clear that the full NT shot (69821) does not show any roll-over in particle flux, while the other two shots exhibit a behaviour more similar to a saturation than to a proper roll-over for $\langle n_e \rangle > 6 \cdot 10^{19} \text{ m}^{-3}$. Once again the difficulty of detaching a negative triangularity plasma is underlined.

Shifting our attention to the degree of detachment [54], we can see it increases about 2-3 times over the shots duration, while a fully detached regime would yield higher values.

In conclusion, while it is unclear if these shots attained the onset of detachment at the highest densities, or only came close to it, without a doubt they were attached for $\langle n_e \rangle < 4.5 \cdot 10^{19} \text{ m}^{-3}$. This is the density chosen in the following as an upper limit for all the following analyses.

4.2. Heat exhaust on divertor target

In this section we are going to investigate the heat deposition profile on the low-field side target. All the profiles shown in this section have been obtained relying on wall-embedded Langmuir Probes (Sec.3.3), from which we can retrieve the plasma temperature, currents and floating potential with a 100 Hz sampling frequency and a ≈ 1 cm spatial resolution. A first, non-trivial, problem to solve is the identification of the proper time interval for data acquisition: LPs are a standard TCV diagnostic and they automatically take data throughout the whole shot, but most of it has to be discarded for various reasons, such as the plasma geometry not being the final one, the operation of a disturbing diagnostic,

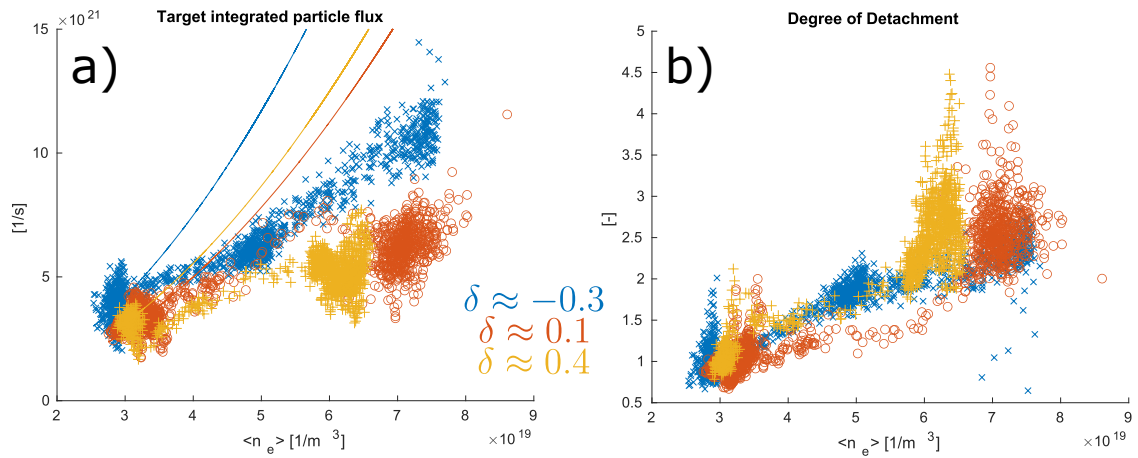


Figure 4.4: a) Particle flux integrated on the whole divertor target. Continuous lines represent a quadratic fit computed on the data at low density. b) Degree of detachment.

the shift in the plasma parameters we want to study or a disruption. Since TCV plasma shots last 2s at most and they were not specifically prepared for this work, the interplay of all these issues leads to an average useful data acquisition time of ≈ 170 ms, with some particular shots going below 50ms, thus making it hard to reconstruct a detailed profile. In fact, it is notoriously difficult to retrieve reliable and accurate data from LPs: to reduce as much as possible the uncertainty on the real profile, all the measurements acquired during the selected time window are here joined into a single profile, under the assumption of a steady-state operation.

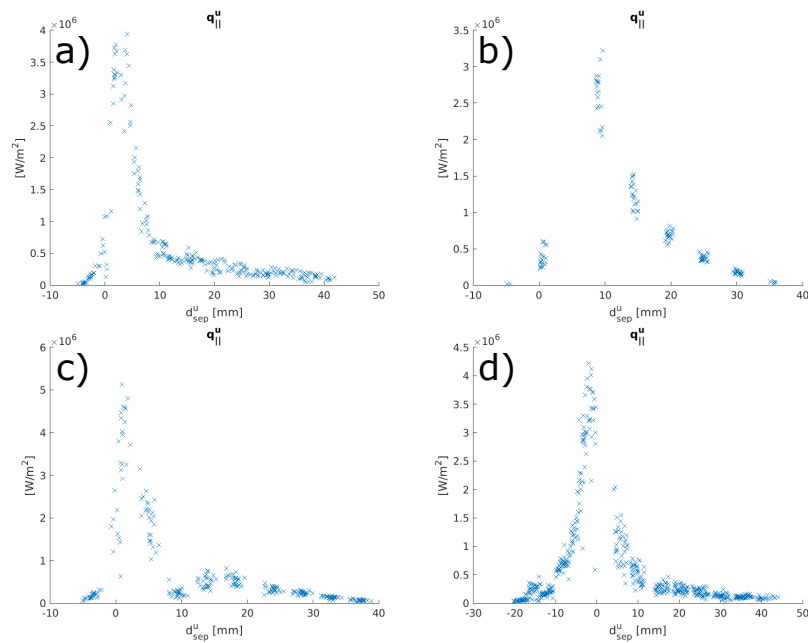


Figure 4.5: Examples of heat flux profiles acquired with LPs.

Once a suitable interval is identified, data is taken from the LPs and a detailed computation of the heat flux is performed, accounting for non-ambipolar effects such as thermoelectric currents, as derived in [11, 62]. The obtained profile is then rescaled to upstream (midplane) conditions by means of Eq.2.11. Also, since LPs can give unreliable results if the current they collect is too low, any data point featuring $J_{sat} < 1000 \text{ A/m}^2$ is discarded. Exploiting the equilibrium reconstruction code LIUQE and field-line tracing techniques we can convert each LP position directly to d_{sep}^u , i.e. the distance from the separatrix projected upstream. This also means that, if the plasma leg is swept back and forth over the divertor target during the acquisition, the limited spatial resolution given by the probes physical spacing can be overcome. Sometimes, when the heat flux profile is very narrow and "badly" positioned with respect to the probes, this is the only way to collect good data, without "missing" the peak.

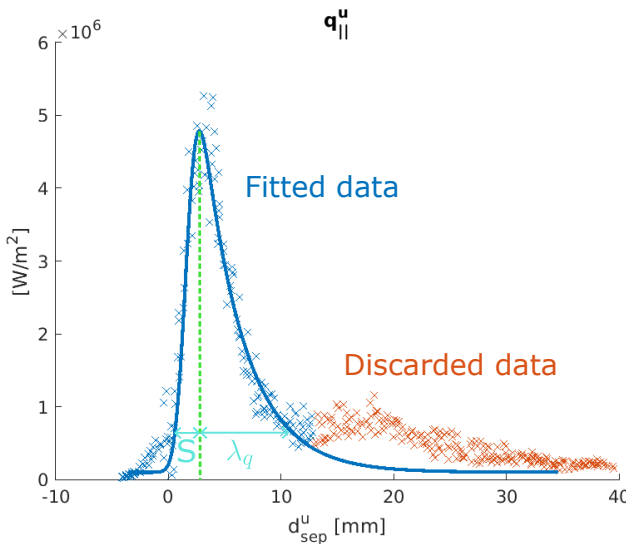


Figure 4.6: Example of Eich fit, ignoring the second peak. The physical meaning of the fitting parameters S and λ_q is also illustrated (note that the lengths drawn on the figure are indicative and do not represent the definitions of S and λ_q).

Some examples of profiles obtained with the explained procedure are shown in Fig.4.5: in panel (a) we see a "standard" profile quite similar to the Eich function presented in Sec.2.3. Nonetheless, we can already notice the presence of a slowly decaying tail on the right of the peak. Panel (b) shows a perfect example of what happens when the plasma leg is not swept at all: we can clearly see the separated contributions of the single probes, the uncertainty affecting their measurement and the impossibility of identifying the true peak. Panel (c) profile is characterized by a noticeable second peak, not explained by the Eich model. The cause of such feature has been linked to drifts effects, but a possible new explanation is offered in this thesis (see Secs.4.2.3, 5.2). Finally, panel (d) shows how some issues with the LPs can lead to a loss of information (in this case, unfortunately, close to the main peak).

To characterize the profiles of all the collected shots in a coherent manner, an Eich function

fit has been performed. Nevertheless, the presence of a long tail and/or a double peak can make this effort quite difficult. A choice was then made to give priority to the main peak fit, manually discarding the data far from the separatrix, if needed. This choice is consistent with the idea that the far-SOL is dominated by turbulence and thus described by different physics with respect to the near SOL. A fit example is shown in Fig.4.6.

Now that a consistent fitting procedure has been put together, we can identify how q_0 , λ_q , S and λ_{int} change across the database. For more reliable results, the Eich fitting parameters were included in the following analyses only if their relative error was lower than 30%.

4.2.1. Eich fitting: fall-off length and spreading factor

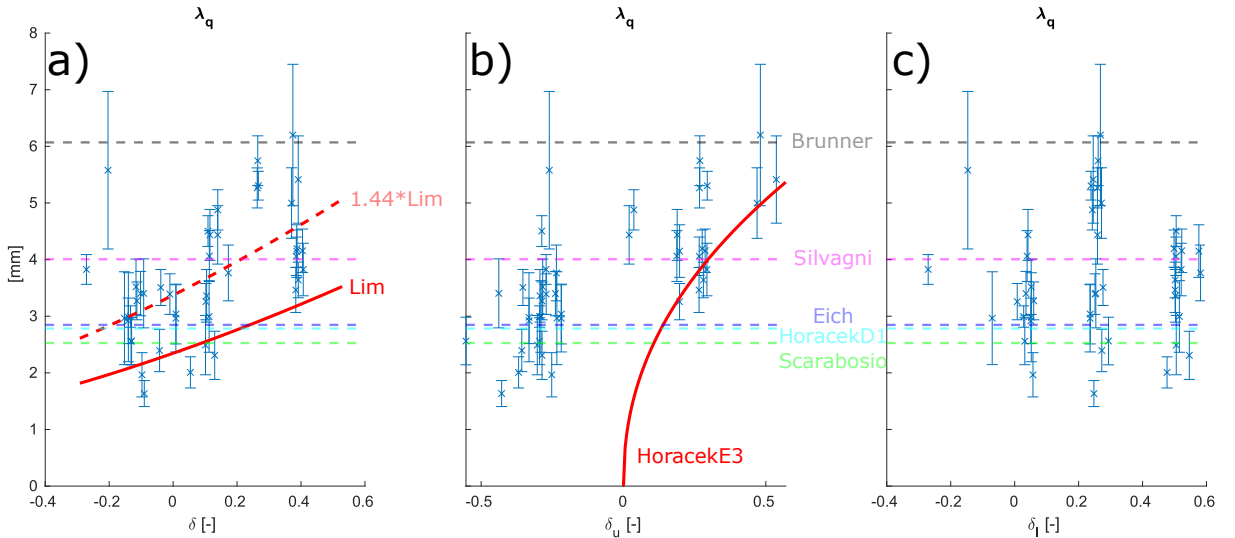


Figure 4.7: Comparison of λ_q correlations and experimental data. Dashed horizontal lines are correlations not depending on triangularity. a) Data is plotted against δ and Lim's scaling is shown. b) Data is plotted against δ_u and Horacek E3 scaling is shown.

The importance of predicting λ_q for the next generation tokamaks led to the publication of various scaling laws, some of which are reported in Table.2.1. We can now compare these correlations, especially the ones featuring triangularity as a regression parameter, with experimental data from TCV. Fig.4.7a plots λ_q against the total triangularity δ . The horizontal dashed lines represent the prediction of the δ -independent scalings, which, overall give a fairly reasonable estimate of the experimental values (each horizontal line is the average of all the predictions of the related scaling law). The red continuous line is the result of Lim's correlation. We should note that this is a theoretical scaling based on the estimation of the pressure decay length, which is then converted to λ_q via a proportionality

constant chosen to best fit the data. In Lim’s original work this constant was found to be 0.27, fitting a multi-machine database, where TCV data points were a bit underestimated. So it is consistent that the best constant found here is actually 0.39 (red dashed line).

Fig.4.7b shows the same data, but plotted against the upper triangularity δ_u and the red line now represents Horacek’s E3 scaling. It is immediately clear that this correlation was obtained with a database only featuring positive upper triangularity (in the range 0.1-0.5) and fails to represent the remaining data. Also, in Horacek’s original paper, a dependence on δ_u was not identified when fitting only low-field side data, but the inclusion of high-field side data was necessary. The present work, on the contrary, only features low-field side data and clearly shows that the upper triangularity has a role.

Finally, 4.7c shows how the lower triangularity δ_l doesn’t seem to affect λ_q at all, thus making δ_u a better regression parameter than δ in this lower single-null shots.

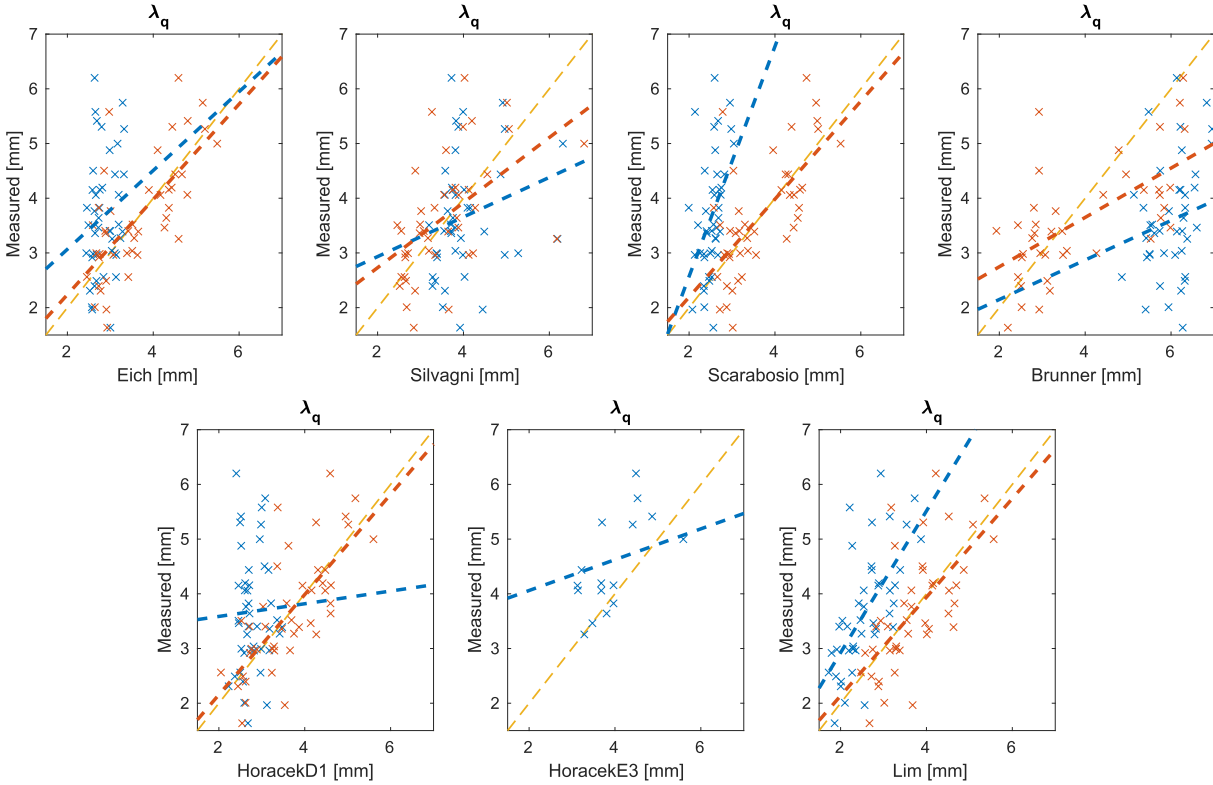


Figure 4.8: Linear regressions (dashed lines) of λ_q scaling laws (Table.2.1) and experimental data. Blue data points refer to the original correlations listed in Table.2.1. Orange data points refer to the corrected correlations. The dashed yellow line shows what a perfect fit would look like.

Since the database built for this work features minimum spreading in most of those parameters that reportedly affect λ_q , it seems pointless to come up with a new scaling law. It is however clear that a good correlation for λ_q must take triangularity into account.

Also, as shown by HoracekE3 (Fig.4.7b) this dependence cannot take the form $\propto (\delta_u)^c$, because it cannot account for $\delta_u < 0$.

	R^2	$R^2_{corrected}$
Eich	0.03	0.47
Scarabosio	0.2	0.46
Brunner	0.04	0.44
Silvagni	0.06	0.27
Horacek D1	0.001	0.53
Horacek E3	0.13	-
Lim	0.43	0.43

Table 4.2: R^2 increase after correction for various scaling laws.

improvement is impressive and is confirmed by the great increase in the coefficient of determination R^2 , shown in Table 4.2. This value quantifies the fraction of the data variability that can be explained by the regression model.

In the present database, in which the most varying parameter is the triangularity, it is unsurprising that the δ -independent correlations have such low R^2 . Still, the obtained increase after the correction is impressive, arriving close to 50%.

Of course, this result is tested only on our limited database, and there is no guarantee that these corrected correlations would perform well on a larger set of data. On the other hand, the fact that the unmodified Lim's scaling law can describe this database with the same precision of the corrected correlations (see Fig.4.8, Table.4.2) makes it a very good candidate for λ_q prediction and calls for further investigation on the role of triangularity.

These considerations led to the following "correction" of the triangularity-independent scaling laws. Each correlation was rescaled with a factor $(c_1 + \delta_u)^{c_2}$ and then fitted over experimental data to retrieve the best coefficients. HoracekE3, already dependent on δ_u was not modified; Lim's scaling was only rescaled with a proportionality constant as explained above. Fig.4.8 shows the obtained results. Blue points come from the unmodified correlations and, with the important exception of Lim, are quite distant from a perfect fit (yellow dashed line). Shown in orange is the data obtained with the corrected correlation. The description improve-

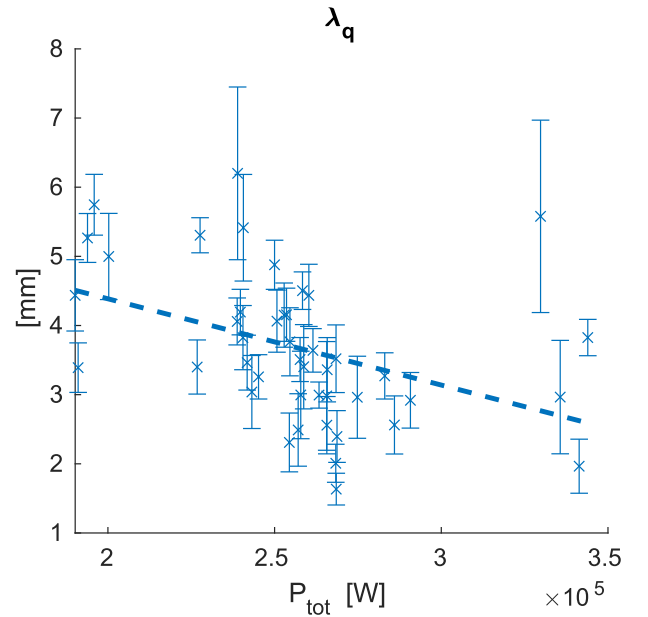


Figure 4.9: λ_q against total input power and linear regression.

Regarding λ_q , one last result worth mentioning is a negative correlation with the total power injected into the plasma (Fig.4.9).

We can now focus on the behaviour of the spreading factor. Contrary to λ_q , S is not found to be affected by triangularity and its value is spread in the interval $0.5 - 3.5$ mm (Fig.4.10a). In fact, linear regressions were performed against a high number of plasma parameters and none of them returned R^2 values higher than 0.1, indicating that S is either unaffected, or the result of a more complex interaction among them. Some weak dependencies have been found with the total input power P_{tot} and (as we would expect from Sec.2.3) the connection length $L_{||}$ (Fig.4.10b,c).

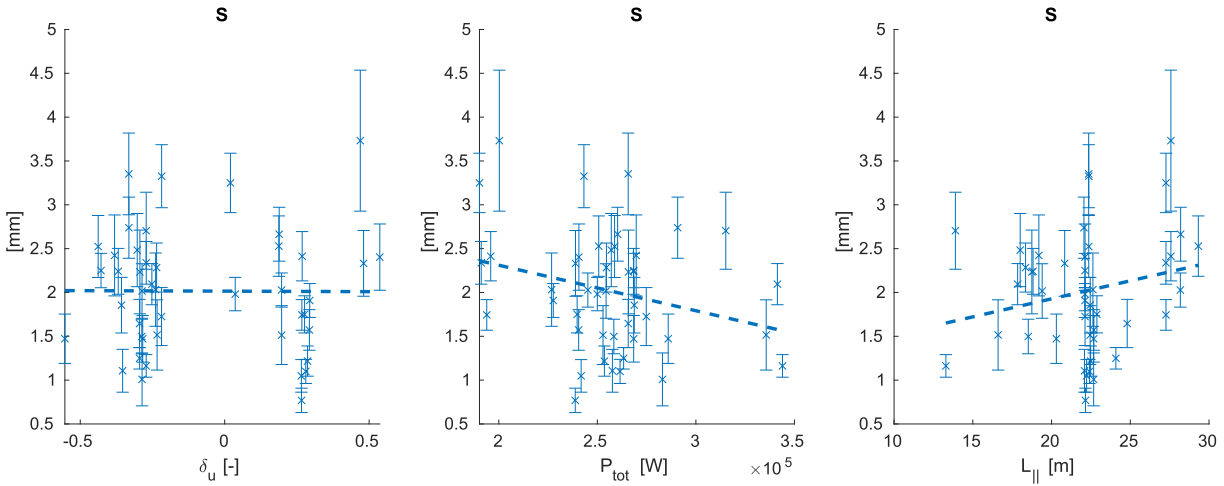


Figure 4.10: Eich spreading factor S against δ_u (a), P_{tot} (b) and $L_{||}$ (c). Dashed lines show linear regressions.

Coherently with these observations, the integral decay length (Eq.2.15) λ_{int} follows the trends seen for λ_q , primarily decreasing for lower δ_u .

4.2.2. Eich fitting: main peak and total heat flux

The determination of q_0 by means of Eich fitting is quite prone to errors. A relevant example is shown in Fig.4.11a: in the region of the peak, for a given d_{sep}^u , the data is quite spread. The reason behind this is probably a combination of uncertainties in equilibrium reconstruction and heat flux computation from LP data. The result is a fit that can still reasonably describe the data, but underestimates the true value of q_0 . Another indication in this direction comes from Fig.4.11b, where we show how the area under the Eich fit q_{int}^{Eich} (computed with Eq.4.1, with the addition of the background multiplied by Δd_{sep}^u) always underestimates $q_{int} = \int q_{||} dd_{sep}^u$ (computed with trapezoidal integration on experimental data) by $\approx 5 - 15\%$. To avoid any bias, Fig.4.11b only takes into account those shots for

which all experimental data was used in the fit, without cutting clear shoulders or second peaks. In general, an error on q_0 could also alter the values of S and λ_q , its investigation is thus of primary importance.

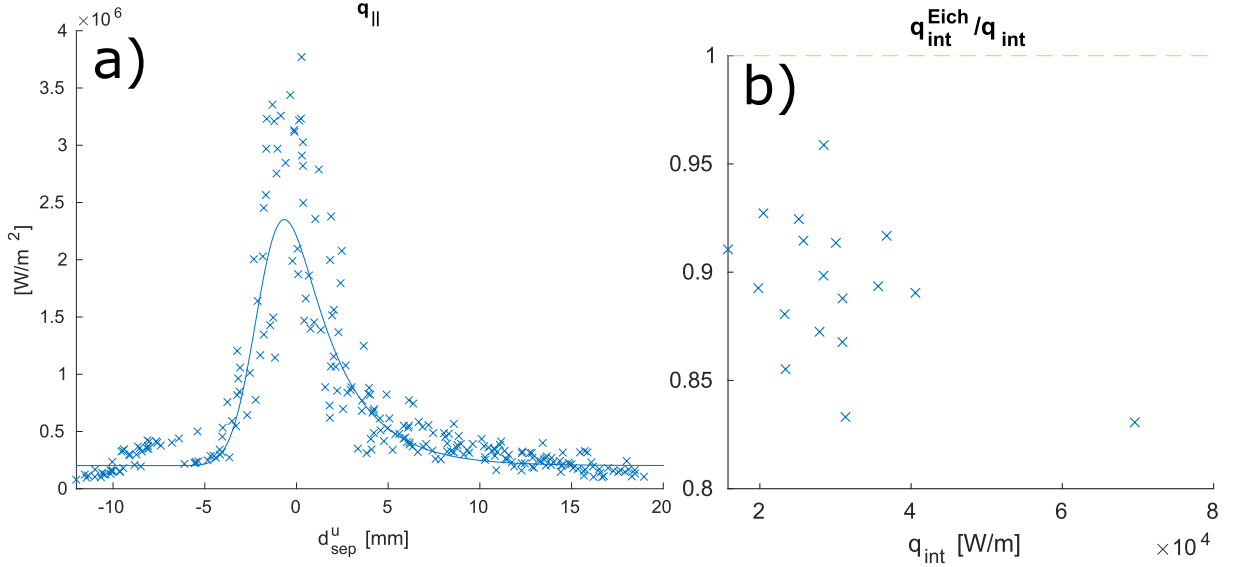


Figure 4.11: Example of an Eich fit with bad q_0 estimation. b) Comparison of experimental and fitted integral flux profiles. The yellow dashed line shows an ideal agreement

In order to make sure that this issue would not lead to wrong conclusions, the behaviour of q_0 was studied along with two other parameters: $q_{||,max}$ (mean of the 3 highest $q_{||}$ data points) and q_{int} (again, the area under the profile, computed on experimental data). Results are shown in Fig.4.12, plotted against the upper triangularity δ_u . The color code refers to the direction of the toroidal magnetic field: blue for forward field ($B_{tor} < 0$), orange for reverse field ($B_{tor} > 0$). Panels (b-c), apart from two outliers, show how triangularity does not appear to have a large effect on the height of the peak nor on the heat total flux reaching the target. The latter, however, is found to be considerably higher ($\approx 40\%$) in reverse field configuration.

Looking at q_0 in panel (a) we can still see higher values for reverse field shots, together with an unexpected spreading for the lowest triangularity, which is not limited only to the two outliers. Also, we can notice how the error bars become wider as δ_u gets lower. This phenomenology is probably a result of more than one competing mechanisms and, while some aspects remain obscure, a potential explanation is offered in the following. Bolometer data indicates that, even if all shots are fed with comparable amount of total input power (≈ 250 kW), the fraction of this power radiated by the core is considerably higher in the forward field case (64% vs 48% on average, see Fig4.13a). While the reason behind this difference is not clear, the consequence is that the power flowing into the SOL

is found to be $\approx 50\%$ higher. This observation can justify the higher values of q_0 and q_{int} in the reverse field scenario, but is not sufficient to explain the observed increase for low triangularity.

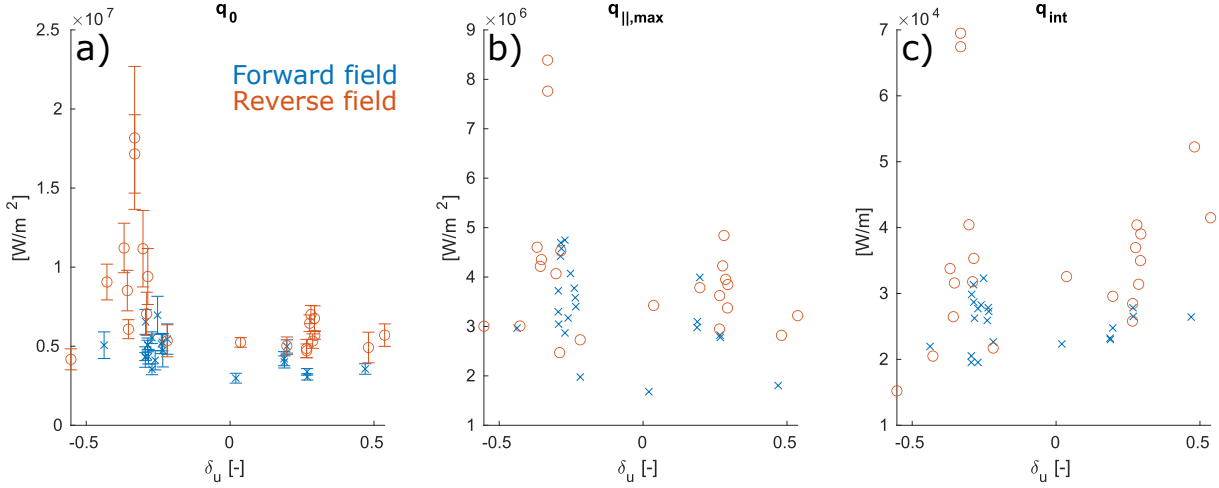


Figure 4.12: Plots of q_0 (a), maximum heat flux (b) and integrated heat flux (c) against δ_u . Blue data come from shots in forward (or negative) toroidal field, orange from shots in reverse (or positive) field.

To address this issue we can notice that, neglecting any background, the total area under the Eich function depends on both q_0 and λ_q :

$$q_{int}^{Eich} = \int_{-\infty}^{\infty} f_{Eich}(q_0, \lambda_q, S, x) dx = q_0 \lambda_q \quad (4.1)$$

Since the experimental integrated power on the target is independent of triangularity (Fig.4.12c) and we showed that λ_q decreases at lower δ_u (Fig.4.7), an increase of q_0 starts to look consistent. But why does the reverse field q_0 increase more than the forward field one (Fig.4.12)? A look at Fig.4.13b reveals that λ_q tends to be lower in the reverse field shots, especially for $\delta_u < 0$ (≈ 2.5 mm vs ≈ 3.5 mm), thus supporting this explanation.

Furthermore, to explain the widening of the error bars, we could hypothesize that the lower values of λ_q associated with lower triangularity, tend to generate a higher, but narrower, peak. This effect could be coupling with the aforementioned uncertainties in equilibrium reconstruction and heat flux computation to give an overall bad experimental profile, in which a high data fluctuation is condensed into a narrow region, thus making a precise fit more difficult.

In conclusion, to support the idea that a changing λ_q can indeed affect q_0 , Fig.4.14 shows the relative error $\frac{\Delta q_0}{q_0}$, where Δq_0 is the 95% confidence interval (i.e. ≈ 2 standard

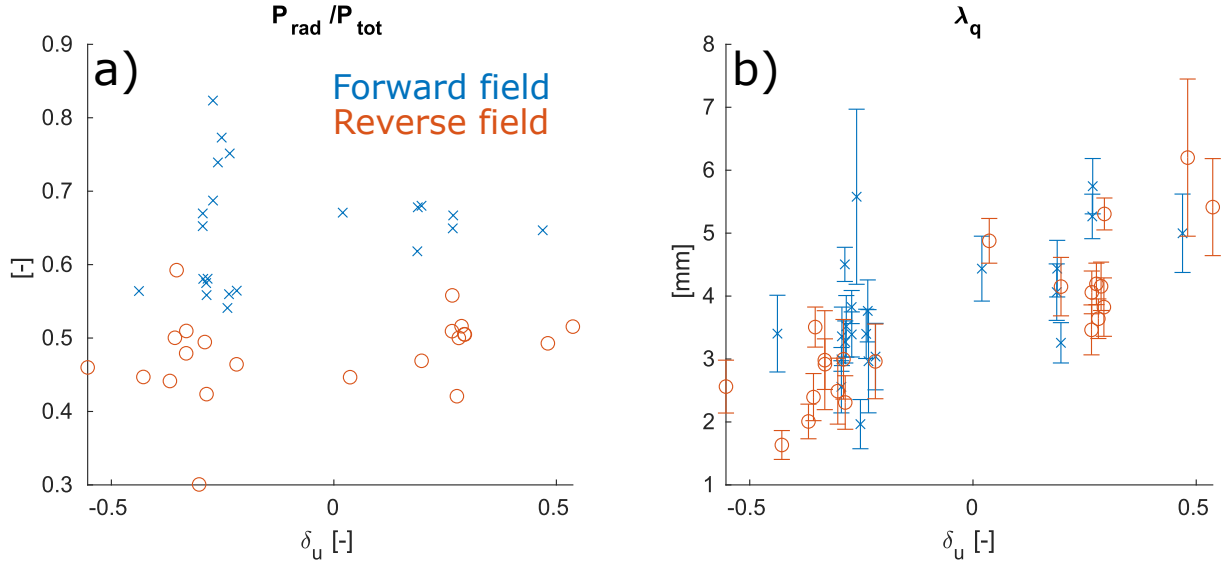


Figure 4.13: Fraction of the radiated power (a) and λ_q (b) for forward and reverse field scenarios (blue and orange).

deviations) given by the Matlab fitting function. A roughly $\propto 1/\lambda_q$ trend is visible and the opposite fields scenarios are now perfectly superimposed.

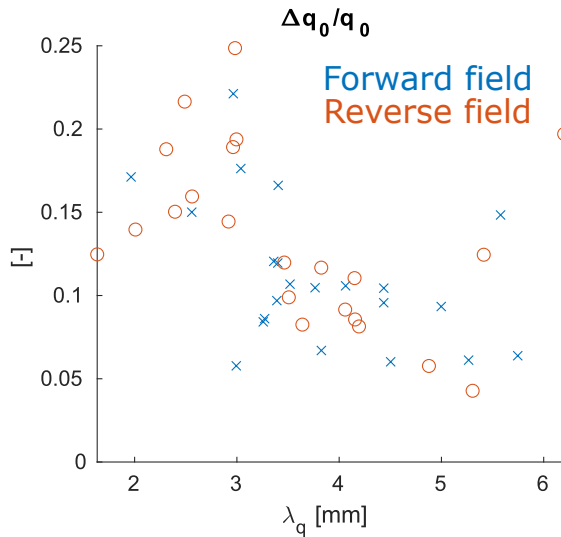


Figure 4.14: $\Delta q_0/q_0$ against λ_q .

We can now move to the analysis of a phenomenon not explainable with Eich's model.

4.2.3. Tail and second peak

As seen before, the Eich function cannot explain a frequently observed phenomenon: the presence in the target heat flux profile of a second peak, or, in a milder manner, of a slowly decaying tail (see for example Fig.4.6). To date, the insurgence and appearance of the second peak has been partially explained with a combination of $\mathbf{E} \times \mathbf{B}$ and ∇B drifts [67–69] and a more recent study on TCV [70] investigated these theories with some suc-

cess. However, a full understanding has yet to be obtained and it could prove quite useful, allowing to spread the heat flux on a larger surface.

In this section we investigate some features of the second peak that will be discussed

again in Sec.4.4 and Sec.5.2, where a different (and possibly contributing) mechanism for its formation is proposed: not based on drifts, but on filamentary turbulence.

The first difficulty in analyzing the second peak is its identification: rarely we can see a fully formed structure. Sometimes we observe little more than a "bump" in the tail of the Eich function and sometimes there is not any indication at all. Regardless, the following semi-consistent procedure was used to identify the position of the peak.

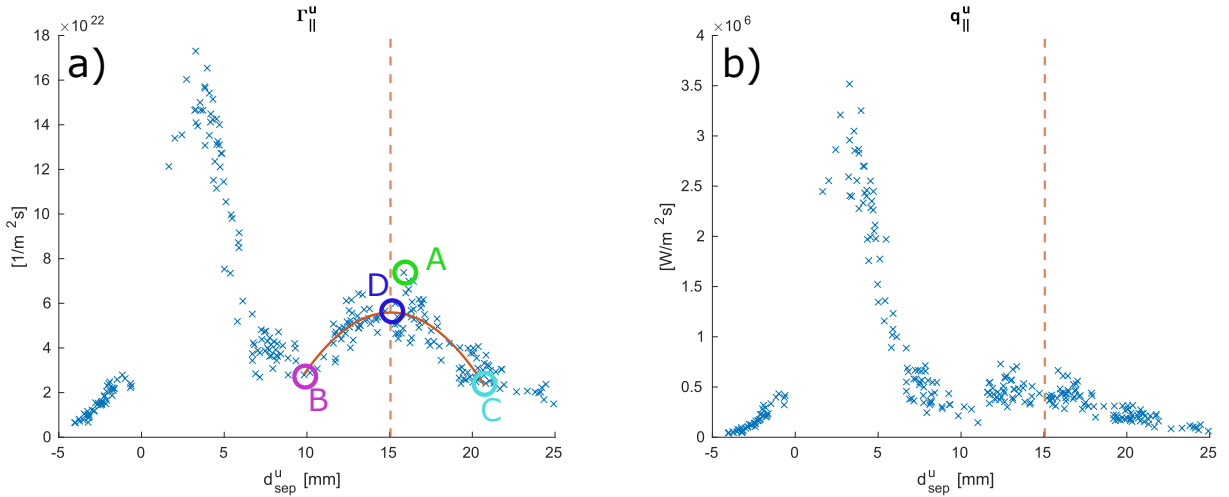


Figure 4.15: Comparison of particle (a) and heat (b) flux profiles for second peak identification. A: highest data point in the second peak. B: lowest data point between main peak and A. C: data point with closest value to B, on the right of A. The continuous orange line is a second order polynomial fit of the data between B and C. The vertex of the fit (D) is taken as the position of the peak and its radial coordinate is highlighted with a dashed line (also reported in the heat flux profile on the right).

First of all, it proved useful to discard the heat flux profile in favour of the target particle flux profile $\Gamma_{||}^t$ (Fig.4.15), in which a second peak is always easier to detect (Sec.5.2). The profile is then rescaled upstream (via the same procedure used in Sec.2.3) to obtain the upstream flux $\Gamma_{||}^u$, which is in turn scanned to find the relatively highest point (A) on the right of the main peak. One could decide to use A as the second peak's position, but due to data fluctuations this is rarely accurate. A better approach is then to find the lowest point (B) between the main peak and A. Finally point C is identified as the data point having the closest value to B, but on the other side of A. All data points between B and C are then fitted with a second order polynomial, whose vertex (D) is accepted as the second peak's position.

Despite efforts to automate this algorithm, a manual calibration was frequently needed to adjust the parameters and sometimes to force the "correct" position of the peak.

Linear regressions with a number of plasma parameters resulted in:

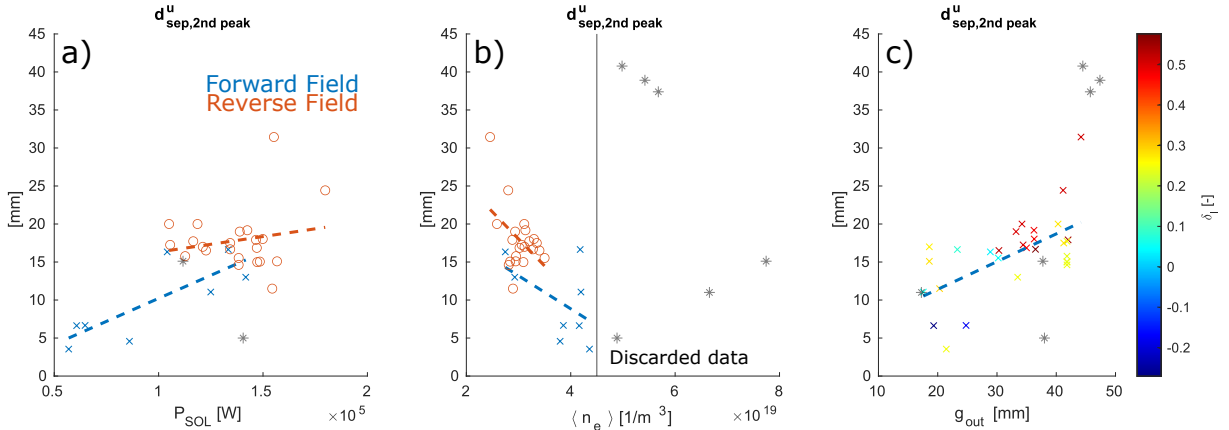


Figure 4.16: Influence of P_{SOL} (a), $\langle n_e \rangle$ (b) and g_{out} (c) on the second peak position. Blue (crosses) data is taken in forward field shots, orange (circles) in reverse field, black (stars) data was discarded due to too high density (Sec.4.1). In (c) the color bar shows how the lower triangularity δ_l roughly increases with g_{out} .

- Power and field dependency

A positive correlation with P_{SOL} is found (Fig4.16a), even if it remains unclear. The effect of field direction is also shown. A variation of the second peak position with the magnetic field direction should be expected due to the documented role of drift effects; however, more data would be needed to confirm this difference, since the overlapping of the two scenarios is limited to few data points.

- Density dependency

A remarkably clear decrease of the second peak position is observed for increasing line averaged density (Fig4.16b). At densities higher than the detachment limit of $4.5 \cdot 10^{19} m^{-3}$ identified in Sec.4.1, the trend is broken. An investigation of this dependency is left for future research, possibly taking into account the influence of a detached regime. Field direction seems to introduce an offset in the second peak position, but the little overlapping of data does not allow solid conclusions.

- Geometrical dependency

The second peak's position is seen to increase with triangularity and the width of the outer gap g_{out} (distance between the outer wall and the midplane separatrix, Fig4.16c), while also decreasing for higher major radii. These correlations are probably connected, since the creation of a negative triangularity plasma on TCV usually requires to move the magnetic axis to a higher R , thus resulting in a lower g_{out} . As hypothesized in Sec.4.4, the parameter directly affecting the second peak could be g_{out} , that would play a role in how the wall influences turbulent phenomena.

4.3. Filamentary turbulence in the SOL

In this section we are going to study filamentary turbulence in the Scrape-Off Layer (Sec.2.4) by means of the TCV Gas-Puff Imaging systems (Sec.3.2).

Two distinct GPI systems have been used: one with a rather small field of view localized at the outer midplane, and one with a much larger field of view focused around the X-point. In the following, we will refer to the first one as Omp-GPI, and to the second one as Xpt-GPI.

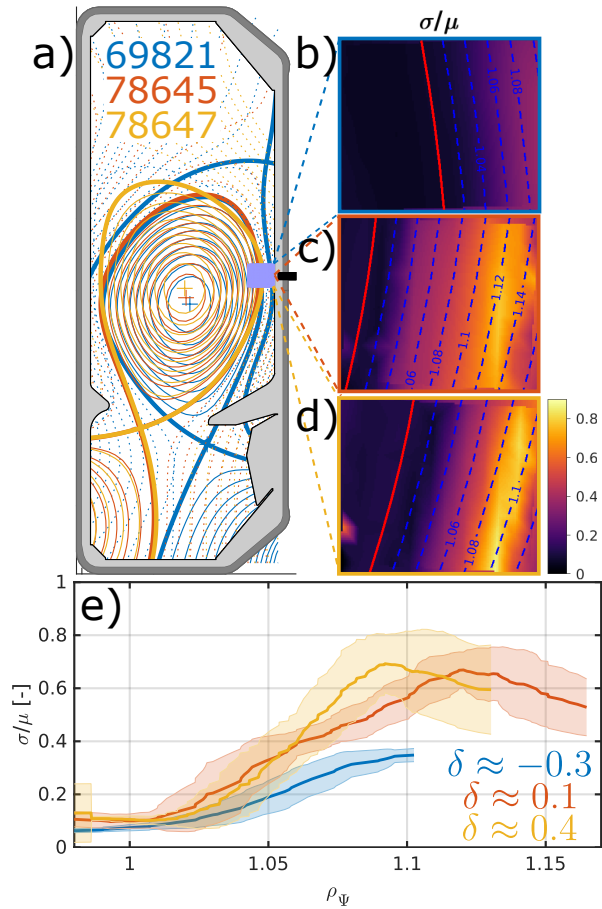


Figure 4.17: Average midplane GPI fluctuations with changing triangularity. a) Geometry of the three analyzed shots and Omp-GPI field of view (purple). b,c,d) Average fluctuations for shots 69821, 78645, 78647 respectively. LCFS is in red, increments of $\Delta\rho_\psi = 0.2$ are in dashed blue. e) Fluctuation level across the SOL.

Before diving into the analysis we should mention that GPI is not a standard diagnostic and does not run automatically, but requires a dedicated diagnostician, much more storing space for data and longer analysis times. As a consequence, GPI is only available for a few of the shots collected for this work. Nevertheless, they were enough to collect quite informative data and to highlight important differences arising with changing triangularity. At the end of the Section, data from both GPI systems will be analyzed together to "follow" the blobs evolution from midplane to the X-point.

4.3.1. Outer Midplane GPI

A first way to quickly get results from GPI is to compute the average fluctuation level in the field of view in the following way. For each pixel we take the absolute brightness recorded over the whole acquisition time and we smooth it by taking the average over a moving window of 1ms. The obtained brightness is averaged once again over the whole acquisition interval to obtain a single value μ . The procedure is repeated, but this second time, the mov-

ing window is used to compute the standard deviation of the data, which is then averaged over the whole time interval to get σ . For each pixel, the average fluctuation level is then computed as $\frac{\sigma}{\mu}$. This fluctuation should be independent on the absolute brightness, which in turn depends on the density of the puffed gas cloud, but should only depend on fluctuations in the plasma density and temperature.

This analysis (Fig.4.17) was run on three characteristic shots, whose triangularities change from full NT (69821), to a mixed $\delta_l > 0, \delta_u < 0$ (78645) to a full PT (78647); the actual triangularity values are equal to the ones in Fig.4.1.

Comparing the full NT shot (Fig.4.17b) with the other two cases (Fig.4.17c,d) we find a clear indication of that turbulence suppression described in Sec.2.4. Furthermore, Fig.4.17e - in which $\frac{\sigma}{\mu}$ has been reordered against ρ_Ψ , regardless of the poloidal position, and again smoothed with a moving window (of $\Delta\rho_\Psi \approx 0.05$) - confirms this result, while showing that a change in δ_u could shift the position of maximum fluctuation.

The next step is to actually study the blobs phenomenology. Rather than identifying and following every single blob for the whole time window, which would be highly expensive in terms of time and computational resources, we preferred to use a Conditional Average Sampling (CAS) approach, described in more detail in Sec.3.2. Briefly, a CAS analysis creates an "average" blob passing in a certain location (called trigger point) and then analyzes its appearance and movement, without actually analyzing all the individual blobs.

Fig.4.18 shows the results of a CAS analysis conducted on the mentioned shots with ≈ 45 trigger points distributed in an uniform grid in the region $\rho_\Psi > 1$ of the field of view. The analyzed time windows were respectively 50, 35 and 35 ms. As explained in Sec.3.2, velocities are taken from the motion of the blob centre of mass, while sizes are computed on the half-maximum contour.

Panels (a-c) do not show any differences in the radial properties of the blobs, although it is interesting to notice some blobs with a negative v_r (thus moving inwards, towards the plasma core). The poloidal velocity (panel b) for $\rho_\Psi > 1.05$ is the same for all shots and its direction is consistent with the mechanism explained in Sec.2.4 and Fig.2.8. The drastic inversion of v_θ happening in the full NT case in the region $1 < \rho_\Psi < 1.05$ is probably due to the strong level of $\mathbf{E} \times \mathbf{B}$ shear: close to the LCFS the radial electric field changes sign and the drift velocity follows [71]. We would expect this inversion to happen exactly around the LCFS: the shift here observed could be due to an imperfect reconstruction of the separatrix position.

The most noticeable difference is surely the discrepancy in the blob poloidal sizes, confirmed by the snapshots from the GPI videos in Fig.4.19, and not affected by issues of

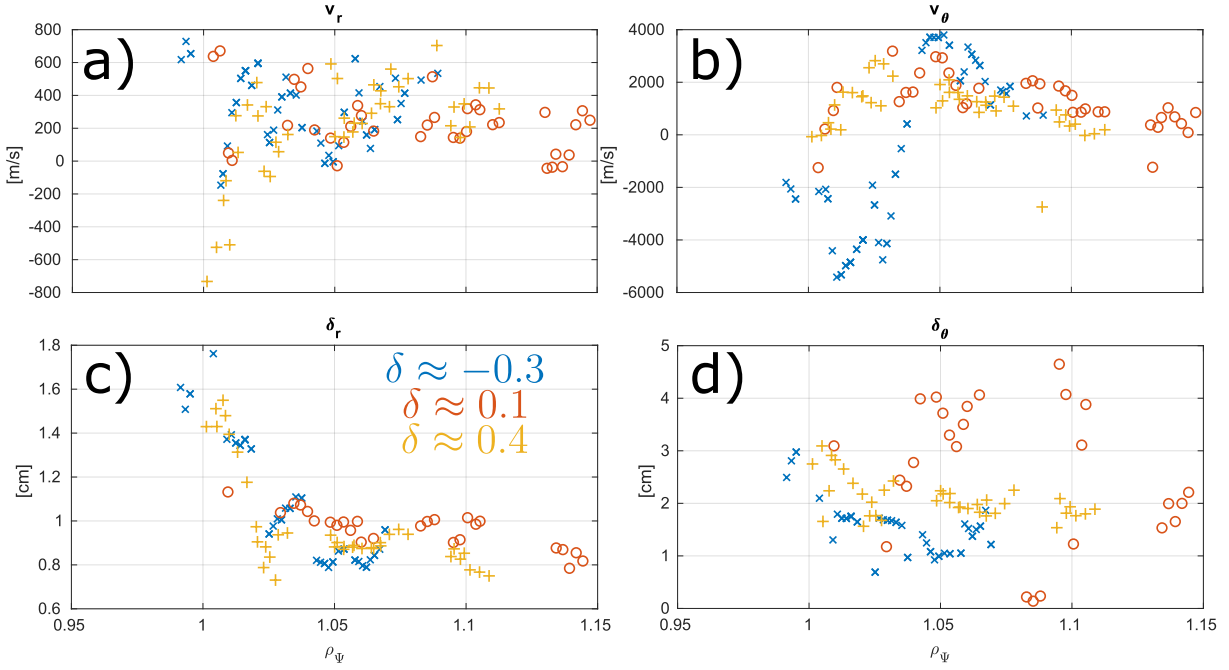


Figure 4.18: Properties of CAS analyzed blobs at the outer midplane, plotted against ρ_Ψ . a)Radial velocity. b)Poloidal velocity. c)Radial size. d)Poloidal size.

camera alignment to the field lines, since all these shots had the same helicity. A difference in poloidal size could be linked to the plasma instabilities that, close to the separatrix, lead to the formation of the blobs. While a deeper investigation is not performed here, but left for future research, we should remember that the introduction of triangularity in plasma shaping was driven by the research of better confinement properties. Therefore, it should not come as a surprise that the $\delta_l > 0$, $\delta_u < 0$ (78645) shot, whose total δ is close to zero, features blobs with the biggest dimensions; while the smallest blobs in the full NT shot are consistent with the reduced turbulence observed in similar scenarios.

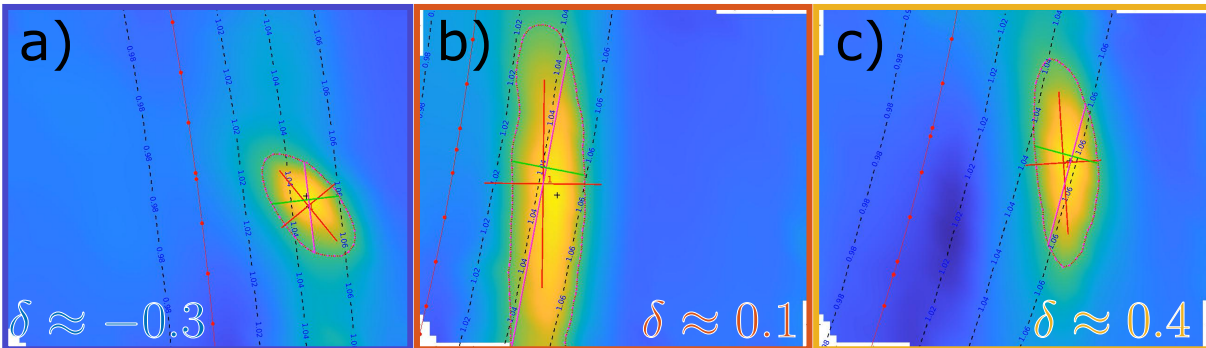


Figure 4.19: Omp-GPI CAS triggering frames for shots with changing δ at $\rho_\Psi \approx 1.05$. Half-maximum contour is dotted. Pink and green lines are poloidal and radial sizes. Red crosses are the axes of a fitted ellipse (not shown).

In general, one must be careful when reporting results about blob sizes. As shown by Fig.4.19 (particularly in panel a), the blob is not always aligned to the flux surfaces, potentially leading to an underestimation of the blob true size. This effect will be particularly strong in the X-point region, where blobs are elongated by the flux expansion and usually tilted.

4.3.2. X-point GPI

Omp-GPI was the first to be installed on TCV; the Xpt-GPI came later and we could not find any shots with full negative triangularity, also before the different position of the X-point (now moved to the low field side) makes it more difficult to study this region with the installed GPI system. The following analysis will therefore be limited to bottom PT plasmas (78545, 78647).

The same analyses of Sec.4.3.1 are repeated for the X-point region. Average fluctuations are shown in Fig.4.20. The commercial fast camera installed in the Xpt-GPI system allows for a much larger field of view. Unfortunately, however, the signal-to-noise is not strong enough in the whole window, leading to unavailable data in the far-SOL. From the remaining data we can see that the level of fluctuation is rather similar to what was found in the midplane region, with the positive triangularity case reaching $\frac{\sigma}{\mu} \approx 0.8$ closer to the LCFS (Fig.4.20d and Fig.4.17e).

Next, a CAS analysis has been performed with ≈ 90 trigger points distributed in a uniform grid in that region of the field of view in which $\rho_{\Psi} > 1$ and data was

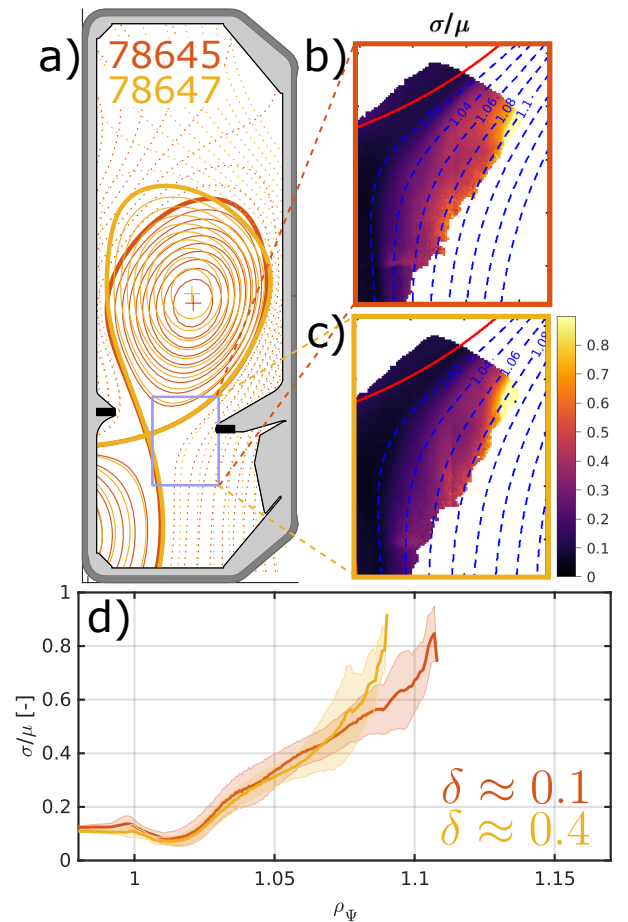


Figure 4.20: Average X-point GPI fluctuations with changing triangularity. a) Geometry of the two analyzed shots and Xpt-GPI field of view (purple). b,c) Average fluctuations for shots 78645, 78647 respectively. LCFS is in red, increments of $\Delta\rho_{\Psi} = 0.2$ are in dashed blue. d) Fluctuation level across the SOL.

present; the analyzed time windows were of 50 ms. Fig.4.21 reports the obtained results. Comparing the trends with the outer midplane analysis (Fig.4.18) we can confirm that triangularity does not seem to play any role in the blob radial size (panel c), while some difference in poloidal size δ_θ (panel d) is still detected, with the PT case (yellow) showing smaller blobs.

On the velocity side, we can now spot a very interesting trend for the radial velocity v_r (panel a). While close to the separatrix we have slower blobs (and some even moving towards the core), higher velocities are reached further in the SOL, where a peak can be distinguished before v_r starts decreasing again. We notice that the positive triangularity blobs (yellow) reach peak velocities of ≈ 1 km/s, while the mixed triangularity blobs (orange) reach more modest values, around ≈ 0.6 km/s, before slowing down.

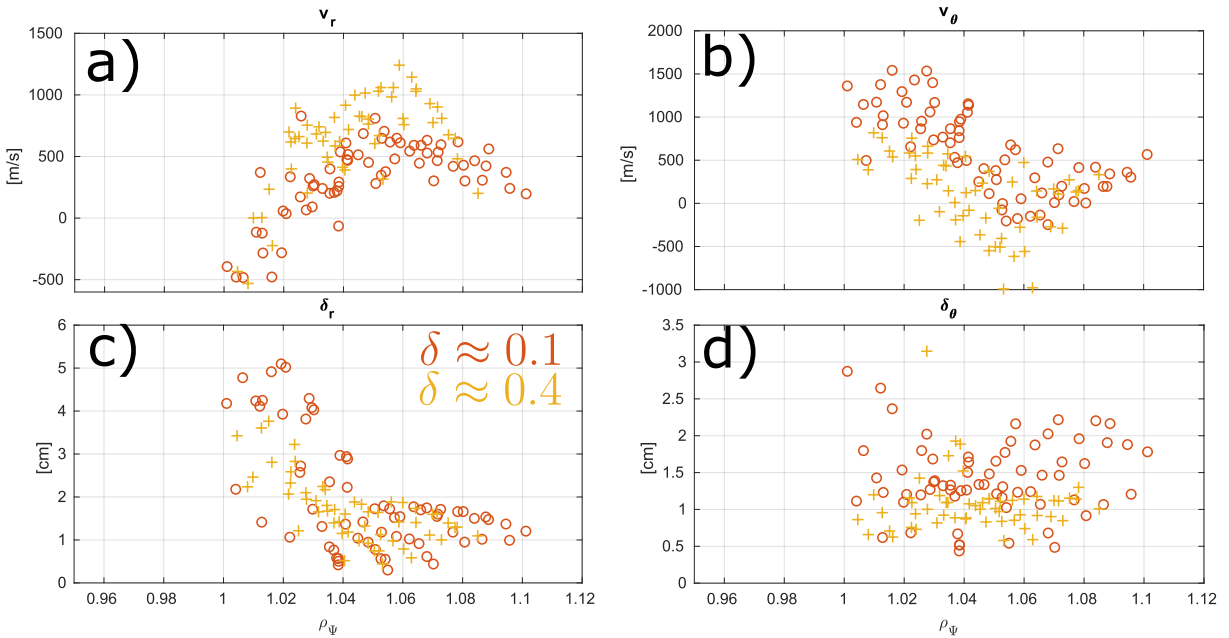


Figure 4.21: Properties of CAS analyzed blobs close to the X-point, plotted against ρ_Ψ . a)Radial velocity. b)Poloidal velocity. c)Radial size. d)Poloidal size.

On the poloidal velocity side (panel b) the PT case features smaller δ_θ . In this regard, we should keep in mind that, as explained in Sec.2.4, if filaments are connected to the midplane region, the velocities registered close to the X-point are usually dictated by the midplane ones, since the blob can be "projected" following the magnetic field lines. On the other hand, if the blobs are disconnected from the midplane, they are known as *divertor localized* and their velocities are more reflective of local plasma conditions: in particular they tend to assume less elongated shapes and their poloidal velocity is in accordance with the mechanism shown in Fig.2.8.

A previous study on TCV [48] showed that in a region very similar to the one analyzed

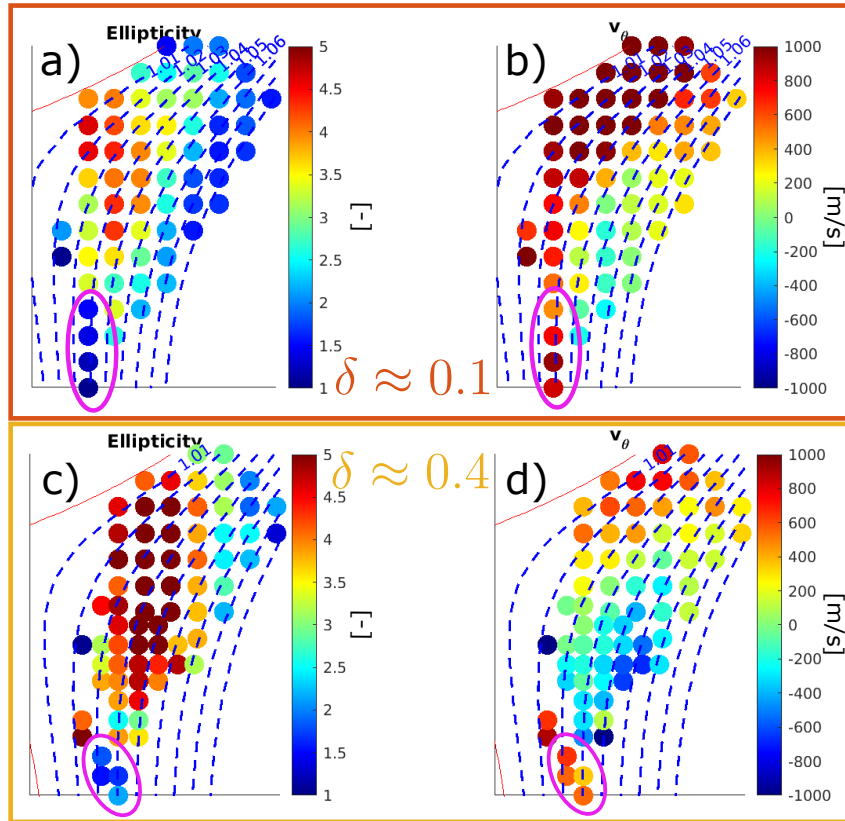


Figure 4.22: Ellipticity and poloidal velocity for X-point GPI trigger for different δ . The purple circle indicates the region where divertor localized filaments are detected.

here, most of the blobs still resulted connected to the midplane, while further down the plasma leg, the turbulence became dominated by divertor localized filaments. To check if this is still the case, Fig.4.22 shows the ellipticity (ratio of the major and minor axes of the ellipse fitted on the half-maximum contour) and the poloidal velocity for each trigger point of the CAS analysis. For both shots, there is indication of the presence of divertor localized filaments only in the lowest region of the field of view (region circled in purple), where we see a combination of low ellipticity and positive v_θ , in sharp contrast with the surrounding regions. This observation is in perfect accordance with the previous TCV results: if we could explore further down the plasma leg, we should expect an abundance of divertor localized blobs; but the majority of the field of view is dominated by connected blobs.

4.3.3. Blobs evolution from midplane to X-point

In the previous two sections, we limited our attention to a very limited number of shots and tried to highlight the main differences for a varying triangularity.

	Omp-GPI	Xpt-GPI
$\delta \approx -0.3$	1	0
$\delta \approx 0.1$	6	4
$\delta \approx 0.4$	2	1

Table 4.3: Number of GPI shots divided for triangularity and GPI location.

the flux surfaces. The obtained regions (Fig.4.23) were named "lower core" and "leg" respectively.

For each region (midplane, lower core and leg) a CAS analysis was then performed. The results regarding velocities and sizes of the detected blobs are summarized as distributions in Fig.4.24, where all histograms show to the probability $p = \frac{\# \text{ observations in bin}}{\# \text{ total observations}}$. For each distribution, a vertical dashed line indicates the average value.

In a way, these distributions are a mere confirmation of trends we already acknowledged. On the other hand, though, they let us better appreciate the differences arising with triangularity and the dashed average values give a more quantitative insight.

Following panels (a-e-i) we see how, in the X-point regions, a lower triangularity creates slower blobs (with average v_r approximately halving from $\approx 0.6\text{km/s}$ (yellow, $\delta \approx 0.4$) to $\approx 0.3\text{km/s}$ (orange, $\delta \approx 0.1$).

Panels (c-g-k) show once again the independence of radial size δ_r with triangularity, on the contrary we can see the clear effect of a strong flux expansion close to the X-point (panel g), in which the separation of the flux surfaces can strongly stretch the blobs.

In panel (j) we notice that in the leg region triangularity seems to affect the poloidal velocity v_θ , to the point that average values have opposite signs ($\pm 200 \text{ m/s}$). Such a difference could be arising due to differences in the presence of divertor localized blobs.

Now we are going to collect CAS results of some more shots, distributed as shown in Table.4.3, to see how the distributions of their features evolves as we pass from a midplane view towards the X-point. To better exploit the large Xpt-GPI field of view, its analysis was divided into two regions, delimited by a line roughly passing through the X-point and perpendicular to the flux surfaces.

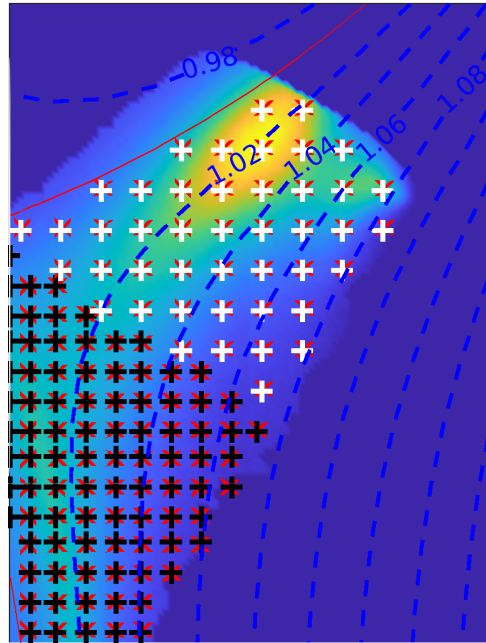


Figure 4.23: Xpt-GPI field of view separation in lower core (white trigger points) and leg (black trigger points) regions.

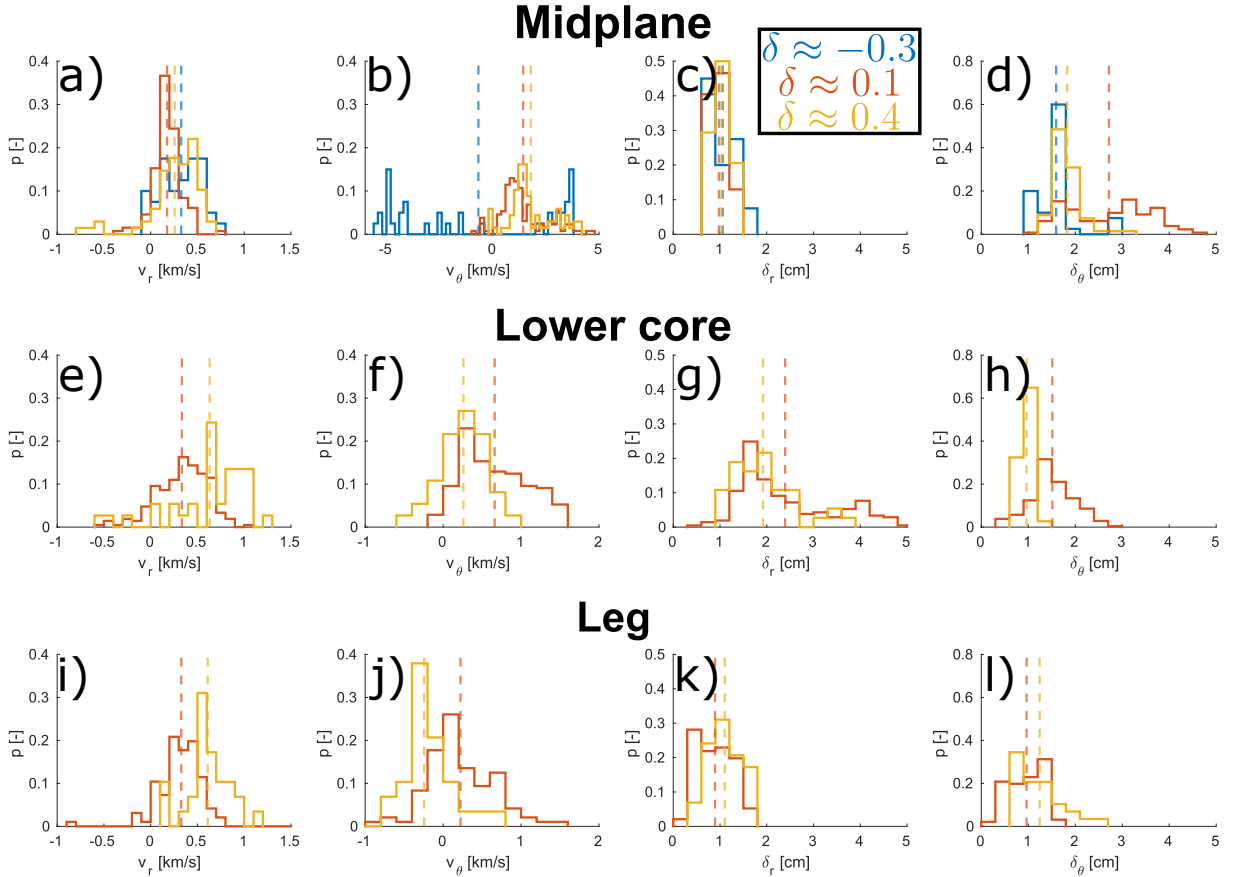


Figure 4.24: Blob velocities and sizes from midplane to X-point. Each column, from left to right, shows radial velocity v_r , poloidal velocity v_θ , radial size δ_r , poloidal size δ_θ . Vertical dashed lines show the average of the distributions.

In panel (d) we can finally appreciate the role of stronger triangularity (both positive and negative) in reducing the blob poloidal size δ_θ , even if this effect is reduced and then canceled when moving towards the X-point (panels h-l).

4.4. Summary and discussion

This sections briefly summarizes the main results and is followed by a discussion about their interpretation.

In Sec.4.2 we analyzed the Eich fitting parameters, used for describing the heat flux profile on the divertor target. The most relevant dependencies we found were on the upper triangularity δ_u , the total (ohmic) power injected into the plasma P_{tot} and the direction of the toroidal field. In particular, the power fall-off length λ_q was found to steadily decrease for a decreasing δ_u (Fig.4.7b). This result confirms previous observations on TCV [32] with many more shots and a slightly larger triangularity range. A decrease of

λ_q is also observed for an increasing P_{tot} (Fig.4.9). The spreading factor S was found to not depend on triangularity, but to still decrease with an increasing P_{tot} (Fig.4.10). The power coefficient q_0 was observed to increase for lower δ_u (Fig.4.12a), coherently with the reduction of λ_q that forces the heat exhaust to focus on a narrower region; an unexplained increase of the radiated power for forward field scenarios (Fig.4.13a) also led to lower q_0 values. Finally a positive correlation was found between the radial position of the second peak with g_{out} (width of the gap between the separatrix and the outer wall) and P_{SOL} (power entering the SOL), while a negative correlation connected it to the line averaged density, Fig.4.16. A clear role of the toroidal field direction could not be confirmed with certainty with the available data.

In Sec.4.3 we shifted our attention to the filamentary turbulence in the SOL. The shots collected for this analysis were mostly equal in terms of input power and field direction, so the only dependency we could extract was the one on triangularity, while others are left for future research. Also, a real regression was not possible, since the shots geometries varied between 3 cases, featuring $\delta \approx -0.3; 0.1; 0.4$.

In the outer midplane region we confirmed the role of negative triangularity in turbulence suppression (Fig.4.17), in accordance with a recent study on TCV [23]. The effect of strong plasma shaping (both in PT and NT) on the blob poloidal dimensions was observed in Figs.4.18d, 4.19.

Passing to the X-point region, we found the midplane results concerning blob sizes to still be valid, while a difference was detected regarding blobs velocities. In particular, v_r was found to be quite higher for higher triangularity (Figs.4.21a, 4.24e,i); at the same time, v_θ was observed to be lower (Figs.4.21b, 4.24f,j). Regarding the blobs parallel extension, evidence (Fig.4.22) showed that most of them were connected upstream, with some divertor localized blobs appearing in the lowest region of the field of view, next to the plasma leg.

Blobs are essentially portions of plasma reaching higher density and temperature with respect to the surrounding regions. Their expulsion through the SOL with very high radial velocity ($\approx 0.5 - 1\text{km/s}$) must then constitute a non negligible convective heat flux, perpendicular to the flux surfaces. We should therefore expect that some kind of connection exists between filamentary turbulence and heat flux profile. In particular, it seems reasonable to imagine a mechanism in which blobs with higher v_r can rapidly carry energy across the SOL (from the hot and dense region close to the LCFS to the colder and less dense far-SOL), thus relieving the heat deposition on the divertor's part close to the separatrix and relaxing the fall-off length λ_q . The experimental data agrees well with this description: a lower triangularity is seen to generate blobs with lower v_r and, for very

negative values, to largely suppress turbulence; at the same time λ_q steadily decreases. Figs.4.18a, 4.21a show how v_r reaches a peak value and then decreases further out in the SOL (especially clear in the Xpt-GPI data). In the picture we are building, a deceleration of the blob in the far-SOL, would create a "column" (we should not forget the blob has actually a long parallel extension) of hotter and denser plasma now moving very slowly and ultimately delivering more energy to a fixed position on the divertor. This interpretation would then help to explain the occasional insurgence of a second peak in the divertor heat flux profiles.

We should then investigate the physical mechanism causing the blobs to slow down. As recalled in Sec.2.4, v_r is a consequence of the charge separation inside the blob: the resulting electric field couples with the tokamak magnetic field to produce a drift: $\mathbf{v}_r = \frac{\mathbf{E} \times \mathbf{B}}{B^2}$. If they form, current closure paths reduce the electric field and dampen v_r . In the midplane region, the gap g_{out} between the separatrix and the outer wall is usually quite small ($\approx 2 - 5\text{cm}$); blobs themselves have a non negligible radial dimension ($\approx 1\text{cm}$ at midplane). When a blob travels through the SOL its outer boundary will at some point meet the wall, which offers a great opportunity for current closure and v_r will start to decrease. If this mechanism is truly at play, we should then observe a positive correlation between g_{out} and the position of the second peak, which is exactly what was found (Fig.4.16c).

Starting from this interpretation, in Chapter 5 is derived a heuristic model for the filamentary turbulence, with which we can simulate the effect of the blobs features on the divertor heat flux profile.

The deeper investigation of other results, such as the dependency of the Eich fitting parameters on the total power, or the mechanisms affecting the blobs poloidal size and velocity, is delayed to future research.

5 | Heuristic Blob Model

In previous chapters we focused our attention on two different phenomena taking place in the SOL: turbulence in the form of blobs and heat deposition on the divertor's target. Since blobs are coherent structures of higher density and temperature and they are travelling fast in the radial direction, it is reasonable to expect that they have an effect on the heat flux profile on the target. In this chapter we are introducing a simple heuristic model trying to describe and quantify this connection.

5.1. Model hypotheses and derivation

The basic assumption at the heart of the model is that the heat and particle fluxes to the target are the result of two contributions. The first one is the unperturbed SOL, that is the ideal case in which no blobs are generated and the whole system is in a perfect steady-state. The second one describes the presence of filamentary turbulence. Since this is an intermittent phenomenon, the approach is to compute the heat flux provided by a single blob and to later perform a weighted average of the unperturbed SOL and the blob contribution (as was done in [39]):

$$\Gamma_{\parallel} = \Gamma_{\parallel}^0 \cdot (1 - P) + \Gamma_{\parallel}^{blobs} \cdot P \quad (5.1a)$$

$$q_{\parallel} = q_{\parallel}^0 \cdot (1 - P) + q_{\parallel}^{blobs} \cdot P \quad (5.1b)$$

The P appearing in Eqs.5.1 is known as *packing fraction* and represents the fraction of the total time in which a particular position on the target is covered by a blob.

Here we are assuming that all blobs are identical and perfectly circular, having constant diameter δ_r , constant radial velocity v_r and are generated with a constant appearance frequency f . In this case, we can compute $P = f \frac{\delta_r}{v_r}$.

However, if the velocity of the blobs is not constant, but changes as a function of the distance from the separatrix $v_r = v_r(r)$, the computation of the packing fraction becomes more complex.

Referring to Fig.5.1b, for a particular location \bar{r} we have $P(\bar{r}) = f \cdot (t_A - t_B)$, where t_X is the amount of time it takes for the point X on the blob to travel from its initial position to \bar{r} . Every point of the blob moves with the same speed, given by $v_r(r)$, where r is the position of the blob center of mass. Naming r_0 the starting position of the blob, it can be shown:

$$P(\bar{r}) = \begin{cases} 0 & \text{if } \bar{r} < r_0 - \frac{\delta_r}{2} \\ f \int_{r_0 - \frac{\delta_r}{2}}^{\bar{r}} \frac{dr}{v(r + \frac{\delta_r}{2})} & \text{if } r_0 - \frac{\delta_r}{2} < \bar{r} < r_0 + \frac{\delta_r}{2} \\ f \left(\int_{r_0 - \frac{\delta_r}{2}}^{\bar{r}} \frac{dr}{v(r + \frac{\delta_r}{2})} - \int_{r_0 + \frac{\delta_r}{2}}^{\bar{r}} \frac{dr}{v(r - \frac{\delta_r}{2})} \right) & \text{if } \bar{r} > r_0 + \frac{\delta_r}{2} \end{cases} \quad (5.2)$$

For the third case, when v_r is constant, we retrieve the previous simple result. In the following we will assume that all blobs are generated with their center of mass exactly positioned on the separatrix, which means $r_0 = 0$.

We can now turn our attention to the SOL and blobs contributions. Following the derivation presented in [11], we obtain a system of equations known as the *two-point model*:

$$q_{||} = \gamma n_t T_t k c_t \quad (5.3a)$$

$$2n_t T_t = n_u T_u \quad (5.3b)$$

$$T_u^{7/2} = T_t^{7/2} + \frac{7}{2} \frac{q_{||} L_{||}}{\kappa_{0e}} \quad (5.3c)$$

Eq.5.3a is a simple expression for the heat flux delivered to the target, where $\gamma \approx 7$ is the *sheath heat transmission coefficient* and $c_t = \sqrt{\frac{2kT_t}{m_i}}$ is the *plasma sound speed*. The hypotheses used in its derivation include quasi-neutrality ($n_e \approx n_i$), ion-electron thermal coupling ($T_e \approx T_i$), electron Maxwellian distribution at the sheath edge and the *Bohm condition* (i.e. ions are accelerated up to their thermal speed in the sheath). The subscript t refers to the plasma conditions at the divertor target.

The remaining equations represent the simplest relation between target and upstream conditions. Eq.5.3b assumes pressure conservation along the whole flux tube, a condition that holds true as long as the SOL plasma is attached. Eq.5.3c comes from a power balance equation of a flux tube in which all power enters at an upstream distance $L_{||}$, conduction is the main heat transfer mechanism ($\kappa_{0e} \approx 2000 [\frac{W}{m \cdot eV^{7/2}}] \approx 1.19 \cdot 10^{-11} [\frac{W}{m \cdot K^{7/2}}]$ being the *electron parallel conductivity coefficient*) and no volumetric power sources or sinks are present. A derivation of both equations can be found in [11].

In the following, n and T without any subscript will always refer to target conditions. If upstream conditions are needed, u will be specified.

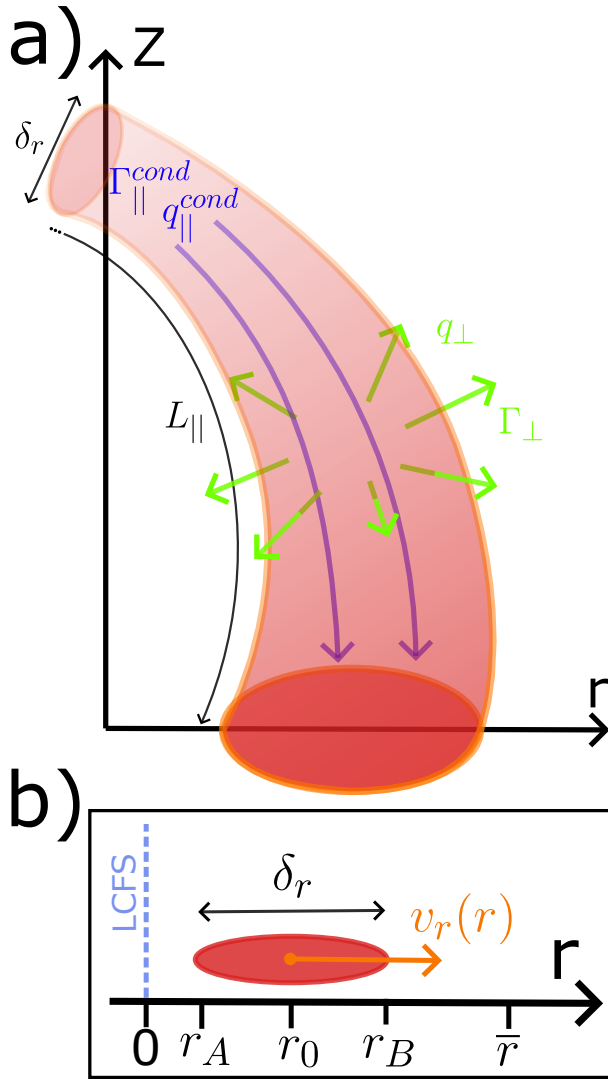


Figure 5.1: Filament description for the heuristic model. a) Blob geometry, with particle and heat fluxes. b) Blob movement across the divertor.

As a first approximation, we can consider that the unperturbed SOL has exponential profiles for n and T ($n(r) = n_{sep}e^{-r/\lambda_n}$). All we have to do is then input in the model n_{sep} , T_{sep} , λ_n , λ_T (values of n and T at the separatrix on the target and their respective fall-off lengths). Then $q_{||}^0$ can be computed using Eq.5.3a. To make the model more realistic we can consider diffusion into the private region, convolving the exponential $q_{||}^0$ with a Gaussian function of width S , thus obtaining an Eich profile, as explained in Sec.2.3. In this case, we can easily reconstruct the density and temperature profiles so they satisfy Eq.5.3a if we assume $\frac{n(r)}{T(r)} = \frac{n_{sep}}{T_{sep}} \forall r$.

In this model, filaments are always connected from midplane to the target and they have a constant cross section $A = \pi \frac{\delta_r^2}{4}$ along the connection length $L_{||}$. All blobs are generated with their center of mass on the separatrix ($r = 0$) with density and temperature defined in the following way:

$$\frac{T^{blobs}}{T^0}|_{sep} = h \frac{n^{blobs}}{n^0}|_{sep} = hR \quad (5.4)$$

Here, R defines the density fluctuations associated with a blob and h is a constant accounting for the fact that temperature fluctuations are usually weaker. The choice made here is $R \approx 1.6$ and $h \approx 0.7$, inferred from data presented in [39]. Note how, to ensure that the blob temperature doesn't drop below the unperturbed SOL temperature, the criterion $Rh > 1$ should be met.

In this model n and T inside the blob are considered to be uniform and therefore defined only in the blob center, while the heat flux that the blob generates will be spread in a Gaussian way as explained below.

Each blob is considered to give two contributions to the heat and particle fluxes reaching the target: *conductive* fluxes describe direct contact between blob and target, while *diffusive* fluxes describe the energy and particles that the blob loses through its lateral surface (these are "given back" to the SOL and will eventually reach the target, yet spread over a larger surface):

$$\Gamma_{\parallel}^{blobs} = \Gamma_{\parallel}^{cond} + \Gamma_{\parallel}^{diff} \quad (5.5a)$$

$$q_{\parallel}^{blobs} = q_{\parallel}^{cond} + q_{\parallel}^{diff} \quad (5.5b)$$

It should be noted that the term *conduction* is used here in a somewhat naive manner. In a conduction limited regime, the upstream SOL is in fact dominated by parallel heat conduction and there is almost no net flow of particles. However, things change in the few millimeters close to the target: just in front of the sheath entrance there is an acceleration of the ions to their sound speed and in the sheath a repulsion of the low-energy electrons takes place. This results in a net flow of particles to the target and the word *conduction* becomes less accurate.

In order to compute the time evolution of the blob parameters, we exploit a particle and energy balance approach and a finite difference scheme. We can start by defining the total particles (Eq.5.6a) and energy (Eq.5.6b) contained in the filament, counting both electron and ions:

$$N = 2n_u AL_{\parallel} \quad (5.6a)$$

$$U = 2 \cdot \frac{3}{2} k n_u T_u AL_{\parallel} = 6k AL_{\parallel} n T \quad (5.6b)$$

The aforementioned fluxes will direct particles and energy to the target and into the SOL:

$$\Gamma_{\parallel}^{cond} = 2nc = 2\sqrt{\frac{2k}{m_i}} n T^{1/2} \quad (5.7a)$$

$$\Gamma_{\perp} = D_{\perp} \frac{\Delta n_u}{\delta_r} \quad (5.7b)$$

$$q_{\parallel}^{cond} = \gamma k \sqrt{\frac{2k}{m_i}} n T^{3/2} \quad (5.7c)$$

$$q_{\perp} = \frac{5}{2} D_{\perp} k T_u \frac{\Delta n_u}{\delta_r} + \chi_{\perp} n_u \frac{k \Delta T_u}{\delta_r} \quad (5.7d)$$

Eq.5.7c comes directly from Eq.5.3a, Eq.5.7d describes the heat flux leaving the blob through its lateral surface $A_{\perp} = \pi \delta_r L_{\parallel}$, taking into account particle diffusion (Eq.5.7b) driven by the density gradient $\Delta n_u = n_u^{blob} - n_u^0$ and heat conduction driven by the temperature gradient $\Delta T_u = T_u^{blob} - T_u^0$. D_{\perp} and χ_{\perp} are the cross-field *mass diffusivity* and *thermal diffusivity*. Balance equations then take the form:

$$N(t + dt) = N(t) - \Gamma_{\parallel}^{cond}(t) A dt - \Gamma_{\perp}(t) A_{\perp} dt \quad (5.8a)$$

$$U(t + dt) = U(t) - q_{\parallel}^{cond}(t) A dt - q_{\perp}(t) A_{\perp} dt \quad (5.8b)$$

Substituting Eqs.5.6,5.7 in Eqs.5.8 and exploiting Eq.5.3b we obtain:

$$n_u|_{t+dt} = n_u - \left(\sqrt{\frac{2k}{m_i}} \frac{1}{L_{\parallel}} n T^{1/2} + \frac{2D_{\perp}}{\delta_r^2} \Delta n_u \right) dt \Big|_t \quad (5.9a)$$

$$T_u|_{t+dt} = \frac{2nT - \left[\frac{\gamma}{3L_{\parallel}} \sqrt{\frac{2k}{m_i}} n T^{3/2} + \left(\frac{5}{2} D_{\perp} T_u \Delta n_u + \chi_{\perp} n_u \Delta T_u \right) \frac{4}{3\delta_r^2} \right] dt}{n_u - \left(\sqrt{\frac{2k}{m_i}} \frac{1}{L_{\parallel}} n T^{1/2} + \frac{2D_{\perp}}{\delta_r^2} \Delta n_u \right) dt} dt \Big|_t \quad (5.9b)$$

Where all the terms on the right-hand-sides are evaluated at time t and are therefore known.

Finally we can obtain the plasma conditions on the target by rearranging Eqs. 5.3:

$$T^{7/2} + \frac{7\gamma k L_{\parallel}}{4\kappa_{0e}} \sqrt{\frac{2k}{m_i}} n_u T_u T^{1/2} - T_u^{7/2} \Big|_{t+dt} = 0 \quad (5.10a)$$

$$n|_{t+dt} = \frac{n_u T_u}{2T} \Big|_{t+dt} \quad (5.10b)$$

where all terms are evaluated at time $t + dt$. Eq.5.10a is a 7-grade polynomial equation and must therefore be solved numerically. The result can be then substituted in Eq.5.10b. From this point it is straightforward to obtain the conductive fluxes that the blob directs on the target, exploiting Eqs.5.7a,5.7c.

What is less clear is how to obtain the diffusive contributions: how can we pass from the fluxes $\Gamma_{\perp}, q_{\perp}$ that the blob gives back to the SOL, to the fluxes that these particles and energy will cause on the target, $\Gamma_{\parallel}^{diff}, q_{\parallel}^{diff}$. The approach used here is to "redirect" the total particles and energy that the blob has diffused into the SOL into parallel fluxes to the target over the cross section of the blob:

$$\Gamma_{\perp}(t)A_{\perp}dt = \Gamma_{\parallel}^{diff}(t)Adt \quad (5.11a)$$

$$q_{\perp}(t)A_{\perp}dt = q_{\parallel}^{diff}(t)Adt \quad (5.11b)$$

Now that we have the blob fluxes to the target, rather than directing them all on the blob's central position, it is more realistic to spread them by means of a Gaussian distribution centered in the blob's central position. The standard deviation of the distribution is chosen to be $\delta_r/4$ for the conductive fluxes and $\delta_r/2$ for the diffusive ones. The total area under the distributions must be given by the fluxes multiplied by the packing fraction P . Finally, the blob's position is shifted by $dr = v_r dt$ and the computation is repeated.

5.2. Predictions and discussion

Parameter	Value
n_{sep}^0, T_{sep}^0	$\approx 10^{19} \text{m}^{-3}, \approx 40 \text{eV}$
λ_n^0, λ_T^0	$\approx 6 \text{mm}$
S^0	$\approx 2 \text{mm}$
D_{\perp}, χ_{\perp}	$\approx 0.2 \text{m}^2/\text{s}$
δ_r	$\approx 10 \text{mm}$
f	$\approx 10^3 \text{Hz}$
L_{\parallel}	$\approx 15 \text{m}$

Table 5.1: Typical parameters for heuristic model computation.

Before running the model, one must define the parameters values: a typical choice is shown in Table.5.1.

We then meet the first issue in achieving good predictions: while some parameters can be taken from experimental observations (such as the blobs dimensions, velocity and appearance frequency), others, the parameters describing the unperturbed profile are not directly measurable and all we can do is an educated guess. Furthermore the diffusion parameters D_{\perp} and χ_{\perp} are anomalous and should be measured; however, their anomaly stems also from the

same turbulent phenomena that we are trying to isolate here, so that choosing an accurate value is even more difficult.

From these considerations, it is clear that we should give more emphasis to the qualitative results we are going to get, while being cautious about quantitative conclusions.

The typical model result is shown in Fig.5.2. While keeping in mind that this is a very crude approximation of the physical reality, since all blobs have the same v_r throughout the whole SOL, we can already recover some experimentally observed phenomena: the final profile (purple) closely resembles the starting Eich profile (blue) around the main peak; however, the blobs contributions become dominant in the far-SOL and create that slowly-decaying tail we are used to see.

An interesting fact is that the blobs diffusive contributions are dominant over the conductive ones, although this largely depends on the value of the diffusion coefficients and the true parallel extension of the blob.

The first thing we want to test with the model, is if a different radial blob velocity v_r can indeed alter the Eich fitting parameters, and λ_q especially. To conduct this analysis, we must then fit an Eich function over the model's output profile. We already noticed in Sec.4.2 how, for experimental data, the Eich fit was made easier and more significant by cutting the profile tail. Now we face the same situation, except that the simpler nature of the data lets us decide the cutting point in a consistent way (here set as the location where the heat flux has dropped to 20% of its maximum value), instead of choosing it manually for every profile.

In Fig.5.3a we see the effect of blobs v_r on the fitted values of λ_q . In panels (b-c-d-e) some of the simulated profiles are shown with the relative fits. At a first glance we notice how blobs always considerably increase the value of λ_q from the unperturbed value. The latter is computed from Eq.5.3a considering exponential decays for n and T with fall-off

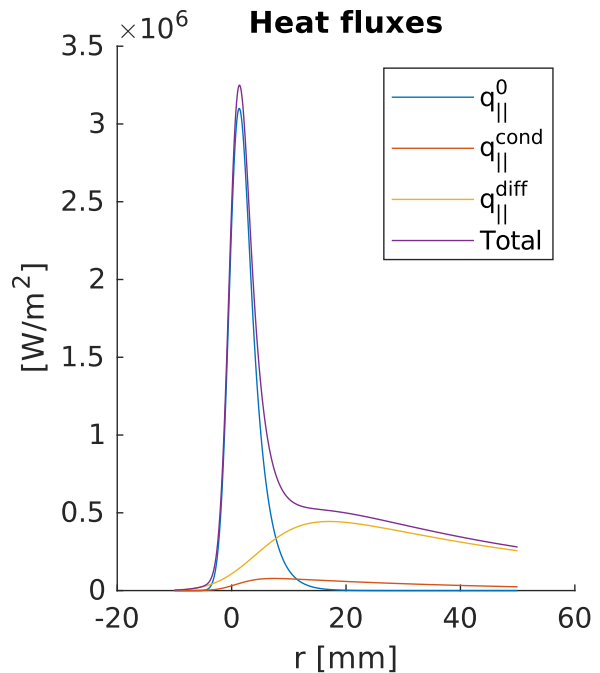


Figure 5.2: Example of heuristic blob model output. All blobs contributions have already been resized with the packing fraction and spread with gaussian curves.

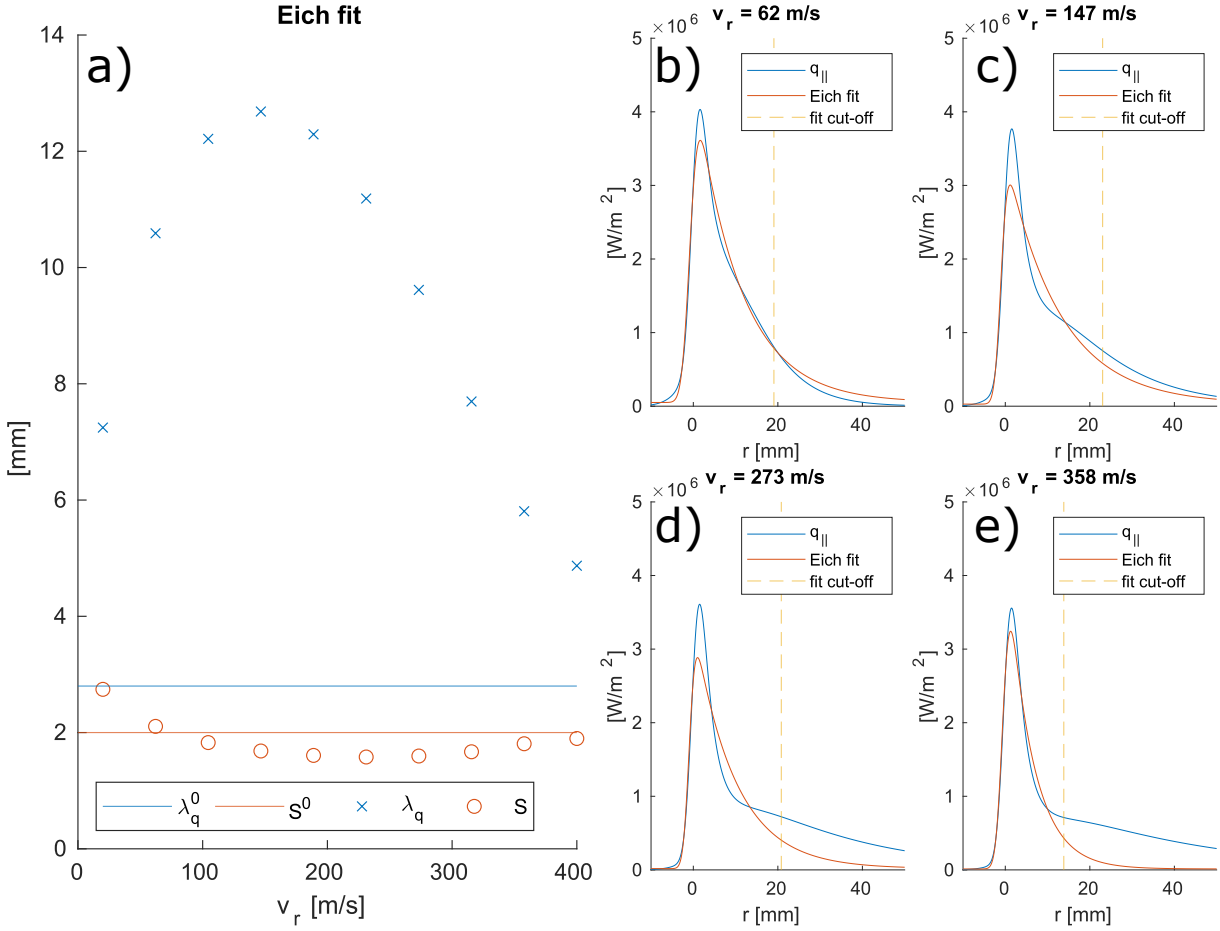


Figure 5.3: a) Simulated effect of blobs v_r on λ_q and S . Horizontal lines show the original unperturbed values. b,c,d,e) Simulated profiles for increasing blobs v_r . The fit is cut when the heat flux falls down to 20% of its maximum value.

lengths λ_n^0 and λ_T^0 : $\lambda_q^0 = \frac{2}{3} \frac{\lambda_n^0 \lambda_T^0}{\lambda_n^0 + \frac{2}{3} \lambda_T^0}$. On the other hand, the spreading factor S is not much affected.

As we expected, for increasing v_r we observe an initial increase in λ_q ; however this correlation is quickly lost and the fitted fall-off length starts decreasing for higher v_r . The reason is simple: for rate at which blobs deliver energy to the divertor is independent of their velocity, but the region of the target over they sweep is not. A slower blob will lose all its energy close to the main peak, thus affecting its shape much more than a very fast blob. The latter will in fact quickly move away from the main peak and proceed to release most of its energy into the far-SOL, creating a slowly decaying tail without affecting the main peak, and λ_q will consequently decrease. This difference is well represented in Fig.5.3b-e. The λ_q decreasing trend must be considered with caution for at least three reasons. First, the decision about where to cut the $q_{||}$ profile for the fit can deeply affect the value of v_r for which λ_q reaches its maximum, as well as the maximum itself. Second, in a real

SOL the blobs radial velocities would not be fixed to a single value, but rather sampled from a distribution, so that slower blobs would still affect the main peak. Third, it is not realistic to assume that the blobs velocity remains constant across the whole SOL.

Another similarity with experimental data can be seen in Fig.5.3c-d: the modification of the profile coming from the blobs forces the Eich fit to sacrifice precision on the main peak to better describe the far-SOL tail. Thus, besides the increased λ_q , we can also see an underestimation of the main peak, as described for experimental data in Sec.4.2.2.

These first model predictions can successfully reproduce qualitative trends we observed experimentally. However, while before we could "blame" various uncertainties in data acquisition, now we introduce the possibility that errors in Eich fitting are also intrinsic; caused by the limitations of using an Eich function to fit data that is not really Eich-like due to the blobs presence.

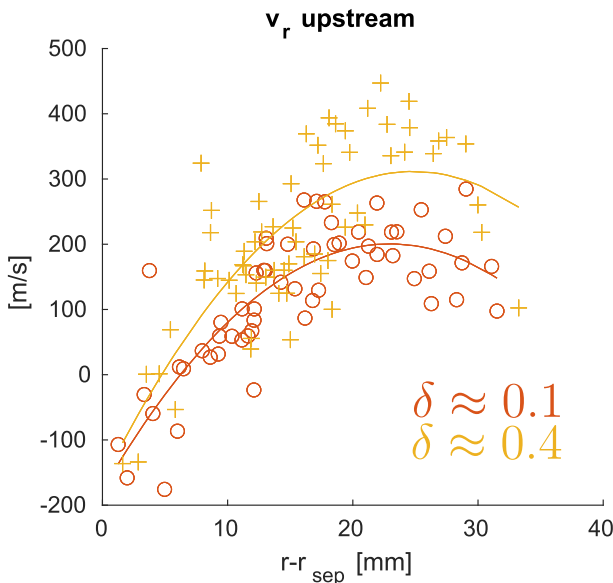


Figure 5.4: v_r profiles across the SOL from Xpt-GPI, rescaled upstream and fitted with a parabola. The shots triangularity δ is also reported.

low issues starts arising with the packing fraction P , which becomes too high and even greater than 1. For these reasons, we forced v_r to be always higher than 50 m/s.

When introducing this velocity profile in the heuristic model, the result is shown in Fig.5.5, where each line is a different shot. The only difference in the model computation is the v_r profile itself, all other parameters were kept the same.

One more theory we can test is the insurgence of the second peak as a consequence of a v_r decrease across the SOL. The v_r profile was taken with Xpt-GPI measurements from shots 78645.78647, already analyzed in Sec.4.3.2. To maintain the same convention applied till here, all data was rescaled to upstream conditions as explained in Sec.2.3. Since we saw most of the blobs were connected and their depends on their midplane behaviour, their radial velocity will be affected by poloidal flux expansion, so that also v_r needs to be rescaled with this parameter.

To later input this changing velocity in the model, it was fitted with a second order polynomial, as shown in Fig.5.4. In this work we did not take into account blobs with negative v_r ; furthermore, if v_r is too

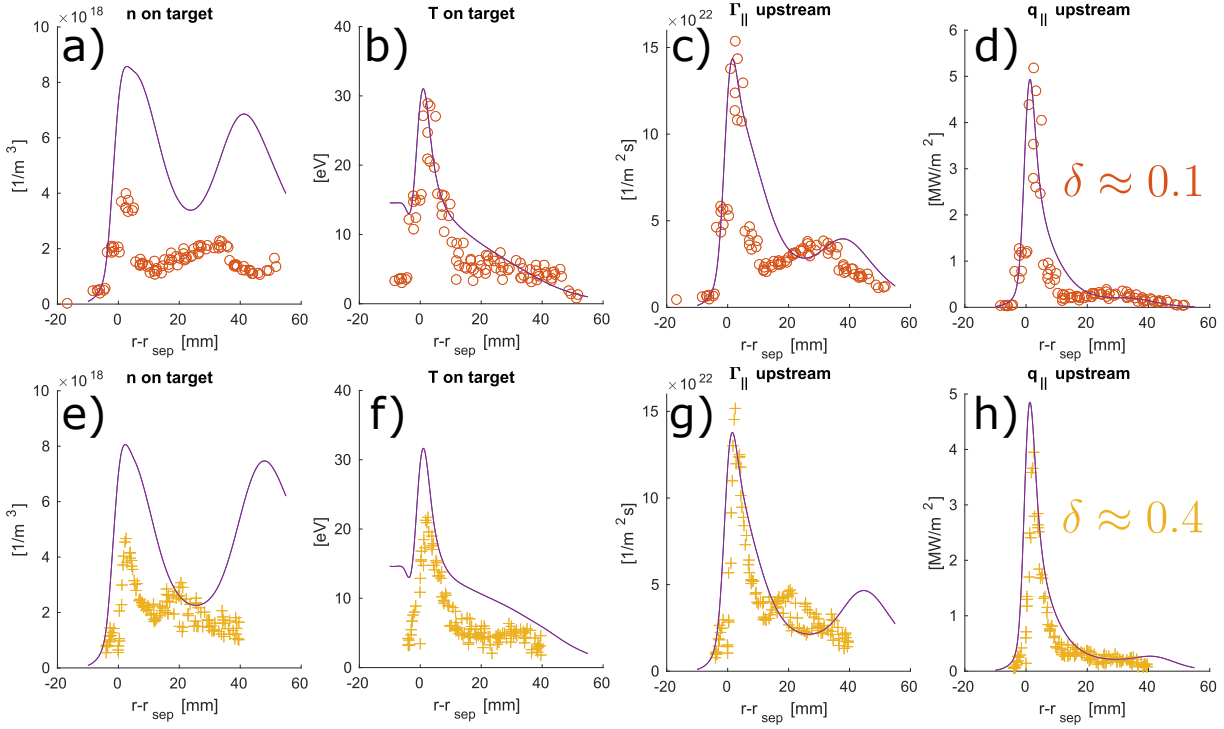


Figure 5.5: Experimental data (scattered in orange and yellow) and model output (purple lines) computed with experimental v_r profiles. a-d) Shot 78645, $\delta \approx 0.1$. e-h) Shot 78647, $\delta \approx 0.4$.

The unperturbed SOL conditions, not being directly measurable, were chosen so that the particle and heat fluxes resembled the experimental ones (panels d-c-g-h). We see from panels (a-b-e-f) that this choice leads to an overestimation of the target features (density especially). This discrepancy probably comes from the simpler manner used by the model to link n and T to the divertor fluxes (Eqs.5.3a, 5.7a) with respect to the more accurate routines exploited by the Langmuir Probes (Sec.3.3), that extrapolate higher fluxes from the same target conditions.

Other than this, the model proves itself capable of reproducing some important qualitative features: first of all, as suggested in Sec.4.2.3, the insurgence of a second peak as a direct consequence of the blobs slowing down. Even if the position of this feature is not perfectly predicted (especially for the PT case), this result holds good potential in improving our predictions of flux profiles on the target.

As recalled in Sec.4.2.3, the presence of a second peak has been partially attributed to drift effects. Here, such drifts have been totally neglected and we showed that filamentary turbulence can also have a role. It is possible that a combination of both phenomena could provide a better quantitative prediction of experimental results: such effort is left for future research.

Another phenomena we can better explain is the experimental observation that the second peak is much more pronounced for the particle flux than for the heat flux. The model predicts in fact (and experimental data confirms) that on the target the density features a strong second peak, while the temperature falls off almost monotonically. This is quite relevant: when computing the fluxes with the model equations we see that $\Gamma_{\parallel} \propto nT$, while $q_{\parallel} \propto nT^{\frac{3}{2}}$. Thus, in the heat flux, the higher weight of the temperature hides the density second peak. This same consideration is also valid for the perpendicular fluxes.

5.3. Limitations and possible improvements

In the previous Section we showed how the heuristic blob model introduced in this Chapter can successfully reproduce various qualitative trends that we experimentally observe and that are not contemplated by the Eich model.

However, in terms of a detailed physical description, the model remains pretty crude: ample spaces for improvement are left for future developments.

An already mentioned possibility is a more realistic description of blobs, substituting the fixed values of velocity, dimensions and appearance frequency used here with distributions obtained from GPI analysis. A major feature that in this work has been neglected is the presence of filaments with negative radial velocity close to the LCFS. These structures could have an heavy impact on the main peak profile, possibly affecting the spreading factor S , which was here found to be mostly independent of filamentary turbulence.

A more complex investigation would be required to assess the connection of filaments from midplane to the target. Here we supposed all filaments were connected, but this is surely not the most realistic description. A correction for disconnected filaments would need some modification of the blobs conductive contribution, while the diffusive one should be unaffected. In any case, we can imagine that the whole energy contained in the blob should finally be delivered the divertor, so that this correction could be considered of secondary importance.

Closely linked to this issue is the behaviour of divertor localized filaments, which here are essentially ignored. Further studies with GPI would be quite beneficial in this respect.

More room for improvement lies in the model set-up parameters. Better estimates for the anomalous diffusive parameters would certainly be beneficial for quantitative conclusions. The same holds true for the unperturbed SOL parameters: a possibility for retrieving better estimates would be to study flux profiles for strongly negative triangularities, in which filamentary turbulence is greatly suppressed. This approach would work supposing that triangularity only affects the blobs phenomenology, without modifying the unper-

turbed profiles. Another way would be to isolate the intermittent blobs contributions on the target from the steady-state SOL. This endeavour is however complicated by the velocity of the blobs, too high for the low LPs sampling rate to distinguish them passing: the final profiles only takes into account the average contributions of the blobs. However if we sacrificed the Four Parameter Fit (Sec.3.3) and with that the estimate of the plasma local density and temperature, to focus on the original current that LPs sample at much higher frequency, then it might be possible to isolate the intermittent blobs contributions from the background signal. Such effort is here proposed, but left for future research.

Finally, in this work we totally neglected the effect of filaments poloidal velocity and size. Whether they have an effect on the target profiles is a question left for future investigation.

6 | Conclusions

Over the last 20 years of fusion research, negative triangularity (NT) has been associated with many desirable plasma features: higher confinement in L-mode operation, a consequent absence of ELMs, a reduction in edge turbulent phenomena, to cite a few. At the same time, however, the heat flux profile on the divertor target was found to be narrower than in comparable positive triangularity (PT) L-mode plasmas, thus discharging more energy on a smaller surface and making it harder to manage this extremely intense heat load.

These results reopened the question whether a future reactor should operate in a PT or NT configuration. Before a conclusive answer can be given, a deeper investigation of the underlying physics is required.

Following this goal, this thesis investigated the role of triangularity and other physical quantities on crucial phenomena happening in the plasma edge. The work was conducted through the analysis of a high number (≈ 100) of plasma shots from the TCV tokamak at the EPFL in Lausanne. As a preliminary preparation, a small number of characteristic shots were analyzed to make sure they operated in the L-mode regime, with a fully attached divertor. To satisfy the latter condition, an upper limit on the plasma line-averaged density was identified at $4.5 \cdot 10^{19} \text{m}^{-3}$. All further analyses were then conducted discarding plasmas whose density exceeded this value.

For each identified shot, we then retrieved the heat flux profile on the divertor target provided via Langmuir Probe measurements. Following the usual practice adopted in the literature, all profiles were rescaled to upstream (midplane) conditions, where they were fitted with an Eich function: a relatively simple analytical function known to well describe these profiles, whose fit parameters can be connected with the underlying physical mechanisms (Eq.2.13). The fitting procedure then allowed to observe the behaviour of each Eich parameter for various changing plasma quantities. The principal conclusions drawn from this are the following:

- The heat flux fall-off length λ_q was observed to steadily decrease for decreasing upper triangularity δ_u (Fig.4.7b). This result, not original per se, was here confirmed with a

higher number of shots and a slightly larger triangularity range than previous studies did. Also, the primary role of δ_u in the triangularity dependence was highlighted, while a role of δ_l was not observed.

A comparison of various λ_q scaling laws with our experimental data identified Lim's correlation [38] as the best candidate and underlined the general need of including triangularity in λ_q correlations, in some form that allows for negative values. In fact, the only scaling law featuring the key parameter δ_u was only defined for $\delta_u > 0$. A decrease of λ_q with higher total injected power P_{tot} was also observed (Fig.4.9).

- The Eich spreading factor S , describing the diffusion of the heat flux profile into the private plasma region was found to be independent of triangularity, but still decreasing for increasing P_{tot} (Fig.4.10).
- The integral of the Eich fit of the heat flux profile is found to consistently underestimate by $\approx 10\%$ the integral of experimental data (Fig.4.11b). Since the area under the Eich function is given by $q_0\lambda_q$ (Eq.4.1) - and supposing λ_q is not affected by this issue - the consequence is an underestimation of the Eich proportionality constant q_0 , which could explain why the main peak of the heat flux profile often looks higher than its fit (Fig.4.11a). This observation also suggests a potentially useful improvement in the Eich fitting process: if the parameter q_0 were to be substituted with the experimental integral of the profile divided by λ_q , we would obtain a function with one less fitting parameter that would not underestimate the total power discharged on the target. Such an investigation is, however, left for future research.

Following the experimental observation that the integral of the heat flux profile is roughly independent of triangularity (Fig.4.12c), the increasing of q_0 for low δ_u (corresponding to lower λ_q) is now partially explained.

Again, the higher q_0 observed in reverse field plasmas is coherent with the lower radiated power observed for this configuration (Fig.4.13a), even if the reason for this behaviour remains unexplained. Finally, the higher uncertainties in the q_0 extrapolation for lower λ_q (Fig.4.14) can be explained in the light of the resulting narrower peak: errors in equilibrium reconstruction and heat flux computation pollute the experimental heat flux profile with uncertainties both in radial position and flux magnitude. When these uncertainties are concentrated into a narrower profile, the fitting operation could be more affected by them, the quality of the fit would decrease and the uncertainties increase.

- An investigation of the second peak in the target flux profiles showed how this is much more notable in the particle flux, rather than in the heat flux. A careful study of its position revealed a positive correlation with the power entering the

SOL (Fig.4.16a) and the width of the outer gap (g_{out} , Fig.4.16c), which suggests that the outer wall can affect this phenomenon. A negative correlation was also found with the line averaged density (at least up to the identified density "limit" of $4.5 \cdot 10^{19} \text{m}^{-3}$ defined in this work, Fig.4.16b).

Finally, following literature results, the direction of the toroidal field (and thus of the $\mathbf{E} \times \mathbf{B}$ drift) was investigated: while some indications of a difference in the second peak position for forward and reverse field were found, the limited parameter range did not allow us to draw conclusive results.

We then focused on the SOL filamentary turbulence, observed with two Gas-Puff Imaging systems (one located at the midplane, the other in the X-point region, Sec.3.2). The acquired data was then analyzed with a Conditional Average Sampling (CAS) method. The principal conclusions were the following:

- The role of negative triangularity in turbulence reduction was confirmed (Fig.4.17).
- Among the blob features detected with CAS, their radial dimension was found to be unaffected by triangularity, while the poloidal one was observed to be significantly lower in plasmas with stronger PT and NT shaping (Figs.4.18d, 4.19).
- An important difference was found in the radial blob velocity v_r in the X-point region: plasmas with positive δ_u featured significantly faster blobs, whose peak velocities was almost double that of negative δ_u cases (Fig.4.21a).
Furthermore, the general v_r profile across the SOL showed that blobs accelerate up to a top speed and then start slowing down. This deceleration could be explained with the presence of the outer wall, which would offer the blob an opportunity of current closure.
- An investigation of the blob parallel extension (Fig.4.22) showed that most of them resulted connected from midplane to the X-point region, with a few exceptions in the lowest region of the Xpt-GPI field of view.

After acknowledging the previous experimental observations, a heuristic blob model was developed to try and connect them (Sec.5.1). Hypothesizing that the target profiles result from a sum of unperturbed SOL fluxes and blob-related fluxes, fluid equations were used to simulate the blobs particle and heat fluxes. The blob features, including their radial velocity, were extrapolated from GPI data. The conducted simulations were successful in:

- reproducing a slowly decaying tail in the far-SOL (Fig.5.2).
- partially explaining the increase of λ_q with the blob radial velocities, and so with triangularity (Fig.5.3). At the same time, an underestimation of the main peak was

similar to the same issue observed on experimental data.

- explaining the insurgence of a second peak, when a realistic v_r profile is used (Fig.5.5). Moreover, the model could reproduce the higher peak in the particle flux and show that the cause is a strong second peak in the target density profile, while the temperature profile does not possess this feature. All these results were found to be compatible with experimental data.

This conclusion constitutes a different explanation of the second peak than the one based on drift effects. In future research, a combination of these ideas could help obtain a better understanding of this phenomenon.

Overall, the model could reproduce many experimental observations, enforcing the idea that SOL turbulence and plasma heat exhaust are strongly connected phenomena and as such they should be studied.

Bibliography

- [1] Jeffrey P. Freidberg. *Plasma Physics and Fusion Energy*. Cambridge University Press, Cambridge, 2007.
- [2] John Wesson. *Tokamaks*. Number 149 in International Series of Monographs on Physics. Oxford Univ. Press, Oxford, 4. ed edition, 2011.
- [3] T. J. M. Boyd and J. J. Sanderson. *The Physics of Plasmas*. Cambridge University Press, Cambridge, UK ; New York, 2003.
- [4] J D Lawson. Some Criteria for a Power Producing Thermonuclear Reactor. *Proceedings of the Physical Society. Section B*, 70(1):6–10, January 1957.
- [5] S. Li, H. Jiang, Z. Ren, and C. Xu. Optimal Tracking for a Divergent-Type Parabolic PDE System in Current Profile Control. *Abstract and Applied Analysis*, 2014:1–8, 2014.
- [6] R.A. Pitts, X. Bonnin, F. Escourbiac, H. Frerichs, J.P. Gunn, T. Hirai, A.S. Kukushkin, E. Kaveeva, M.A. Miller, D. Moulton, V. Rozhansky, I. Senichenkov, E. Sytova, O. Schmitz, P.C. Stangeby, G. De Temmerman, I. Veselova, and S. Wiesen. Physics basis for the first ITER tungsten divertor. *Nuclear Materials and Energy*, 20:100696, August 2019.
- [7] M. Kovari, M. Coleman, I. Cristescu, and R. Smith. Tritium resources available for fusion reactors. *Nuclear Fusion*, 58(2):026010, February 2018.
- [8] V Mukhovatov, M Shimada, A N Chudnovskiy, A E Costley, Y Gribov, G Federici, O Kardaun, A S Kukushkin, A Polevoi, V D Pustovitov, Y Shimomura, T Sugie, M Sugihara, and G Vayakis. Overview of physics basis for ITER. *Plasma Physics and Controlled Fusion*, 45(12A):A235–A252, December 2003.
- [9] <https://www.iter.org/sci/iterandbeyond>.
- [10] G. Federici, W. Biel, M.R. Gilbert, R. Kemp, N. Taylor, and R. Wenninger. European DEMO design strategy and consequences for materials. *Nuclear Fusion*, 57(9):092002, September 2017.

- [11] Peter C Stangeby. *The plasma boundary of magnetic fusion devices*, volume 224. Institute of Physics Pub. Philadelphia, Pennsylvania, 2000.
- [12] <https://wiki.fusion.ciemat.es/wiki/triangularity>.
- [13] A. Marinoni, O. Sauter, and S. Coda. A brief history of negative triangularity tokamak plasmas. *Reviews of Modern Plasma Physics*, 5(1):6, December 2021.
- [14] Nicola Offeddu. 3D Characterisation of Turbulent Plasma Filaments Using Gas Puff Imaging in the Tokamak à Configuration Variable. March 2023.
- [15] F. Wagner, G. Becker, K. Behringer, D. Campbell, A. Eberhagen, W. Engelhardt, G. Fussmann, O. Gehre, J. Gernhardt, G. V. Gierke, G. Haas, M. Huang, F. Karger, M. Keilhacker, O. Klüber, M. Kornherr, K. Lackner, G. Lisitano, G. G. Lister, H. M. Mayer, D. Meisel, E. R. Müller, H. Murmann, H. Niedermeyer, W. Poschenrieder, H. Rapp, H. Röhr, F. Schneider, G. Siller, E. Speth, A. Stäbler, K. H. Steuer, G. Venus, O. Vollmer, and Z. Yü. Regime of Improved Confinement and High Beta in Neutral-Beam-Heated Divertor Discharges of the ASDEX Tokamak. *Physical Review Letters*, 49(19):1408–1412, November 1982.
- [16] ASDEX Team. The H-Mode of ASDEX. *Nuclear Fusion*, 29(11):1959–2040, November 1989.
- [17] A. Loarte, G. Huijsmans, S. Futatani, L.R. Baylor, T.E. Evans, D. M. Orlov, O. Schmitz, M. Becoulet, P. Cahyna, Y. Gribov, A. Kavin, A. Sashala Naik, D.J. Campbell, T. Casper, E. Daly, H. Frerichs, A. Kischner, R. Laengner, S. Lisgo, R.A. Pitts, G. Saibene, and A. Wingen. Progress on the application of ELM control schemes to ITER scenarios from the non-active phase to DT operation. *Nuclear Fusion*, 54(3):033007, March 2014.
- [18] J.P. Gunn, S. Carpentier-Chouchana, F. Escourbiac, T. Hirai, S. Panayotis, R.A. Pitts, Y. Corre, R. Dejarnac, M. Firdaouss, M. Kočan, M. Komm, A. Kukushkin, P. Languille, M. Missirlian, W. Zhao, and G. Zhong. Surface heat loads on the ITER divertor vertical targets. *Nuclear Fusion*, 57(4):046025, April 2017.
- [19] M. E. Austin, A. Marinoni, M. L. Walker, M. W. Brookman, J. S. deGrassie, A. W. Hyatt, G. R. McKee, C. C. Petty, T. L. Rhodes, S. P. Smith, C. Sung, K. E. Thome, and A. D. Turnbull. Achievement of Reactor-Relevant Performance in Negative Triangularity Shape in the DIII-D Tokamak. *Physical Review Letters*, 122(11):115001, March 2019.
- [20] Y Camenen, A Pochelon, R Behn, A Bottino, A Bortolon, S Coda, A Karpushov,

- O Sauter, G Zhuang, and The Tcv Team. Impact of plasma triangularity and collisionality on electron heat transport in TCV L-mode plasmas. *Nuclear Fusion*, 47(7):510–516, July 2007.
- [21] S Coda, A Merle, O Sauter, L Porte, F Bagnato, J Boedo, T Bolzonella, O Février, B Labit, A Marinoni, A Pau, L Pigatto, U Sheikh, C Tsui, M Vallar, and T Vu. Enhanced confinement in diverted negative-triangularity L-mode plasmas in TCV. *Plasma Physics and Controlled Fusion*, 64(1):014004, January 2022.
- [22] M. Fontana, L. Porte, S. Coda, O. Sauter, and The TCV Team. The effect of triangularity on fluctuations in a tokamak plasma. *Nuclear Fusion*, 58(2):024002, February 2018.
- [23] W. Han, N. Offeddu, T. Golfopoulos, C. Theiler, C.K. Tsui, J.A. Boedo, E.S. Marmor, and The Tcv Team. Suppression of first-wall interaction in negative triangularity plasmas on TCV. *Nuclear Fusion*, 61(3):034003, March 2021.
- [24] A. Marinoni, M.E. Austin, A.W. Hyatt, S. Saarelma, F. Scotti, Z. Yan, C. Chrystal, S. Coda, F. Glass, J.M. Hanson, A.G. McLean, D.C. Pace, C. Paz-Soldan, C.C. Petty, M. Porkolab, L. Schmitz, F. Sciortino, S.P. Smith, K.E. Thome, F. Turco, and The Diii-D Team. Diverted negative triangularity plasmas on DIII-D: The benefit of high confinement without the liability of an edge pedestal. *Nuclear Fusion*, 61(11):116010, November 2021.
- [25] T. Eich, A.W. Leonard, R.A. Pitts, W. Fundamenski, R.J. Goldston, T.K. Gray, A. Herrmann, A. Kirk, A. Kallenbach, O. Kardaun, A.S. Kukushkin, B. LaBombard, R. Maingi, M.A. Makowski, A. Scarabosio, B. Sieglin, J. Terry, A. Thornton, ASDEX Upgrade Team, and JET EFDA Contributors. Scaling of the tokamak near the scrape-off layer H-mode power width and implications for ITER. *Nuclear Fusion*, 53(9):093031, September 2013.
- [26] T. Eich, B. Sieglin, A. Scarabosio, W. Fundamenski, R. J. Goldston, A. Herrmann, and ASDEX Upgrade Team. Inter-ELM Power Decay Length for JET and ASDEX Upgrade: Measurement and Comparison with Heuristic Drift-Based Model. *Physical Review Letters*, 107(21):215001, November 2011.
- [27] B Sieglin, T Eich, M Faitsch, A Herrmann, A Scarabosio, and the ASDEX Upgrade Team. Investigation of scrape-off layer and divertor heat transport in ASDEX Upgrade L-mode. *Plasma Physics and Controlled Fusion*, 58(5):055015, May 2016.
- [28] R. Maurizio, S. Elmore, N. Fedorczak, A. Gallo, H. Reimerdes, B. Labit, C. Theiler, C.K. Tsui, W.A.J. Vijvers, The TCV Team, and The MST1 Team. Divertor power

- load studies for attached L-mode single-null plasmas in TCV. *Nuclear Fusion*, 58(1):016052, January 2018.
- [29] A Loarte, S Bosch, A Chankin, S Clement, A Herrmann, D Hill, K Itami, J Lingertat, B Lipschultz, K McCormick, R Monk, G.D Porter, M Shimada, and M Sugihara. Multi-machine scaling of the divertor peak heat flux and width for L-mode and H-mode discharges. *Journal of Nuclear Materials*, 266–269:587–592, March 1999.
- [30] M. A. Makowski, D. Elder, T. K. Gray, B. LaBombard, C. J. Lasnier, A. W. Leonard, R. Maingi, T. H. Osborne, P. C. Stangeby, J. L. Terry, and J. Watkins. Analysis of a multi-machine database on divertor heat fluxes. *Physics of Plasmas*, 19(5):056122, May 2012.
- [31] S.B. Ballinger, D. Brunner, A.E. Hubbard, J.W. Hughes, A.Q. Kuang, B. LaBombard, J.L. Terry, and A.E. White. Dependence of the boundary heat flux width on core and edge profiles in Alcator C-Mod. *Nuclear Fusion*, 62(7):076020, July 2022.
- [32] M Faitsch, R Maurizio, A Gallo, S Coda, T Eich, B Labit, A Merle, H Reimerdes, B Sieglin, C Theiler, the Eurofusion MST1 Team, and the TCV Team. Dependence of the L-Mode scrape-off layer power fall-off length on the upper triangularity in TCV. *Plasma Physics and Controlled Fusion*, 60(4):045010, April 2018.
- [33] T. Eich, B. Sieglin, A. Scarabosio, A. Herrmann, A. Kallenbach, G.F. Matthews, S. Jachmich, S. Brezinsek, M. Rack, and R.J. Goldston. Empirical scaling of inter-ELM power widths in ASDEX Upgrade and JET. *Journal of Nuclear Materials*, 438:S72–S77, July 2013.
- [34] A. Scarabosio, T. Eich, A. Herrmann, and B. Sieglin. Outer target heat fluxes and power decay length scaling in L-mode plasmas at JET and AUG. *Journal of Nuclear Materials*, 438:S426–S430, July 2013.
- [35] D. Brunner, B. LaBombard, A.Q. Kuang, and J.L. Terry. High-resolution heat flux width measurements at reactor-level magnetic fields and observation of a unified width scaling across confinement regimes in the Alcator C-Mod tokamak. *Nuclear Fusion*, 58(9):094002, September 2018.
- [36] D Silvagni, T Eich, M Faitsch, T Happel, B Sieglin, P David, D Nille, L Gil, and U Stroth. Scrape-off layer (SOL) power width scaling and correlation between SOL and pedestal gradients across L, I and H-mode plasmas at ASDEX Upgrade. *Plasma Physics and Controlled Fusion*, 62(4):045015, April 2020.
- [37] J. Horacek, J. Adamek, M. Komm, J. Seidl, P. Vondracek, A. Jardin, Ch. Guillemaut,

- S. Elmore, A. Thornton, K. Jirakova, F. Jaulmes, G. Deng, X. Gao, L. Wang, R. Ding, D. Brunner, B. LaBombard, J. Olsen, J.J. Rasmussen, A.H. Nielsen, V. Naulin, M. Ezzat, K.M. Camacho, M. Hron, and G.F. Matthews. Scaling of L-mode heat flux for ITER and COMPASS-U divertors, based on five tokamaks. *Nuclear Fusion*, 60(6):066016, June 2020.
- [38] K Lim, M Giacomini, P Ricci, A Coelho, O Février, D Mancini, D Silvagni, and L Stenger. Effect of triangularity on plasma turbulence and the SOL-width scaling in L-mode diverted tokamak configurations. *Plasma Physics and Controlled Fusion*, 65(8):085006, August 2023.
- [39] D. Carralero, S. Artene, M. Bernert, G. Birkenmeier, M. Faitsch, P. Manz, P. De Marne, U. Stroth, M. Wischmeier, E. Wolfrum, The ASDEX Upgrade Team, and The EURO-fusion MST1 Team. On the role of filaments in perpendicular heat transport at the scrape-off layer. *Nuclear Fusion*, 58(9):096015, September 2018.
- [40] W. Han, N. Offeddu, T. Golfopoulos, C. Theiler, J.L. Terry, C. Wüthrich, D. Galassi, C. Colandrea, and E.S. Marmor. Estimating cross-field particle transport at the outer midplane of TCV by tracking filaments with machine learning. *Nuclear Fusion*, 63(7):076025, July 2023.
- [41] J. A. Boedo, D. L. Rudakov, R. A. Moyer, G. R. McKee, R. J. Colchin, M. J. Schaffer, P. G. Stangeby, W. P. West, S. L. Allen, T. E. Evans, R. J. Fonck, E. M. Hollmann, S. Krasheninnikov, A. W. Leonard, W. Nevins, M. A. Mahdavi, G. D. Porter, G. R. Tynan, D. G. Whyte, and X. Xu. Transport by intermittency in the boundary of the DIII-D tokamak. *Physics of Plasmas*, 10(5):1670–1677, May 2003.
- [42] J. R. Myra, D. A. D’Ippolito, D. P. Stotler, S. J. Zweben, B. P. LeBlanc, J. E. Menard, R. J. Maqueda, and J. Boedo. Blob birth and transport in the tokamak edge plasma: Analysis of imaging data. *Physics of Plasmas*, 13(9):092509, September 2006.
- [43] C. Theiler, I. Furno, P. Ricci, A. Fasoli, B. Labit, S. H. Müller, and G. Plyushchev. Cross-Field Motion of Plasma Blobs in an Open Magnetic Field Line Configuration. *Physical Review Letters*, 103(6):065001, August 2009.
- [44] J. R. Myra, D. A. Russell, and D. A. D’Ippolito. Collisionality and magnetic geometry effects on tokamak edge turbulent transport. I. A two-region model with application to blobs. *Physics of Plasmas*, 13(11):112502, November 2006.
- [45] N. Offeddu, W. Han, C. Theiler, T. Golfopoulos, J.L. Terry, E. Marmor, C. Wüthrich, C.K. Tsui, H. De Oliveira, B.P. Duval, D. Galassi, D.S. Oliveira,

- D. Mancini, and The Tcv Team. Cross-field and parallel dynamics of SOL filaments in TCV. *Nuclear Fusion*, 62(9):096014, September 2022.
- [46] D Farina, R Pozzoli, and D.D Ryutov. Effect of the magnetic field geometry on the flute-like perturbations near the divertor X point. *Nuclear Fusion*, 33(9):1315–1317, September 1993.
- [47] F. Nespoli, P. Tamain, N. Fedorczak, D. Galassi, and Y. Marandet. A new mechanism for filament disconnection at the X-point: Poloidal shear in radial $E \times B$ velocity. *Nuclear Fusion*, 60(4):046002, April 2020.
- [48] C. Wüthrich, C. Theiler, N. Offeddu, D. Galassi, D.S. Oliveira, B.P. Duval, O. Février, T. Golfinopoulos, W. Han, E. Marmar, J.L. Terry, C.K. Tsui, and The Tcv Team. X-point and divertor filament dynamics from gas puff imaging on TCV. *Nuclear Fusion*, 62(10):106022, October 2022.
- [49] D. A. D’Ippolito, J. R. Myra, and S. J. Zweben. Convective transport by intermittent blob-filaments: Comparison of theory and experiment. *Physics of Plasmas*, 18(6):060501, June 2011.
- [50] D. Carralero, G. Birkenmeier, H.W. Müller, P. Manz, P. deMarne, S.H. Müller, F. Reimold, U. Stroth, M. Wischmeier, E. Wolfrum, and The ASDEX Upgrade Team. An experimental investigation of the high density transition of the scrape-off layer transport in ASDEX Upgrade. *Nuclear Fusion*, 54(12):123005, December 2014.
- [51] E. Laribi, E. Serre, P. Tamain, and H. Yang. Impact of negative triangularity on edge plasma transport and turbulence in TOKAM3X simulations. *Nuclear Materials and Energy*, 27:101012, June 2021.
- [52] C. Theiler, B. Lipschultz, J. Harrison, B. Labit, H. Reimerdes, C. Tsui, W.A.J. Vijvers, J. A. Boedo, B.P. Duval, S. Elmore, P. Innocente, U. Kruezi, T. Lunt, R. Maurizio, F. Nespoli, U. Sheikh, A.J. Thornton, S.H.M. Van Limpt, K. Verhaegh, and N. Vianello. Results from recent detachment experiments in alternative divertor configurations on TCV. *Nuclear Fusion*, 57(7):072008, July 2017.
- [53] A. Kallenbach, M. Bernert, M. Beurskens, L. Casali, M. Dunne, T. Eich, L. Giannone, A. Herrmann, M. Maraschek, S. Potzel, F. Reimold, V. Rohde, J. Schweinzer, E. Viezzer, M. Wischmeier, and the ASDEX Upgrade Team. Partial detachment of high power discharges in ASDEX Upgrade. *Nuclear Fusion*, 55(5):053026, May 2015.
- [54] A Loarte, R.D Monk, J.R Martín-Solís, D.J Campbell, A.V Chankin, S Clement, S.J Davies, J Ehrenberg, S.K Erents, H.Y Guo, P.J Harbour, L.D Horton, L.C Ingesson,

- H Jäckel, J Lingertat, C.G Lowry, C.F Maggi, G.F Matthews, K McCormick, D.P O'Brien, R Reichle, G Saibene, R.J Smith, M.F Stamp, D Stork, and G.C Vlases. Plasma detachment in JET Mark I divertor experiments. *Nuclear Fusion*, 38(3):331–371, March 1998.
- [55] O. Février, C. K. Tsui, G. Durr-Legoupil-Nicoud, C. Theiler, M. Carpita, S. Coda, C. Colandrea, B. P. Duval, S. Gorno, E. Huett, B. Linehan, A. Perek, L. Porte, H. Reimerdes, O. Sauter, E. Tonello, M. Zurita, T. Bolzonella, F. Sciortino, the TCV Team, and the EUROfusion Tokamak Exploitation Team. Comparison of detachment in Ohmic plasmas with positive and negative triangularity. 2023.
- [56] F Hofmann, J B Lister, W Anton, S Barry, R Behn, S Bernel, G Besson, F Buhlmann, R Chavan, M Corboz, M J Dutch, B P Duval, D Fasel, A Favre, S Franke, A Heym, A Hirt, C Hollenstein, P Isoz, B Joye, X Llobet, J C Magnin, B Marletaz, P Marmillod, Y Martin, J M Mayor, J M Moret, C Nieswand, P J Paris, A Perez, Z A Pietrzyk, R A Pitts, A Pochelon, R Rage, O Sauter, G Tonetti, M Q Tran, F Troyon, D J Ward, and H Weisen. Creation and control of variably shaped plasmas in TCV. *Plasma Physics and Controlled Fusion*, 36(12B):B277–B287, December 1994.
- [57] <https://www.epfl.ch/research/domains/swiss-plasma-center/research/tcv>.
- [58] R. J. Maqueda, G. A. Wurden, D. P. Stotler, S. J. Zweben, B. LaBombard, J. L. Terry, J. L. Lowrance, V. J. Mastrocola, G. F. Renda, D. A. D'Ippolito, J. R. Myra, and N. Nishino. Gas puff imaging of edge turbulence (invited). *Review of Scientific Instruments*, 74(3):2020–2026, March 2003.
- [59] N. Offeddu, C. Wüthrich, W. Han, C. Theiler, T. Golfinopoulos, J. L. Terry, E. Marmar, C. Galperti, Y. Andrebe, B. P. Duval, R. Bertizzolo, A. Clement, O. Février, H. Elaian, D. Gönczy, J. D. Landis, and TCV Team. Gas puff imaging on the TCV tokamak. *Review of Scientific Instruments*, 93(12):123504, December 2022.
- [60] N. Offeddu, C. Wüthrich, W. Han, C. Theiler, T. Golfinopoulos, J. L. Terry, E. Marmar, A. Ravetta, and G. Van Parys. Analysis techniques for blob properties from gas puff imaging data. *Review of Scientific Instruments*, 94(3):033512, March 2023.
- [61] O. Février, C. Theiler, H. De Oliveira, B. Labit, N. Fedorczak, and A. Baillod. Analysis of wall-embedded Langmuir probe signals in different conditions on the Tokamak à Configuration Variable. *Review of Scientific Instruments*, 89(5):053502, May 2018.
- [62] D Brida, D Silvagni, T Eich, M Faitsch, P McCarthy, the ASDEX Upgrade Team, and the MST1 Team. Role of electric currents for the SOL and divertor target heat

- fluxes in ASDEX Upgrade. *Plasma Physics and Controlled Fusion*, 62(10):105014, October 2020.
- [63] Mirko Wensing. *Drift-Related Transport and Plasma-Neutral Interaction in the TCV Divertor*. PhD thesis, EPFL, 2021.
- [64] Uron Kruezi, G. Sergienko, P. D. Morgan, G. F. Matthews, S. Brezinsek, S. Vartanian, and JET-EFDA Contributors. JET divertor diagnostic upgrade for neutral gas analysis. *Review of Scientific Instruments*, 83(10):10D728, October 2012.
- [65] A. Niemczewski. *Neutral particle dynamics in the Alcator C-Mod tokamak*. PhD thesis, Massachusetts Institute of Technology, 1995.
- [66] A. Perek, W. A. J. Vijvers, Y. Andrebe, I. G. J. Classen, B. P. Duval, C. Galperti, J. R. Harrison, B. L. Linehan, T. Ravensbergen, K. Verhaegh, M. R. De Baar, TCV, and EUROfusion MST1 Teams. MANTIS: A real-time quantitative multispectral imaging system for fusion plasmas. *Review of Scientific Instruments*, 90(12):123514, December 2019.
- [67] T.D. Rognlien, G.D. Porter, and D.D. Ryutov. Influence of $\mathbf{E} \times \mathbf{B}$ and ∇B drift terms in 2-D edge/SOL transport simulations. *Journal of Nuclear Materials*, 266–269:654–659, March 1999.
- [68] A V Chankin, G Corrigan, S K Erents, G F Matthews, J Spence, and P C Stangeby. Possible explanation for doubly peaked profiles at the divertor target in JET. *Plasma Physics and Controlled Fusion*, 43(3):299–304, March 2001.
- [69] V. Rozhansky, P. Molchanov, I. Veselova, S. Voskoboynikov, A. Kirk, and D. Coster. Contribution of drifts and parallel currents to divertor asymmetries. *Nuclear Fusion*, 52(10):103017, October 2012.
- [70] N Christen, C Theiler, Td Rognlien, Me Rensink, H Reimerdes, R Maurizio, and B Labit. Exploring drift effects in TCV single-null plasmas with the UEDGE code. *Plasma Physics and Controlled Fusion*, 59(10):105004, October 2017.
- [71] L. Vermare, P. Hennequin, C. Honoré, M. Peret, G. Dif-Pradalier, X. Garbet, J. Gunn, C. Bourdelle, F. Clairet, J. Morales, R. Dumont, M. Goniche, P. Maget, R. Varennes, and The West Team. Formation of the radial electric field profile in the WEST tokamak. *Nuclear Fusion*, 62(2):026002, February 2022.

A | Appendix A

A.1. List of exploited TCV shots

In Sec.4.1 we described the creation of a TCV shots database, which was then extensively used in Sec.4.2 for the study of the heat fluxes on the divertor target. Some of the shots also provided GPI data, used in Sec.4.3 for the study of SOL filamentary turbulence.

The following Tables contain a comprehensive list of all TCV shots analyzed in this thesis, along with their triangularity value.

The reader should keep in mind that:

- From all shots listed in Table A.1 we extracted LP data to retrieve the divertor target heat flux and analyze it. However, one can notice that all figures in Sec.4.2 contain much less data points than the number of shots shown here. The reason is that a lot of data had to be discarded for the reason explained in Secs.4.1, 4.2 (too high density, bad LP data, too high fitting errors, ...).
- GPI data could be taken only for a limited number of shots, listed in Table A.2.
- Some shot numbers are repeated with different δ values: those shots were created to run a triangularity scan and multiple time intervals were considered independently.

TCV shot	δ						
52783	0,15	77237	0,17	79371	0,01	79383	0,27
52785	0,44	77241	0,41	79371	0,14	79383	0,39
52787	0,31	78102	0,1	79371	0,26	79412	0,37
52789	0,53	78103	0,39	79375	0,42	79412	-0,14
67070	-0,29	78287	0,24	79375	0,37	79414	-0,13
67072	0,28	78291	-0,04	79375	0,26	79428	0,39
67081	-0,18	78540	-0,14	79375	0,14	79430	-0,04
67084	-0,29	78543	0,15	79375	0,02	79433	0,24
67465	-0,28	78544	0,39	79375	-0,08	79435	-0,14
67467	0,27	78545	0,4	79377	0,37	79436	-
69821	-0,28	78546	0,11	79377	0,26	79917	-0,1
69957	-0,18	78645	0,11	79377	0,14	79954	-0,08
69962	0,1	78647	0,38	79377	-0,01	80007	-0,1
72855	-0,27	79153	0,39	79377	-0,09	80007	-0,11
72856	-0,22	79156	0,13	79380	0,41	80024	-0,1
72861	-0,15	79162	0,1	79381	-0,15	80024	-0,09
72862	-0,1	79163	0,11	79381	-0,09	80028	-0,09
72863	-0,2	79213	0,4	79381	0,01	80028	-0,08
73398	0,11	79230	0,12	79381	0,14	80028	-0,06
73399	-0,13	79267	0,04	79381	0,27	80029	-0,11
73400	-0,13	79268	0,06	79381	0,4	80029	-0,12
73401	0,12	79269	0,05	79383	-0,09	80029	-0,11
77235	0,17	79270	0,07	79383	0,01		
77236	0,41	79371	-0,14	79383	0,14		

Table A.1: TCV shots exploited for LPs target heat flux analysis, with triangularity value.

TCV shot	Omp-GPI	Xpt-GPI	TCV shot	Omp-GPI	Xpt-GPI
69821	★		79157	★	
78645	★	★	79158	★	
78647	★	★	79228		★
79153	★		79268	★	★
79156	★		79270	★	★

Table A.2: TCV shots exploited for GPI SOL turbulence analysis.

List of Figures

1.1	Deuterium-tritium fusion scheme.	1
1.2	Nuclei binding energy per nucleon	2
1.3	Reaction rates for various fusion reactions.	4
1.4	Tokamak and Stellarator schemes	7
1.5	Scheme of the ITER tokamak	10
2.1	Limited and diverted configurations	14
2.2	Scheme of two flux surfaces and two ribbons connecting them	16
2.3	Plasma geometry	18
2.4	Comparison of different triangularity plasmas	19
2.5	Orientation of magnetic field at the target	20
2.6	Evolution of the heat flux profile from upstream to the divertor target	25
2.7	Formation mechanism of the edge filaments	28
2.8	Divertor localized blobs poloidal velocity	29
3.1	Different plasma shapes achieved in TCV	35
3.2	Scheme of the GPI system on TCV	37
3.3	Locations in TCV of some diagnostics used in this thesis	42
4.1	Characteristic shots geometry	46
4.2	D_α radiation and line averaged density for checking the confinement regime	47
4.3	C-III front movement and neutrals pressure	48
4.4	Integrated particle flux and DoD	49
4.5	Some heat flux profiles	49
4.6	Example of Eich fit	50
4.7	Comparison of λ_q correlations and experimental data	51
4.8	Linear regressions of λ_q scaling laws and experimental data	52
4.9	λ_q against total input power	53
4.10	Eich spreading factor S against δ_u , P_{tot} and $L_{ }$	54
4.11	a)Example of an Eich fit with bad q_0 estimation	55
4.12	q_0 , peak, and integrated heat flux in a triangularity scan	56

4.13	Fraction of radiated power and λ_q against δ_u	57
4.14	q_0 error dependency on λ_q	57
4.15	Comparison of particle and heat flux profiles for second peak identification	58
4.16	Influence of P_{SOL} , $\langle n_e \rangle$ and g_{out} on the second peak position	59
4.17	Average midplane GPI fluctuations with changing triangularity	60
4.18	Sizes and velocities of CAS analyzed blobs at the outer midplane	62
4.19	Omp-GPI CAS triggering frames for shots with changing δ at $\rho_\Psi \approx 1.05$. .	62
4.20	Average X-point GPI fluctuations with changing triangularity	63
4.21	Sizes and velocities of CAS analyzed blobs close to the X-point	64
4.22	Ellipticity (a-c) and poloidal velocity (b-d) for X-point GPI trigger points for changing δ	65
4.23	Xpt-GPI field of view separation in lower core and leg regions	66
4.24	Blob velocities and sizes from midplane to X-point	67
5.1	Filament description for the heuristic model	73
5.2	Example of heuristic blob model output	77
5.3	Simulated effect of blobs v_r on λ_q	78
5.4	v_r profiles across the SOL from Xpt-GPI	79
5.5	Model output and experimental data	80

List of Tables

2.1	Some scaling laws for λ_q	26
4.1	Parameter ranges for the TCV shots used in this thesis	45
4.2	R^2 increase after correction for various scaling laws.	53
4.3	Number of GPI shots divided for triangularity and GPI location.	66
5.1	Typical parameters for heuristic model computation.	76
A.1	TCV shots exploited for LPs target heat flux analysis	96
A.2	TCV shots exploited for GPI SOL turbulence analysis	96

List of Symbols

Variable	Description	SI unit
"0"	Model's superscript indicating unperturbed values	[-]
" \perp "	Model's subscript indicating fluxes across blobs lateral surface	[-]
a	Plasma minor radius	[m]
A	Ions mass number	[-]
A	Flux tube cross-section	[m ²]
A_{\perp}	Model's blobs lateral surface	[m ²]
\mathbf{A}	Magnetic vector potential	[T · m]
"blobs"	Model's superscript indicating blobs values	[-]
\mathbf{B}	Magnetic field	[T]
\mathbf{B}_{pol}	Poloidal magnetic field	[T]
\mathbf{B}_{tor}	Toroidal magnetic field	[T]
c	Ions/plasma sound speed	[m/s]
"cond"	Model's superscript indicating conductive fluxes	[-]
C	Curvature coefficient	[V/m]
"diff"	Model's superscript indicating diffusive fluxes	[-]
d_{sep}	Distance from separatrix	[m]
D_{\perp}	Cross-field mass diffusivity	[m ² /s]
DoD	Degree of detachment	[-]
dr	Distance from separatrix	[m]
dt	Model's time increment	[s]
e	Elementary charge	[C]
E_{rec}	Hydrogen ion and molecule recombination energy	[J]
\mathbf{E}	Electric field	[V/m]
f_{gw}	Greenwald fraction	[-]

Variable	Description	SI unit
f_x	Total flux expansion	[-]
$f_{x,pol}$	Poloidal flux expansion	[-]
$f_{x,pol}^*$	Effective poloidal flux expansion	[-]
g_{out}	Outer gap width	[m]
h	Model's T and n fluctuations ratio at separatrix	[-]
I	GPI light brightness	[W/(m ² ·sr)]
\bar{I}	GPI light brightness, time moving average	[W/(m ² ·sr)]
I_p	Plasma current	[A]
I_{sat}	LPs saturation current	[A]
\mathbf{J}	Plasma current density field	[A/m ²]
J_{net}	LPs net current density	[A/m ²]
J_{sat}	LPs saturation current density	[A/m ²]
k	Boltzmann constant	[m ² ·Kg/(s ² ·K)]
L_χ	Poloidal length at LCFS	[m]
$L_{ }$	Connection length	[m]
m_e	Electron mass	[Kg]
m_i	Ion mass	[Kg]
n	(= $n_e = n_i$) Electron, ion density	[m ⁻³]
\hat{n}	Normal versor	[-]
n_e	(Electron) density	[m ⁻³]
$\langle n_e \rangle$	(Electron) line-averaged density	[m ⁻³]
n_0	GPI neutral gas density	[m ⁻³]
p	GPI probability of a certain blob feature	[-]
p	Plasma pressure	[Pa]
\bar{p}	Volume averaged core plasma pressure	[Pa]
$p_{e,95}$	Electron pressure at $\rho_\Psi = 0.95$	[Pa]
P	Blobs packing fraction	[-]
P_{rad}	Power radiated by the core	[W]
P_{SOL}	Power flowing from plasma core to SOL	[W]
P_{tot}	Total power injected into plasma	[W]
q	Safety factor	[-]

Variable	Description	SI unit
q_{bg}	Eich fitting parameter: background heat flux	[W/m ²]
q_{cyl}	Cylindrical safety factor	[-]
q_{int}	Experimental area under heat flux profile	[W/m]
q_{int}^{Eich}	Area under Eich function	[W/m]
q_0	Eich fitting parameter: proportionality constant	[W/m ²]
q_{95}	Safety factor at $\rho_{\Psi} = 0.95$	[-]
$q_{ }$	Heat flux, parallel to magnetic field lines	[W/m ²]
r_0	Model's blobs starting position	[m]
R	Plasma major radius	[m]
R	Model's density fluctuation at separatrix	[-]
$\hat{\mathbf{R}}$	radial versor	[-]
R_E	LPs ions energy reflection coefficient	[-]
\bar{s}	Eich fitting: target curvilinear coordinate	[m]
"sep"	Model's subscript indicating separatrix values	[-]
S	Eich fitting parameter: spreading factor	[m]
S	LPs effective probe collection area	[-]
S	GPI normalized signal	[-]
\bar{S}	GPI CAS signal	[-]
S_{eff}	GPI gas cloud FWHM	[m]
t	Time	[s]
"t"	Subscript or superscript, refers to target conditions	[-]
T	(= $T_e = T_i$) Electron, ion temperature	[K]
T_e	Electron temperature	[K]
T_i	Ion temperature	[K]
"u"	Subscript or superscript, refers to upstream conditions	[-]
\mathbf{v}_r	Blobs radial velocity	[m/s]
\mathbf{v}_θ	Blobs poloidal velocity	[m/s]
V_{fl}	Wall floating potential	[V]
V_{pr}	LPs applied potential	[V]
V_{pre-sh}	Pre-sheath potential drop	[V]
$\hat{\mathbf{Z}}$	Vertical versor	[-]

Variable	Description	SI unit
α	LPs sheath expansion coefficient	[-]
χ_{\perp}	Cross-field thermal diffusivity	[m ² /s]
δ	Plasma triangularity	[-]
δ_l	Plasma lower triangularity	[-]
δ_r	Blobs radial dimension	[m]
δ_u	Plasma upper triangularity	[-]
δ_{θ}	Blobs poloidal dimension	[m]
ϵ	Tokamak aspect ratio	[-]
ϵ	GPI light emissivity	[1/(m ³ ·s·sr)]
γ	Sheath heat transmission coefficient	[-]
Γ_{\parallel}	Particle flux, parallel to magnetic field lines	[1/(m ² ·s)]
κ	Plasma elongation	[-]
κ_{0e}	Electron parallel conductivity coefficient	[W/(m·K ^{7/2})]
λ	Wavelength	[m]
λ_{int}	Heat flux integral decay length	[m]
λ_n	Target density profile fall-off length	[m]
λ_q	Eich fitting parameter: fall-off length	[m]
λ_T	Target temperature profile fall-off length	[m]
μ	GPI smoothed and time-averaged brightness	[W/(m ² ·sr)]
ν_{SOL}	SOL collisionality	[-]
$\widehat{\Phi}$	Toroidal versor	[-]
Ψ	Poloidal flux function	[T·m ²]
Ψ_0	Ψ Value on magnetic axis	[T·m ²]
ρ_{Ψ}	Plasma coordinate, constant on flux surfaces	[-]
σ	GPI smoothed and time-averaged brightness standard dev.	[W/(m ² ·sr)]

Acknowledgements

I am deeply grateful to my supervisor, Prof. Matteo Passoni, for guiding me through the fundamental process of writing the thesis and for explaining to me the importance of the little, big details.

Similarly, I owe my most sincere thanks to my co-supervisors Prof. Christian Theiler and Dr. Theodore Golfinopoulos, as well as to Yinghan Wang, for making me feel welcomed at EPFL and MIT, for their invaluable support, guidance, suggestions and freedom they granted me during the months we worked together.

To my parents, my sister and my brother, who have been supporting me for 25 years, thank you for having always pushed me to do better and not to be satisfied with sufficient results: without you I certainly wouldn't be standing where I am now.

To all my friends, thank you for always being there for me. Whenever I imagine what my life would be if I hadn't met you, I can grasp how much you have given me and how much you made me the person I am proud to be.

